

Colletta, Giuseppe (2026) *Superconducting coherent structures for next-generation quantum technology.* PhD thesis.

https://theses.gla.ac.uk/86401/

Copyright and moral rights for this work are retained by the author

A copy can be downloaded for personal non-commercial research or study, without prior permission or charge

This work cannot be reproduced or quoted extensively from without first obtaining permission from the author

The content must not be changed in any way or sold commercially in any format or medium without the formal permission of the author

When referring to this work, full bibliographic details including the author, title, awarding institution and date of the thesis must be given

Enlighten: Theses
https://theses.gla.ac.uk
research-enlighten@glasgow.ac.uk



James Watt School of Engineering
College of Science and Engineering
University of Glasgow

SUPERCONDUCTING COHERENT STRUCTURES FOR NEXT-GENERATION QUANTUM TECHNOLOGY

1° Supervisor:
Prof. Martin Weides

2° Supervisor:
Prof. Vihar Georgiev

Student:
Giuseppe Colletta

Submitted in fulfillment of the requirements

for the Degree of Doctor of Philosophy

April 2026

Abstract

Superconducting quantum technologies, including SQUIDs, Single Flux Quantum (SFQ) circuits, and superconducting qubits, rely on the Josephson junction as a key building block. While superconductor-insulator-superconductor (SIS) tunnel junctions are widely used, their fabrication requires precise control of ultra-thin oxide barriers and introduces loss mechanisms associated with two-level systems, which can limit device performance. Nanobridge Josephson junctions offer an alternative approach, where the weak link is a metallic constriction, removing the oxide layer and potentially reducing dissipation and parasitic effects. This work focuses on improving the understanding and implementation of nanobridge Josephson junctions for superconducting circuits. A three-dimensional numerical model based on finite element methods is developed to describe nanobridge junctions with realistic geometries and multilayer structures, enabling the extraction of relevant parameters for circuit design. In parallel, nanobridge junctions are fabricated and experimentally characterized, including their integration into SQUID devices. In addition, superconducting microwave resonators and coplanar waveguides are designed and measured. Deviations in resonance frequency observed in multilayer resonators are interpreted in terms of kinetic inductance contributions, emphasizing the role of material properties in device performance. Flux-tunable resonators based on embedded SQUIDs are also investigated, allowing controlled tuning of the resonance frequency. Overall, this work combines modeling, fabrication, and characterization to support the development of superconducting quantum circuits based on nanobridge Josephson junctions.

Declaration

I declare that, except where explicit reference is made to the contribution of others, that this dissertation is the result of my own work and has not been submitted for any other degree at the University of Glasgow or any other institution.

Contents

List of Figures VI

Publications XVI

Introduction and Objectives XVIII

1 Background 1

1.1 Superconductivity . . . 1

1.1.1 Microscopic origin . . . 1

1.1.2 Zero Resistance and Perfect Conductivity . . . 2

1.1.3 The Meissner Effect . . . 3

1.1.4 Type-I and Type-II Superconductors . . . 4

1.1.5 The Proximity Effect . . . 6

1.2 Josephson Junctions . . . 8

1.2.1 The Josephson Effect . . . 8

1.2.2 The RCSJ Model . . . 12

1.3 Electronics based on Josephson Junctions . . . 14

1.3.1 SQUID . . . 14

1.3.2 Transmon qubit . . . 15

1.3.3 Fluxonium qubit . . . 19

1.3.4 Single Flux Quantum (SFQ) electronics . . . 20

1.4 Motivation for Nanobridge Josephson Junctions . . . 21

2 Theory and Simulations of the Nanobridge junction 23

2.1 The Green Function . . . 24

2.2 Quasi-Classical Approximation . . . 26

2.2.1 The Usadel Equations . . . 27

2.2.2 Boundary conditions between 2 different materials . . . 28

2.3 Nanobridge junction . . . 29

2.4 Modelling realistic multilayer devices for superconducting quantum electronic circuits 32

2.4.1 The Finite Element Method . . . 32
2.4.2 FEM applied to the Usadel equations . . . 33
2.5 Testing the Code . . . 35
2.5.1 1D Bridge Simulation . . . 35
2.5.2 2D Aluminium Junction Replication . . . 36
2.5.3 3D Variable Thickness Nanobridge Analysis . . . 37
2.5.4 Numerical Convergence . . . 39
2.6 Multi-layer devices . . . 39
2.6.1 Design . . . 39
2.6.2 Qubit energy levels . . . 43
2.6.3 Density of states DOS . . . 44
2.7 Further simulations . . . 45
2.7.1 SNS junction . . . 45
2.7.2 SS'S junction with $T_{CS'} > T_{CS}$ . . . 46
2.8 Conclusions . . . 49

3 Nanofabrication and DC nanobridge devices **51**
3.0.1 Properties of silicon wafers and substrate preparation . . . 51
3.0.2 Substrate cleaning and surface preparation . . . 52
3.0.3 Thin film deposition techniques . . . 52
3.0.4 Resist materials and spin coating . . . 53
3.0.5 Lithographic pattern definition . . . 54
3.0.6 Dry etching techniques . . . 56
3.0.7 Structural characterization and inspection . . . 57
3.1 Gap Engineered Superconducting Multilayer Nanobridges . . . 60
3.1.1 Fabrication of the Nanobridges . . . 60
3.1.2 Etching of Nanobridges and Micrometer Features . . . 61
3.1.3 Film Characterization . . . 63
3.1.4 Reproducibility of the Nanobridge Fabrication Process . . . 64
3.2 Cryogenic Characterization of Nanobridge Junctions . . . 65
3.3 SQUIDs . . . 67

3.4 Conclusions . . . 71

4 Microwave Circuits **73**

4.1 Transmission line basics . . . 73

4.2 Resonators . . . 75

4.2.1 Series resonator . . . 75

4.2.2 Parallel resonator . . . 77

4.3 Transmission line resonators . . . 77

4.3.1 Short-circuited $\lambda/4$ line . . . 78

4.3.2 Open-circuited $\lambda/2$ line . . . 79

4.4 Loaded quality factor and coupling . . . 79

4.4.1 Scattering matrix . . . 81

4.5 Ungrounded coplanar waveguides . . . 82

4.5.1 Transmission spectrum of microwave resonators . . . 82

4.5.2 Kinetic Inductance . . . 84

4.5.3 Kinetic inductance in multi-layer devices . . . 85

4.6 Design of Superconducting Transmission Lines and Resonators . . . 88

4.6.1 Fabrication of the microwave devices . . . 91

4.6.2 Package for resonator samples . . . 92

4.7 Resonators: Device Characterization . . . 95

4.7.1 Cryogenic microwave setup . . . 95

4.7.2 Transmission measurements . . . 98

4.7.3 Extraction of resonator parameters . . . 99

4.7.4 Power-dependent measurements . . . 100

4.7.5 Measured Kinetic inductance . . . 101

4.8 Flux-tunable resonators . . . 102

4.9 Conclusions . . . 103

Conclusions **105**

Acknowledgements **111**

Appendices **130**

List of Figures

1.1 Qualitative illustration of Cooper pair formation: an electron propagating through the lattice induces a local lattice distortion (phonon excitation), which mediates an effective attractive interaction with a second electron. Image adapted from [26]. . . 2

1.2 The two phenomena of superconductivity: a) phase transition where they exhibit zero electrical resistance, under a critical temperature b) The Meissner effect, where all the magnetic flux is expelled from the material. Image adapted from [24]. 4

1.3 Schematic overview of superconducting phenomenology. a) In the normal state, electrons occupy a continuous spectrum of energy, with the valence and conduction band overlapping at the Fermi energy E_F. Below the critical temperature T_c, an effective phonon mediated attraction leads to the formation of Cooper pairs and the opening of a superconducting energy gap 2Δ. b) The phase diagram of a type II superconductor illustrates the Meissner state for applied magnetic fields below H_{c1}, the mixed state in which magnetic flux penetrates the material as Abrikosov vortices between H_{c1} and H_{c2}, and the normal state above H_{c2}. Adapted from [27]. . 5

1.4 Conceptual representation of the Josephson effect and its microscopic origin. A Josephson junction consists of two superconducting regions weakly coupled through a) thin insulating or b) normal barrier, allowing a dissipationless current to flow when a phase difference is imposed between the superconducting order parameters. b) Charge transfer across a superconductor normal interface occurs via Andreev reflection, in which an incident electron is converted into a reflected hole while a Cooper pair is added to the superconducting condensate. Adapted from [27]. 8

1.5 (a) Current voltage characteristic of a Josephson junction under AC drive, showing the emergence of Shapiro steps. (b) Tilted washboard potential as described by Eq. 1.2.21 for different bias currents. 13

1.6 (a) Superconducting Quantum Interference Device (SQUID). I represents the current supplied to the device, while the numbers 1 and 2 represent the two Josephson junctions, and H is the applied magnetic field. b) Example of SQUID critical current modulation, computed for $L = 0$ ($\beta_L = 0$). Adapted from [4]. 16

1.7 Transmon qubit, real device (up) and lumped model (down). A transmon qubit is created by shunting a SQUID with a capacitance. In this way the parameters of the Hamiltonian in Eq. (1.3.3) can be tailored to design a qubit which is controllable and resistant to noise. Adapted from [10]. 16
1.8 The energy levels of a Transmon qubit at different ratios of Josephson and charge energy are shown. Higher charging energy results in higher anharmonicity, but also high sensitivity to charge noise n_g (proportional to the slope of the curve). Therefore, it is important to find the right ratio of E_J and E_C to reduce noise and maintain high anharmonicity. Adapted from [10]. 18
1.9 Fluxonium, real device (up), and lumped model (down). Adapted from [56]. 18
1.10 Fluxonium energy levels for $E_J = 4$ GHz, $E_C = 0.5$ GHz, $E_L = 0.1$ GHz. 20
1.11 SFQ circuit model, a DC pulse at the input generates an SFQ pulse at the output. Adapted from [25]. 20

2.1 Two different types of nanobridge junctions: planar (a) and variable-thickness (b). The nanobridge is a type of Josephson junction where the connection between the two electrodes is a small constriction made of the same material or a different one. Typical dimensions of the constriction are a few tens of nanometer in length. 29
2.2 Current phase relationship (CPR) of a nanobridge junction in the limit of small length L, referred to as the KO-1 model [62]. 29
2.3 CPR of planar (a) and variable-thickness (b) nanobridge junctions for different bridge lengths; the width of the bridge is $W = 45$ nm in all cases. The junctions are considered to be made of aluminium. The phase difference of the function Φ in Eq. (2.2.10) across the nanobridge junction is shown for the planar (c) and variable-thickness (d) designs. It can be observed that in the variable-thickness design, the phase drops significantly only in a region closer to the constriction compared to the planar case. As discussed in the main text, this means that the electrodes behave as good reservoirs of superconductivity, resulting in a less skewed CPR, which will be useful in applications in quantum circuit dynamics, as discussed in the next section. Figures from [18]. 31

2.4 3D models of the nanobridge junction considered in this work: (a) effective 1D bridge, (b) planar junction, and (c) variable thickness junction. Rigid boundary conditions are applied as described in the text. 36
2.5 CPR (dots) obtained from simulations of a nanobridge with length $L \ll \xi$ at different temperatures, compared to the KO-1 model (solid lines). 36
2.6 CPR calculated from the models in Fig. 2.4, replicating the junction designs of Ref. [18] in order to validate the numerical code. (a) Planar junctions. (b) Variable thickness junctions. (c) Phase variation across the planar junction. (d) Phase variation across the VTB junction. 38
2.7 Convergence of the critical current as a function of the number of mesh elements, with the number of phase steps kept fixed. Figure from [2]. 39
2.8 Three-dimensional designs of the nanobridge junctions analyzed in this work. (a) Planar nanobridge junction. (b) Variable-thickness nanobridge (VTB) junction. (c) Cross-section of a simplified VTB junction with rectangular edges. (d) Cross-section of a VTB junction with realistically rounded edges. Different colors indicate the presence of different materials. Figure from [2]. 40
2.9 (a) Simulated current phase relations (CPRs) of different nanobridge junctions. For the VTB junctions, the parameters are $L/\xi_{S'} = 2$, $L' = 2L$, $T/T_{CS'} = 0.1$, $T_{CS}/T_{CS'} = 5$, $\xi_S = 5\xi_{S'}$, $\gamma_B = 0.01$, $\gamma = 0.01$, and $T_{CS} = 5\,\mathrm{K}$. For the planar junction, a single material is considered, with parameters $L/\xi_S = 2$, $T/T_{CS} = 0.1$, and $T_{CS} = 5\,\mathrm{K}$. Here, A denotes the cross-sectional area of the nanobridge. The inset shows the normalized pair potential of the planar junction with rounded edges, simulated using the same parameters and a phase difference $\delta = 0.3\pi$, illustrating the expected suppression of the order parameter in the weak-link region. (b) Comparison between simulated and experimental critical currents from Ref. [79] as a function of nanobridge length. The percentage difference between the experimental values and those obtained from the simulations or from the KO-1 model is reported. Overall, the simulated results show good agreement with the experimental data, with improved alignment obtained by assuming a larger coherence length than the value originally reported in Ref. [79], consistent with Ref. [80]. Figure from [2]. . . . 41

2.10 Simulated anharmonicities of (a) Transmon and (b) Fluxonium qubits using the CPR from Fig. 2.9, assuming the same Josephson energy for all devices. Both qubits use $E_C = 300$ MHz, and the Fluxonium also uses $E_L = 0.53\,E_C$ [57]. For the Fluxonium, smaller E_J values were explored, as it operates in the regime $E_J < 10\,E_C$ [59]. Figure from [2]. 43

2.11 (a) Simulated current phase relations (CPR) of the variable-thickness nanobridge (VTB) junction with rounded cross-section shown in Fig. 2.8, for different values of the normal metal coherence length ξ_N. The simulations were performed using $T/T_C = 0.1$, $\xi_S = 200$ nm, $L = 60$ nm, $L' = 2L$, $\gamma_B = 0.01$, and $\gamma = 0.01$. (b) Dependence of the critical current I_C on the parameter γ for different values of ξ_N. The remaining parameters were fixed to $T/T_C = 0.1$, $\xi_S = 200$ nm, $L = 60$ nm, and $\gamma_B = 0.01$. Adapted from [2]. 46

2.12 Density of states DOS(E) calculated inside the SNS nanobridge for different values of the superconducting phase difference $\Delta\delta$. The parameters used were $T/T_C = 0.1$, $\xi_S = 200$ nm, $\xi_N = 120$ nm, $W = 20$ nm, $L = 60$ nm, $L' = 2L$, $\gamma_B = 0.01$, and $\gamma = 0.01$. The results illustrate the emergence of quasiparticle states within the normal metal weak link. Figure from [2]. 47

2.13 (a) Simulated current phase relations (CPR) of the SS'S variable-thickness nanobridge (VTB) junction with rounded cross-section shown in Fig. 2.8 for different values of $\xi_{S'}$. The parameters used were $T/T_{CS} = 0.1$, $T_{CS} = 1$, $T_{CS'} = 5$, $\xi_S = 200$ nm, $W = 20$ nm, $L = 60$ nm, $L' = 2L$, $\gamma_B = 0.01$, and $\gamma = 0.01$. (b) Dependence of the critical current I_C on the parameter γ for different values of $\xi_{S'}$. The remaining parameters were fixed to $T/T_C = 0.1$, $\xi_S = 200$ nm, $L = 60$ nm. (c) CPR for different distances between the banks, $\xi_{S'} = 30$ nm, $L = 60$ nm. 48

2.14 Density of states DOS(E) calculated for an SS'S nanobridge junction with $L/\xi_{S'} = 2$. The parameters used were $T/T_{CS} = 0.1$, $T_{CS} = 1$, $T_{CS'} = 5$, $\xi_S = 200$ nm, $\xi_{S'} = 30$ nm, $W = 20$ nm, $L = 60$ nm, $\gamma_B = 0.01$, and $\gamma = 0.01$. In addition to the standard quasiparticle peaks, extra features appear at higher energies due to the larger superconducting gap of the bottom layer. Figure from [2]. 49

3.1 a) Simple schematic overview of the sputtering process, b) Picture of the main chamber of the sputtering tool used in this work, where all the different targets are shown. Adapted from [26]. 53
3.2 Schematic example of positive and negative tone resist. Adapted from [25]. 54
3.3 (a) Schematic overview of an electron beam lithography system, adapted from [94]. Electrons emitted from the source are focused by lenses into a finely controlled beam, which is scanned across the substrate to locally expose the resist according to the desired pattern. (b) Example of a lithographic pattern written on the substrate. . . 55
3.4 Schematic overview of an inductively coupled plasma (ICP) dry etching system. An RF-driven coil surrounding the chamber inductively couples energy into the system, while an independently powered RF bias is applied to the substrate electrode, enabling separate control of plasma density and ion energy. 57
3.5 Examples of SEM images taken for two samples: (a) a SQUID, where SEM was used to check that no residues or other contaminants were present near the structure, and to verify the alignment of features after multiple exposures; (b) a planar nanobridge, showing the typical size of the fabricated devices. 59
3.6 Schematic illustration of the two step fabrication process used to realize multilayer 3D nanobridges. Large features and the planar bridge are first defined, followed by a second etching step that selectively removes only the top Nb layer above the bridge. This leaves the bottom nitride layer intact, forming a high resistance three-dimensional weak link. Figure from [1]. 60
3.7 Critical temperature T_C and resistivity characterization of the materials used for nanobridge fabrication: (a) Nb, (b) NbN, and (c) TiN. The absence of data points around 3 K for TiN is due to measurements performed in a different cryostat, which did not allow fine temperature control in this range. Figure from [1]. 63
3.8 Room temperature resistance of multilayer nanobridges measured using a probe station. The resistance is shown as a function of the junction index for a set of nominally identical devices. The distribution is centered at $R = 198\,\Omega$, with a spread of $\sim 20\%$, reflecting moderate variability likely arising from nanoscale fabrication inhomogeneities. Overall, the results confirm the reproducibility of the process. Figure from [1]. 65

3.9 (a) Representative current voltage characteristics of NbN nanobridge Josephson junctions. All curves were measured at the base temperature of the dilution refrigerator, 40 mK. (b) Critical current as a function of normal state resistance. Two device populations are observed: low resistance junctions (gray region), attributed to incomplete etching and residual Nb, exhibit an I_cR_N independent of the nitride layer; properly defined junctions follow the expected trend. Solid lines correspond to simulations based on the KO-1 model and the three-dimensional Usadel model ($L = 30$ nm, $\xi = 10$ nm), with the effective cross section adjusted to match R_N. The agreement is quantified by $\chi^2_{\text{norm}} = 0.96$ (Usadel) and 3.5 (KO-1). (c) Simulated spatial profiles of the superconducting gap for NbN and TiN multilayer nanobridges at $T = 0.1T_c$ ($L = 30$ nm, $W = 60$ nm). Proximity effects lead to a $\sim 5\%$ suppression in NbN and a $\sim 60\%$ enhancement in TiN. Figure from [1]. 66

3.10 Flux modulation of the critical current in SQUIDs based on (a,c) NbN (Sample A) and (b,d) TiN (Sample B). The NbN device shows a modulation depth of about 5%, while the TiN device reaches approximately 20%. The relatively limited modulation depth is mainly attributed to the asymmetry between the two nanobridges, while the loop inductance ($\beta_L \approx 0.25$) plays only a minor role. Panels (c) and (d) display the full modulation under positive and negative current bias, highlighting asymmetries arising from differences in critical current and CPR between the two nanobridges. Figure adapted from [1]. 68

3.11 Measured SQUID critical current as a function of magnetic flux together with theoretical fits. (a) NbN based SQUID, with inset showing a zoom of a small feature associated with higher harmonic contributions to the CPR. (b) TiN based SQUID. Solid lines represent fits obtained using an asymmetric dc SQUID model including finite loop inductance, comparing both sinusoidal and nanobridge specific CPRs [2]. Figure adapted from [1]. 69

4.1 Lumped-element representation of a transmission line. Adapted from [129]. 74

4.2 Transmission line terminated by a load impedance. Adapted from [129]. 75

4.3 (a) Lumped-element model of a series resonator and (b) corresponding input impedance. Adapted from [129]. 77

4.4 (a) Lumped-element model of a parallel resonator and (b) corresponding input impedance. Adapted from [129]. 78
4.5 Schematic overview of a) Short-circuited $\lambda/4$ line b) Open-circuited $\lambda/2$ line 78
4.6 Capacitive coupling between a feedline and a resonator. Adapted from [129]. 80
4.7 Geometry of a coplanar waveguide: central conductor of width W, separated by G from the ground plane. Adapted from [131]. 83
4.8 (a) 3D schematic of a multilayer CPW (not to scale). Panels (b) to (d) show the magnitude of the function Φ in the CPW for different values of γ: (b) $\gamma = 10$, (c) $\gamma = 1$, and (d) $\gamma = 0.1$. The dotted line marks the interface between the niobium layer and the encapsulating material. The simulations used $\xi_S = 5\,\xi_N$, $\xi_N = 30$ nm, $\gamma_b = 0.01$, $T/T_{CS} = 0.1$, and layer thicknesses of 200 nm for the superconductor and 20 nm for the normal metal. These results illustrate that the proximity effect strongly depends on γ: larger values of γ significantly suppress the magnitude of Φ, even when the encapsulating layer is thinner than the coherence length. Figure from [2]. 87
4.9 Simulated magnitude of the function Φ in a CPW (not to scale for clarity), capped with the materials listed in Tab. 4.1: (a) Au, (b) Al, (c) TiN, and (d) Ta. The dotted line marks the interface between the niobium and the encapsulating layer. As expected, materials with low γ have only a minor effect on Φ, while larger γ values lead to a more pronounced suppression. Figure from [2]. 88
4.10 Coplanar waveguide simulated in HFSS to extract the characteristic impedance and match it to 50 Ω. As described in [143], a wave port (pink rectangle) with dimensions larger than $3(2S + W)$ in width and $2t$ in height was used. 89
4.11 Coupling strength and quality factor extraction performed by setting the lengths and separation of two CPWs, using the open-source code from [144]. 89
4.12 Design of five CPW resonators coupled to the same feedline in a hanging-resonator configuration. 90
4.13 Eigenmode simulation of one of the quarter-wave resonators showing the electric field distribution on the chip surface. 90
4.14 Convergence behavior of the eigenmode solver. Simulations were stopped when the relative frequency variation was below 5%. 91

4.15 Simulated S_{21} of the five-resonator sample: (a) $f_0 = 4.24$ GHz, $Q_C \sim 1 \cdot 10^5$; (b) $f_0 = 4.58$ GHz, $Q_C \sim 1.15 \cdot 10^5$; (c) $f_0 = 5.34$ GHz, $Q_C \sim 1.37 \cdot 10^5$; (d) $f_0 = 6.639$ GHz, $Q_C \sim 0.55 \cdot 10^5$; (e) $f_0 = 7.27$ GHz, $Q_C \sim 0.6 \cdot 10^5$. 92
4.16 (a) Package used for fixed-frequency resonators (diameter of internal cavity: 1.5 cm). (b) Package used for flux-tunable resonators ($3 \times 3 \times 2$ cm^3). 93
4.17 RF connectors considered for the package design. 94
4.18 (a) Designed package, y-view. (b) Designed package, z-view. (c) Picture of the fabricated package ($4 \times 4 \times 2$ cm^3). 95
4.19 Simulated eigenmodes of the custom package: (a) first resonance $\sim$ 11 GHz, (b) second resonance $\sim$ 12 GHz, (c) fifth resonance $\sim$ 13 GHz. 95
4.20 Measured scattering parameters of the PCB and package assembly: (a) S_{11}, (b) S_{22}, and (c) S_{21}. 96
4.21 a) Photograph of the cryostat used for microwave measurements adapted from [24, 26]. b) Electrical wiring diagram of the cryogenic measurement setup, showing signal flow through attenuators, circulators, amplifiers, and temperature stages (300 K to 40 mK). c) Legend of symbols used in the schematic. d) Close-up view of the superconducting sample mounted in the copper sample box at the mixing chamber stage (40 mK). 97
4.22 Circle fit performed for the TiN based resonator at an input power of -5 dB: (a) circle fit in the complex plane, (b) amplitude, (c) phase. 98
4.23 Comparison of internal quality factors (Q_i) for TiN and NbN based multilayer resonators. Both devices exhibit similarly high Q_i values, indicating that losses associated with different bottom nitride layers play a minor role; instead, dissipation is predominantly governed by the superconducting film, substrate, and interfaces, consistent with the use of high quality niobium resonators. 99
4.24 Kinetic inductance extracted from resonance shifts with respect to a perfect-electric-conductor (PEC) reference resonator for (a) Sample A and (b) Sample B. 102

4.25 Measured and fitted resonance frequency of flux-tunable superconducting resonators fabricated with TiN and NbN, demonstrating continuous frequency tuning via magnetic flux biasing. The large extracted screening parameter, $\beta_L > 1.5$, indicates strong inductive screening due to the relatively high critical current of the nanobridge SQUIDs ($I_c \sim 100$ μA). 104
4.26 SEM images of (a) the x-oriented nanobridges forming the SQUID in the flux-tunable resonator (dimensions: 152×32 nm^2) and (b) y-oriented nanobridges (dimensions: 65×43 nm^2). The electron-beam lithography distortion along the x-axis leads to a larger effective junction area and increased critical current. The images were taken on twin devices fabricated together with the measured ones, which were not imaged by SEM before the measurements. 104

Publications

Journal Articles

1. **Colletta, G.**, Johny, S., Feng, H., Alkhalidi, M., Collins, J. A., Weides, M., "Gap Engineered Superconducting Multilayer Nanobridge Josephson Junctions," (2026), `arXiv:2603.20757` [1]. (under review in *Applied Physics Letters* as of 01/04/2026).

2. **Colletta, G.**, Johny, S., Collins, J. A., Casaburi, A., Weides, M., "Modeling realistic multilayer devices for superconducting quantum electronic circuits," *Applied Physics Letters* **126**(14), 142601 (2025). DOI: `10.1063/5.0251879` [2].

Conference Contributions

1. Weides, M., **Colletta, G.**, Johny, S., Collins, J. A., Reynolds, P. Casaburi, A., Seferai, V., Zhao, S. "Multilayer superconducting circuits: model and experiments," APS Global Physics Summit 2026, Denver (2026), Oral presentation.

2. **Colletta, G.**, Weides, M., "Design and Analysis of Multilayer Superconducting Devices for Quantum Technologies," SM2Q, Glasgow (2025), Oral presentation.

3. Imroze, F., Yalagala, B., Ahmad, M., Elsayed, M., Graham, R., **Colletta, G.**, "Hysteresis-Induced Neuromorphic Behavior in 180nm Bulk PMOS Devices at 3K," *2025 IEEE 37th International Conference on Microelectronic Test Structures (ICMTS)*, San Antonio, TX, USA, 2025, pp. 1-4, doi: `10.1109/ICMTS63811.2025.11068927` [3]. Conference Proceeding.

4. **Colletta, G.**, Weides, M., "Design and Analysis of Multilayer Devices for Superconducting Quantum Technologies," QCI3 Hub, Oxford (2025), Poster.

5. **Colletta, G.**, Weides, M., "Modelling Realistic Multilayer devices for quantum electronic circuits," QCA, Glasgow (2024), Oral presentation.

6. **Colletta, G.**, Johny, S., Collins, J. A., Weides, M., "Fabrication of Multi-layer devices for quantum electronic circuits", JWNC Internal Conference, Glasgow (2024), Oral presentation.

7. **Colletta, G.**, Weides, M., Casaburi, A., "Superconducting Coherent Structures for Next-Generation Quantum Technology," EUCAS, Bologna (2023), Poster.

Introduction and Objectives

Most superconducting quantum technologies, such as SQUIDs (Superconducting QUantum Interference Devices) [4], Single Flux Quantum (SFQ) circuits [5], and superconducting qubits [6], rely on a common key element: the Josephson junction. A Josephson junction is an electronic device consisting of two superconducting electrodes connected by a weak link [7, 8]. This configuration gives rise to the Josephson effect, where a supercurrent flows between the two electrodes even in the absence of an applied voltage. The supercurrent originates from a phase difference between the macroscopic quantum wave functions of the Cooper-pair condensates in the two superconductors [9]. In recent years, this property has been exploited in a wide range of applications, and the dependence of the supercurrent on the superconducting phase difference is one of the key reasons why quantum computers based on superconducting devices operate successfully [10]. One of the most commonly used Josephson junctions in qubits and SFQ circuits is the superconductor-insulator-superconductor (SIS) tunnel junction, where the electrodes are coupled through an ultra-thin insulating barrier. Although excellent results have been achieved using this approach [11, 12], tunnel junctions present several limitations. Their fabrication requires multiple processing steps and tight control of oxide thickness, making the process more prone to variability and defects. Moreover, in superconducting qubits, decoherence is strongly influenced by two-level systems (TLSs) hosted also in the amorphous oxide barrier, which couple to the circuit and reduce coherence times [13–16].

An alternative approach is provided by nanobridge Josephson junctions, where the coupling between the superconducting electrodes is achieved through a narrow metallic constriction rather than an insulating barrier. This geometry removes the oxide layer entirely, significantly reducing TLS-related losses and parasitic capacitance, while also enabling more compact device layouts. Despite these advantages, most experimental work on nanobridge junctions has so far relied on simplified design rules based on strong assumptions and one-dimensional models [7, 17, 18]. Theoretical studies have mainly focused on two-dimensional geometries [18], while the few three-dimensional simulations reported in the literature did not specifically target applications in superconducting quantum technologies or realistic device layouts [17, 19].

The first objective of this Ph.D. is to improve the theoretical understanding of nanobridge

Josephson junctions in order to establish a solid engineering framework for their design and integration into larger superconducting circuits, such as SQUIDs, qubits, and SFQ architectures. An extensive numerical model was developed using modern finite element techniques to solve the equations describing three-dimensional nanobridge junctions with arbitrary geometries and multilayer material stacks. This represents one of the first attempts to create an open and flexible engineering platform for the design of nanobridge Josephson junctions and the extraction of the parameters required for their implementation in complex superconducting circuits [2]. In parallel, the experimental activity focused on the fabrication and testing of nanobridge junctions and their use in SQUIDs.

In addition to Josephson junctions, most superconducting quantum circuits rely on coplanar waveguides (CPWs) and microwave resonators for their operation [20, 21]. These elements play a central role in circuit quantum electrodynamics, acting as readout resonators, coupling buses, and filters. To meet the stringent requirements of quantum applications, the accurate simulation and design of CPW resonators are essential parts of the fabrication process. In this work, we design and fabricate superconducting microwave resonators using conformal mapping techniques and electromagnetic simulations, allowing precise control of resonance frequency, impedance matching, and coupling strength. We further investigate systematic shifts in the resonance frequencies of multilayer resonators, which are interpreted in terms of variations in kinetic inductance. By comparing experimental data with full-wave simulations of ideal perfect electric conductor (PEC) resonators, we extract the additional kinetic inductance contribution associated with the multilayer films, which highlights the importance of combining electromagnetic simulations with detailed material characterization when interpreting resonator measurements.

A further part of this thesis is devoted to flux tunable superconducting resonators, where tunability is achieved by embedding a SQUID into the resonator. In these devices, the effective inductance becomes dependent on the applied magnetic flux, allowing controlled tuning of the resonance frequency. Finally, this work also addresses practical aspects of microwave measurements, including the design of three-dimensional sample boxes and printed circuit boards.

The thesis is organized as follows. Chapter 1 reviews the basic concepts of superconductivity, the proximity effect and Josephson junctions. Chapter 2 presents the theoretical framework and numerical simulations developed for nanobridge Josephson junctions. Chapter 3 describes the nanofabrication processes and the experimental characterization of nanobridge junctions and

SQUIDs. Chapter 4 discusses the theory and design of microwave resonators, coplanar waveguides, microwave packaging and their experimental characterization. The final chapter summarizes the main results and outlines future research directions, together with the steps needed to achieve them.

1. Background

This chapter introduces the physical concepts and devices on which the rest of the thesis is based. Section 1.1 summarises the main properties of superconductors, from the microscopic origin of superconductivity to the Meissner effect and the distinction between type-I and type-II materials, and introduces the proximity effect, which is central to the multilayer devices studied in this work. Section 1.2 describes the Josephson effect, the AC and DC Josephson relations, Shapiro steps and the RCSJ model, which are used throughout the thesis to interpret the measurements on nanobridge junctions. Section 1.3 reviews the main superconducting circuits based on Josephson junctions that motivate this work: SQUIDs, transmon and fluxonium qubits, and SFQ electronics. For each of them we highlight the junction properties that matter most, such as the critical current and the shape of the current phase relation. Finally, Section 1.4 discusses the limitations of tunnel junctions and motivates the study of nanobridge Josephson junctions, which is the subject of the following chapters.

1.1 Superconductivity

Superconductivity is a macroscopic quantum phenomenon observed in a wide class of materials at sufficiently low temperatures. Since its discovery, it has played a central role in both fundamental physics and technological applications. In this section, we introduce the basic concepts required to understand the superconducting devices studied in this thesis, focusing on the physical properties most relevant for Josephson junctions [9, 22–27].

1.1.1 Microscopic origin

The microscopic understanding of superconductivity is provided by the Bardeen, Cooper and Schrieffer (BCS) theory [28]. Within this framework, superconductivity arises from the formation of electron pairs, known as Cooper pairs, which despite the repulsive Coulomb interaction, feel an effective attractive interaction mediated by lattice vibrations, or phonons as seen in Fig. 1.1. Cooper pairs consist of electrons with opposite momenta and spin, forming a boson. The condensation of a macroscopic number of Cooper pairs leads to phase coherence across the entire superconducting

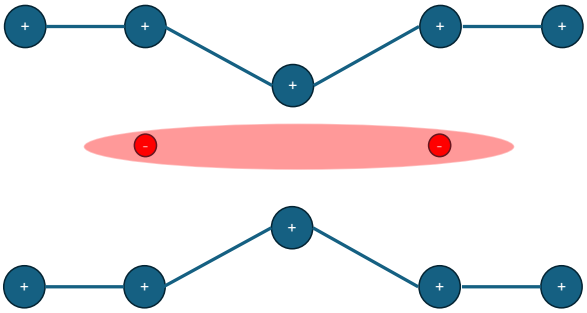

Figure 1.1: Qualitative illustration of Cooper pair formation: an electron propagating through the lattice induces a local lattice distortion (phonon excitation), which mediates an effective attractive interaction with a second electron. Image adapted from [26].

sample. As a consequence, the superconducting state can be described by a complex parameter

$$\Psi(\mathbf{r}) = |\Psi(\mathbf{r})|e^{i\phi(\mathbf{r})} \tag{1.1.1}$$

whose magnitude is related to the density of Cooper pairs. A direct consequence of Cooper pair condensation is the opening of an energy gap Δ in the energy spectrum at the Fermi level, Fig. 1.3(a). This superconducting gap represents the energy required to break a Cooper pair and create quasiparticle excitations. In conventional superconductors described by BCS theory, the zero temperature gap $\Delta(0)$ is directly related to the critical temperature T_c through the relation

$$2\Delta(0) = 3.52\, k_B T_c \tag{1.1.2}$$

The fact that excitations with energy smaller than 2Δ are unable to break Cooper pairs explains the absence of electrical resistance in the superconducting state.

1.1.2 Zero Resistance and Perfect Conductivity

Below the critical temperature T_c, superconductors have zero electrical resistance, Fig. 1.2. Experimentally, the transition into the superconducting state is marked by a sharp drop of the electrical resistance to zero and by a change in magnetic response. The electrical conductivity of superconductors can be understood through an extension of the Drude model [9, 24]. In normal metals, the current density $\mathbf{J}$ is related to the electric field $\mathbf{E}$ through Ohm's law:

$$\mathbf{J} = \sigma_0 \mathbf{E} = \frac{nq^2\tau}{m}\mathbf{E} \tag{1.1.3}$$

where n is the charge carrier density, q and m are the charge and mass of the carriers, τ is the electrical mean free time, and σ_0 is the DC conductivity. For frequency dependent signals, this generalizes to:

$$\sigma(\omega) = \sigma_0 \frac{1}{1 + j\omega\tau} \tag{1.1.4}$$

In the limit of infinite mean free time ($\tau \to \infty$), corresponding to a perfect conductor with no scattering, the conductivity becomes purely imaginary:

$$\sigma(\omega) = \frac{nq^2}{m} \frac{1}{j\omega} \tag{1.1.5}$$

This expression reveals a key characteristic of superconductors: the impedance is dominated by an inductive term proportional to $j\omega$, corresponding to the kinetic inductance [24, 29]. This inductance arises from the inertia of the charge carriers, with energy stored in the kinetic energy of electrons [24]. The two fluid model [30] describes the total charge carrier density n as the sum of Cooper pair density n_s and quasiparticle density n_{qp}:

$$n = n_s + n_{qp} \tag{1.1.6}$$

Below T_c, Cooper pairs dominate, and as temperature decreases toward absolute zero, n_s increases exponentially while n_{qp} diminishes. The complex conductivity of a superconductor can then be written as:

$$\sigma(\omega) = \sigma_{qp}(\omega) + \sigma_s(\omega) \approx \frac{n_{qp} e^2 \tau}{m} - j \frac{4 n_s e^2}{\omega m} \tag{1.1.7}$$

The first term represents the resistive contribution from quasiparticles, which becomes negligible at temperatures well below T_c. The second term represents the superconducting contribution, which is purely reactive and corresponds to the kinetic inductance.

1.1.3 The Meissner Effect

The Meissner effect [24, 31] demonstrates that superconductors are not only perfect conductors but also perfect diamagnets. When cooled below T_c in an applied magnetic field, a superconductor expels magnetic flux from the inside, creating screening currents at its surface that cancel the applied field within the material. This behavior distinguishes superconductors from perfect conductors. A perfect conductor would maintain whatever magnetic flux was present when it became a perfect conductor (by Lenz's law), whereas a superconductor always expels it. The penetration

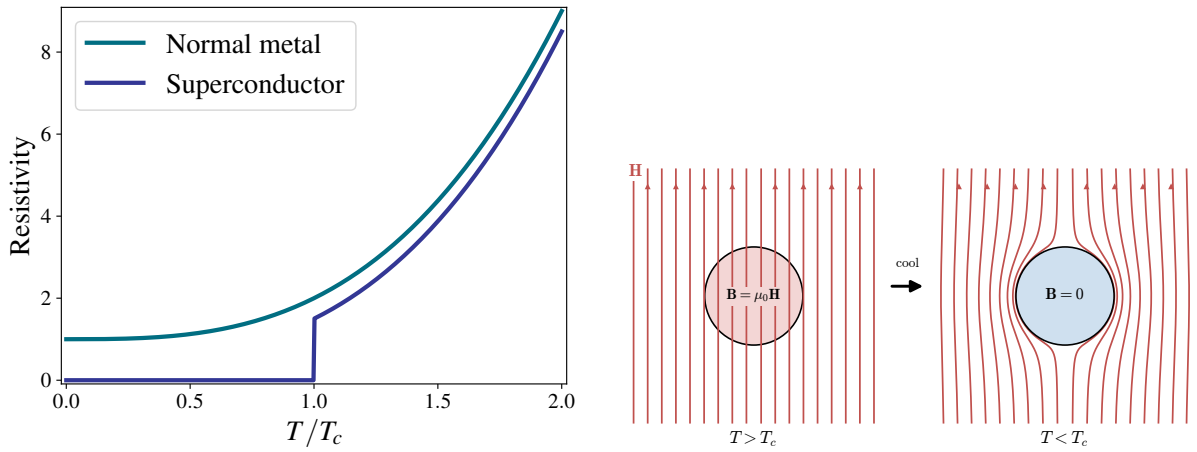

(a) (b)

Figure 1.2: The two phenomena of superconductivity: a) phase transition where they exhibit zero electrical resistance, under a critical temperature b) The Meissner effect, where all the magnetic flux is expelled from the material. Image adapted from [24].

of magnetic fields into a superconductor is characterized by the London penetration depth λ_L:

$$\lambda_L = \sqrt{\frac{m}{4\mu_0 n_s e^2}} \tag{1.1.8}$$

The magnetic field decays exponentially within this length scale: $B(x) = B(0)e^{-x/\lambda_L}$.

1.1.4 Type-I and Type-II Superconductors

Superconductors are classified into two distinct types based on their response to applied magnetic fields, as predicted by Ginzburg-Landau (GL) theory [24, 32]. This theory introduces two characteristic length scales: the London penetration depth λ_L and the coherence length ξ, which describes the spatial extent over which the superconducting order parameter can vary. The ratio of these lengths, the Ginzburg-Landau parameter:

$$\kappa = \frac{\lambda_L}{\xi} \tag{1.1.9}$$

determines the type of superconductor.

Type-I Superconductors

Type-I superconductors are characterized by $\kappa < 1/\sqrt{2}$. When an external magnetic field is applied, these materials exhibit perfect diamagnetism (complete Meissner effect) up to a critical

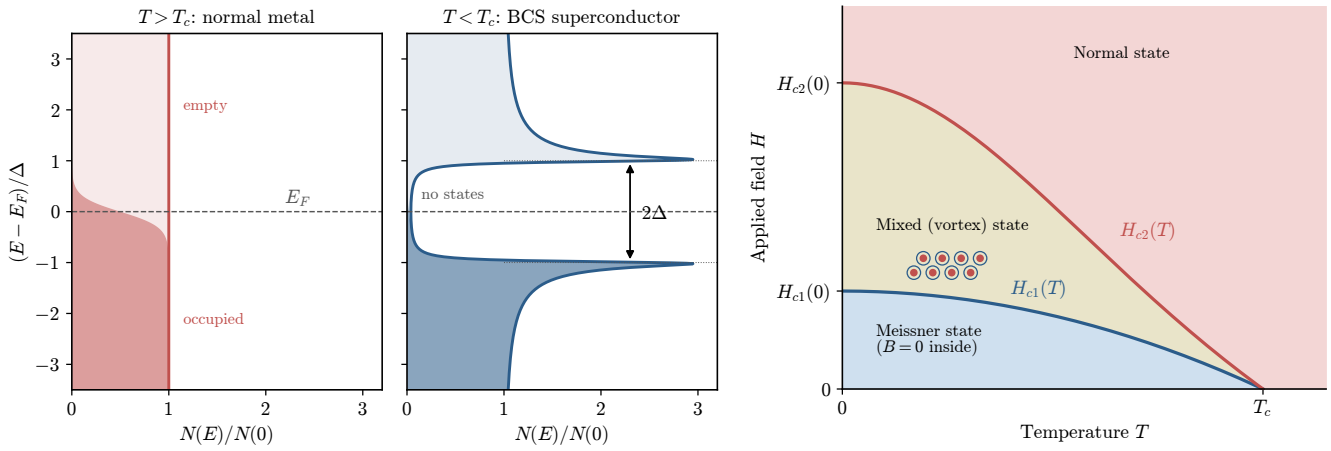

(a) (b)

Figure 1.3: Schematic overview of superconducting phenomenology. a) In the normal state, electrons occupy a continuous spectrum of energy, with the valence and conduction band overlapping at the Fermi energy E_F. Below the critical temperature T_c, an effective phonon mediated attraction leads to the formation of Cooper pairs and the opening of a superconducting energy gap 2Δ. b) The phase diagram of a type II superconductor illustrates the Meissner state for applied magnetic fields below H_{c1}, the mixed state in which magnetic flux penetrates the material as Abrikosov vortices between H_{c1} and H_{c2}, and the normal state above H_{c2}. Adapted from [27].

field H_c. Above this field, superconductivity is abruptly destroyed throughout the entire sample, and the material transitions to the normal state. The critical field depends on temperature as:

$$H_c(T) = H_c(0)\left[1 - \left(\frac{T}{T_c}\right)^2\right] \tag{1.1.10}$$

Examples of Type-I superconductors include bulk aluminium and TiN [24, 33]. The free energy difference between the superconducting and normal states at the critical field is [9]:

$$\Delta F = \frac{\mu_0 H_c^2}{2} V \tag{1.1.11}$$

In Type-I superconductors, the interface between superconducting and normal regions has positive surface energy, making it energetically unfavorable to form multiple domains. This leads to the expulsion of the magnetic field and to an intermediate state, in which macroscopic normal regions form in the superconductor above a certain applied magnetic field.

Type-II Superconductors

Type-II superconductors, characterized by $\kappa > 1/\sqrt{2}$, exhibit more complex behavior in magnetic fields. These materials have two critical fields:

- **Lower critical field H_{c1}:** Below this field, the superconductor exhibits complete Meissner effect.
- **Upper critical field H_{c2}:** Above this field, superconductivity is completely destroyed.

Between H_{c1} and H_{c2}, the superconductor enters the mixed state (or vortex state), where magnetic flux penetrates in quantized units called flux vortices or Abrikosov vortices as in Fig. 1.3(b). Each vortex carries exactly one flux quantum Φ_0 and consists of [27]:

- A normal core of radius approximately ξ where the Cooper pair density vanishes
- Circulating supercurrents extending over a radius λ_L

The critical fields are related to H_c by [9]:

$$H_{c1} \approx \frac{H_c}{\sqrt{2}\kappa} \ln \kappa, \quad H_{c2} \approx \sqrt{2}\kappa H_c \tag{1.1.12}$$

In Type-II superconductors, the interface between superconducting and normal regions has negative surface energy, making it energetically favorable to form many small normal regions (vortices) rather than large normal domains as in Type-I superconductors. This is why flux penetration occurs gradually through the formation of vortex lattices. In the thin-film regime, many superconductors behave like Type-II superconductors [24, 34, 35].

1.1.5 The Proximity Effect

When a superconductor (S) is placed in contact with a normal metal (N), or with a weaker superconductor (S') with a lower critical temperature, the superconducting properties of both materials are modified near the interface. This phenomenon is known as the proximity effect [9, 36]. Cooper pairs from the superconductor can enter the normal metal, so that superconducting correlations are induced in N over a characteristic length; at the same time, the pair amplitude in S is reduced near the interface. Microscopically, the transfer of pair correlations across the interface takes place through Andreev reflection, which is discussed in Section 1.2.

In the dirty limit, which applies to the thin films used in this thesis, the induced pair amplitude in the normal metal decays over the normal-metal coherence length

$$\xi_N = \sqrt{\frac{\hbar D_N}{2\pi k_B T}} \tag{1.1.13}$$

where D_N is the electronic diffusion coefficient of the normal metal. On the superconducting side, the order parameter recovers its bulk value over a distance of the order of the superconducting coherence length $\xi_S = \sqrt{\hbar D_S/2\pi k_B T_C}$. When both layers are much thinner than their coherence lengths, the bilayer behaves as a single, homogeneous superconductor with an intermediate critical temperature (the Cooper limit) [36, 37]. In this limit, the effective coupling constant is the average of the coupling constants of the two layers, weighted by their thickness d and density of states $N(0)$,

$$(NV)_{\text{eff}} = \frac{(NV)_S\, N_S(0)\, d_S + (NV)_N\, N_N(0)\, d_N}{N_S(0)\, d_S + N_N(0)\, d_N} \tag{1.1.14}$$

with $(NV)_N = 0$ for a normal metal, so that a thicker normal layer lowers the critical temperature of the bilayer.

The strength of the proximity effect depends strongly on the properties of the interface and on the ratio of the normal state conductances of the two materials. In the theory of dirty SN and SS' materials, these are described by two parameters [8, 38]: the suppression parameter $\gamma = \rho_S \xi_S/(\rho_N \xi_N)$, which compares the conductance of the two layers over one coherence length, and the interface parameter $\gamma_B = R_B/(\rho_N \xi_N)$, which accounts for the boundary resistance R_B. A small γ means that the second layer can only weakly draw pairs from the superconductor, which therefore keeps its bulk properties, while a large γ leads to a strong suppression of the order parameter in S. A large γ_B corresponds to a poorly transparent interface, which decouples the two layers. These parameters enter the boundary conditions of the Usadel equations used in Chapter 2.

The proximity effect is central to this thesis for three reasons. First, it is the mechanism that carries the supercurrent across SNS and SS'S junctions, as discussed in the next section. Second, the multilayer nanobridges developed in this work consist of several superconducting layers in direct contact, so the superconducting gap and the critical current of the weak link depend on the coupling between the layers (Chapters 2 and 3). Third, the proximity effect modifies the superconducting gap and the kinetic inductance of encapsulated or multilayer microwave resonators (Chapter 4).

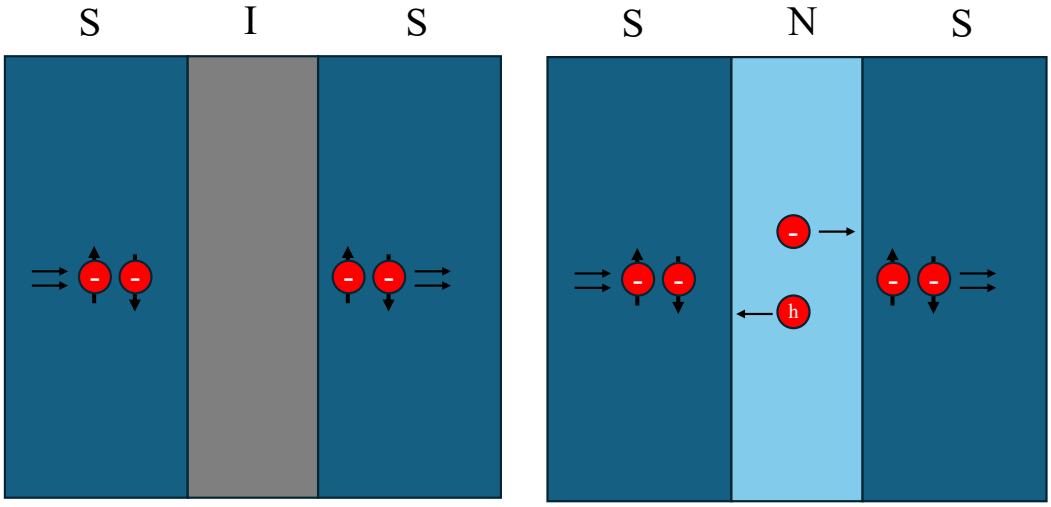

(a) (b)

Figure 1.4: Conceptual representation of the Josephson effect and its microscopic origin. A Josephson junction consists of two superconducting regions weakly coupled through a) thin insulating or b) normal barrier, allowing a dissipationless current to flow when a phase difference is imposed between the superconducting order parameters. b) Charge transfer across a superconductor normal interface occurs via Andreev reflection, in which an incident electron is converted into a reflected hole while a Cooper pair is added to the superconducting condensate. Adapted from [27].

1.2 Josephson Junctions

The Josephson junction is one of the most important superconducting devices, consisting of two superconducting electrodes separated by a weak link [8, 39]. This weak link can be an insulating barrier, a normal metal, or a geometrical constriction in the superconductor itself. For tunnel junctions, quantum mechanical tunnelling of Cooper pairs across the barrier enables a dissipationless supercurrent that depends on the quantum phase difference between the two electrodes. In the case of normal metals and constriction type junctions the phenomenon is described by Andreev reflections, but the consequence is always the formation of a supercurrent [8, 27, 40].

1.2.1 The Josephson Effect

The Josephson effect arises from the transport of Cooper pairs between two superconductors separated by a weak link, Fig. 1.4. To understand this phenomenon, we first consider the tunnelling

case in which the superconducting state is described by a macroscopic quantum wavefunction, initially neglecting the Andreev reflections:

$$\psi(\mathbf{r}) = |\psi(\mathbf{r})|e^{j\phi(\mathbf{r})} \tag{1.2.1}$$

where $\phi(\mathbf{r})$ is the phase of the wavefunction. The supercurrent density can be related to the gradient of this phase through:

$$\mathbf{J}_s = \frac{q\hbar n_s}{m}\nabla\phi - \frac{q^2 n_s}{m}\mathbf{A} \tag{1.2.2}$$

where $\mathbf{A}$ is the vector potential of the magnetic field. In a Josephson junction, the weak link creates a region where the Cooper pair density is greatly reduced. To maintain a continuous supercurrent, the phase gradient must increase in this region, leading to a finite phase difference between the two electrodes. Defining the gauge invariant phase difference as:

$$\gamma = \phi_2 - \phi_1 - \frac{q}{\hbar}\int_1^2 \mathbf{A}\cdot d\mathbf{l} \tag{1.2.3}$$

the supercurrent through the junction can be expressed as a periodic function of γ. Using symmetry arguments (time-reversal symmetry requires $I_s(\gamma) = -I_s(-\gamma)$), the most general form is:

$$I_s(\gamma) = \sum_{n=1}^{\infty} I_{c,n}\sin(n\gamma) \tag{1.2.4}$$

This equation remains valid for superconductor-normal-superconductor (SNS) junctions. In this case, however, it is no longer appropriate to describe transport in terms of tunnelling. Instead, the transfer of Cooper pairs between the two superconductors is mediated by coherent transport through the normal region. To illustrate this mechanism, we first consider a single interface between a superconductor and a normal metal (see Fig. 1.4(b)). Andreev reflection is the process by which an electron incident from the normal region is retroreflected as a hole at the superconducting interface, while a Cooper pair is simultaneously transferred into the superconductor [27, 40]. When the normal region is sandwiched between two superconductors, the retroreflected hole can undergo a subsequent Andreev reflection at the opposite interface, being converted back into an electron. Repeated Andreev reflections at the two interfaces allow this process to continue coherently, giving rise to a dissipationless supercurrent across the junction (see Fig. 1.4(b)). Provided phase coherence is preserved, these processes lead to the formation of discrete, localised energy states within the normal region, known as Andreev bound states. The interested reader can see the calculations in [41]. For most junctions, the first harmonic dominates, yielding the first Josephson equation:

$$I_s = I_c\sin\gamma \tag{1.2.5}$$

where I_c is the critical current of the junction, the maximum supercurrent that can flow without voltage drop. Taking the time derivative of the gauge invariant phase difference and using Faraday's law:

$$\frac{d\gamma}{dt} = \frac{d\phi_2}{dt} - \frac{d\phi_1}{dt} - \frac{q}{\hbar}\frac{d}{dt}\int_1^2 \mathbf{A} \cdot d\mathbf{l} \tag{1.2.6}$$

From quantum mechanics, the time derivative of the phase is related to the energy by $\hbar\frac{d\phi}{dt} = E$. For Cooper pairs with charge $2e$, the energy difference corresponds to the electrical potential difference: $E_2 - E_1 = 2eV$. The time derivative of the vector potential integral gives the induced voltage. Combining these, we obtain the second Josephson equation:

$$\frac{d\gamma}{dt} = \frac{2\pi}{\Phi_0}V = \frac{2eV}{\hbar} \tag{1.2.7}$$

These two equations, Eqs. (1.2.5) and (1.2.7), known as the Josephson relations, can be used to describe the DC and AC Josephson effects.

DC Josephson Effect

When no voltage is applied across the junction ($V = 0$), a supercurrent can flow with magnitude up to I_c, determined only by the phase difference. This demonstrates that Cooper pairs can travel through the barrier without dissipation, carrying current in the absence of any voltage.

AC Josephson Effect

When a DC voltage V is applied, the phase difference increases linearly with time: $\gamma(t) = \gamma_0 + \frac{2eV}{\hbar}t$. Substituting into the first Josephson equation:

$$I_s(t) = I_c \sin\left(\gamma_0 + \frac{2eV}{\hbar}t\right) = I_c \sin(\gamma_0 + 2\pi f_J t) \tag{1.2.8}$$

where the Josephson frequency is:

$$f_J = \frac{2eV}{h} = K_J V \tag{1.2.9}$$

with the Josephson constant $K_J = 2e/h \approx 483.6$ GHz/mV [22, 23]. The supercurrent oscillates at this frequency, which is directly proportional to the applied voltage. This precise relationship between frequency and voltage, dependent only on fundamental constants, forms the basis for voltage standards in metrology.

Shapiro steps

We consider a Josephson junction subject to an external voltage bias consisting of a DC component and an AC drive,

$$V(t) = V_0 + V_1 \cos(\omega_1 t) \tag{1.2.10}$$

The temporal evolution of the superconducting phase difference $\gamma(t)$ across the junction is governed by the second Josephson relation,

$$\frac{d\gamma}{dt} = \frac{2\pi}{\Phi_0} V(t) \tag{1.2.11}$$

where $\Phi_0 = h/2e$ is the superconducting flux quantum. Substituting Eq. (1.2.10) into Eq. (1.2.11) and integrating over time yields

$$\gamma(t) = \gamma_0 + \frac{2\pi}{\Phi_0} V_0 t + \frac{2\pi V_1}{\Phi_0 \omega_1} \sin(\omega_1 t) \tag{1.2.12}$$

where γ_0 is an integration constant corresponding to the initial phase difference.

The supercurrent flowing through the junction is given by the first Josephson relation,

$$I_s(t) = I_c \sin \gamma(t) \tag{1.2.13}$$

which, upon substitution of Eq. (1.2.12), becomes

$$I_s(t) = I_c \sin \left[\gamma_0 + \frac{2\pi V_0}{\Phi_0} t + \frac{2\pi V_1}{\Phi_0 \omega_1} \sin(\omega_1 t) \right] \tag{1.2.14}$$

The argument of the sine function contains a sinusoidally modulated phase and can be expanded using the Jacobi-Anger identities applied to Eq. (1.2.14) [9, 22, 23]

$$I_s(t) = I_c \sum_{n=-\infty}^{\infty} (-1)^n J_n \left(\frac{2\pi V_1}{\Phi_0 \omega_1} \right) \sin \left[\gamma_0 + \left(\frac{2\pi V_0}{\Phi_0} - n\omega_1 \right) t \right] \tag{1.2.15}$$

where J_n denotes the Bessel functions of the first kind. From Eq. (1.2.15), it is evident that the supercurrent generally oscillates in time. However, a non-zero DC component of the supercurrent arises when the time dependent argument of the sine vanishes, i.e.,

$$\frac{2\pi V_0}{\Phi_0} - n\omega_1 = 0 \tag{1.2.16}$$

This phase locking condition yields discrete voltage values

$$V_0 = n \frac{\Phi_0 \omega_1}{2\pi} = n f_1 \Phi_0 \tag{1.2.17}$$

where $f_1 = \omega_1/2\pi$ is the frequency of the applied microwave drive. These quantized voltages correspond to the appearance of constant voltage plateaus in the current voltage characteristic, known as Shapiro steps.

The amplitude of the DC supercurrent associated with the nth Shapiro step is determined by the corresponding Bessel coefficient. The width of the step in current is therefore given by

$$|I_n| = 2I_c \left| J_n\left(\frac{2\pi V_1}{\Phi_0 \omega_1}\right)\right| \tag{1.2.18}$$

This result shows that the number and width of observable Shapiro steps depend sensitively on the amplitude of the AC drive, following the characteristic oscillatory behaviour of Bessel functions. Physically, Shapiro steps originate from a phase locking mechanism between the intrinsic Josephson oscillations and the external microwave drive [22, 23, 42]. When the average voltage across the junction satisfies Eq. (1.2.17), the phase difference evolves synchronously with the drive, such that the phase advances by exactly $2\pi n$ during each period of the microwave signal. In the tilted washboard potential picture, this corresponds to a particle moving down the potential while undergoing oscillations that are perfectly synchronized with transitions across an integer number of potential wells per drive cycle, see Fig. 1.5. For voltage biases not fulfilling the locking condition, the supercurrent oscillates in time and averages to zero over a period, resulting in a linear current voltage characteristic determined solely by the normal state contribution. When the junction is instead biased by a current source, the full resistively and capacitively shunted junction (RCSJ) model must be solved numerically; an example is reported in Fig. 1.5(a). Similar quantized voltage steps appear in the IV characteristics, with their behavior strongly influenced by the junction damping and the amplitude of the RF drive.

1.2.2 The RCSJ Model

The Resistively and Capacitively Shunted Junction (RCSJ) model [4, 9] provides a complete description of the current-voltage characteristics of Josephson junctions by including dissipative and reactive elements in parallel with the ideal Josephson element. The total current through the junction is:

$$I = I_c \sin\gamma + \frac{V}{R} + C\frac{dV}{dt} \tag{1.2.19}$$

where R represents the residual normal state resistance and C is the junction capacitance.

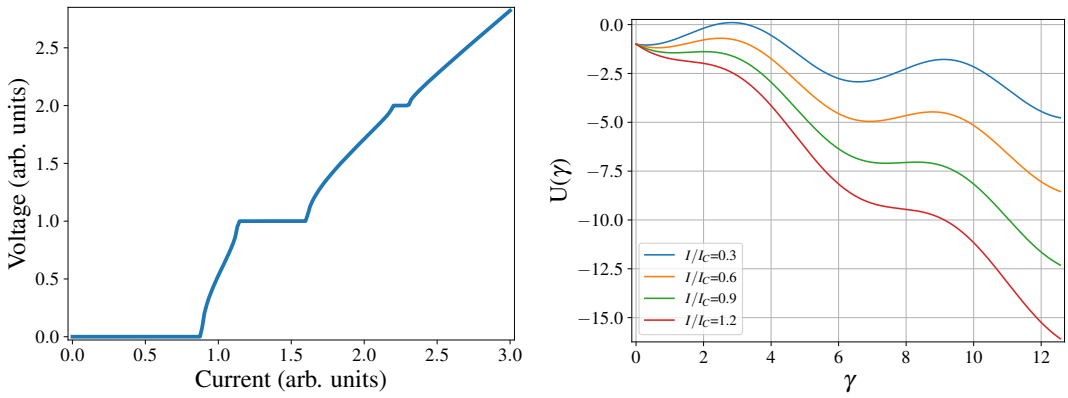

(a) (b)

Figure 1.5: (a) Current voltage characteristic of a Josephson junction under AC drive, showing the emergence of Shapiro steps. (b) Tilted washboard potential as described by Eq. 1.2.21 for different bias currents.

Using the second Josephson equation, this becomes:

$$I = I_c \sin\gamma + \frac{\Phi_0}{2\pi R}\frac{d\gamma}{dt} + C\frac{\Phi_0}{2\pi}\frac{d^2\gamma}{dt^2} \tag{1.2.20}$$

This equation is analogous to that of a nonlinear damped pendulum, where γ plays the role of the angular displacement. The "restoring force" is $I - I_c \sin\gamma$, which derives from the tilted washboard potential:

$$U(\gamma) = -\frac{\Phi_0}{2\pi}(I\gamma + I_c \cos\gamma) \tag{1.2.21}$$

The potential landscape changes as the bias current increases. For $I < I_c$, the potential has local minima where the phase can be trapped. At $I = I_c$, these minima disappear, and for $I > I_c$, the phase runs continuously, corresponding to a voltage state, see Fig. 1.5.

Stewart-McCumber Parameter

The dynamics of the junction are characterized by the Stewart-McCumber parameter:

$$\beta_c = \frac{2\pi I_c R^2 C}{\Phi_0} \tag{1.2.22}$$

This dimensionless parameter determines the degree of damping:

- **Overdamped regime ($\beta_c < 1$):** The capacitive term is negligible. The voltage response to current is non-hysteretic. When I exceeds I_c, the junction switches immediately to a voltage state and returns to the zero voltage state when I drops below I_c.

- **Underdamped regime ($\beta_c > 1$):** The capacitive term is significant, leading to hysteretic behavior. When I exceeds I_c, the junction switches to a voltage state but remains there even when I is reduced below I_c, returning to the zero voltage state only when I drops to the retrapping current $I_r \approx 4I_c/(\pi\sqrt{\beta_c})$ [9, 24].

- **Critically damped ($\beta_c \approx 1$):** This regime provides the fastest switching with slight hysteresis.

The quality factor of the junction damping is related to β_c by:

$$Q = \sqrt{\beta_c} = \omega_p RC \tag{1.2.23}$$

where $\omega_p = \sqrt{2\pi I_c/(\Phi_0 C)}$ is the plasma frequency of the junction.

1.3 Electronics based on Josephson Junctions

1.3.1 SQUID

A SQUID is a Superconducting QUantum Interference Device that combines the properties of Josephson junctions with flux quantization [4, 43, 44]. Its applications range from magnetic field sensors to circuit components in circuit quantum electrodynamics (QED). This device is composed of a superconducting loop interrupted by two Josephson junctions, as shown in Fig. 1.6. In the lumped-element approximation, each junction can be modelled as an ideal Josephson element shunted by a resistor and a capacitor, while the loop contributes an inductance. So the basic equations describing it are [4]:

$$\frac{I}{2} \pm J = I_{0,k} f(\gamma_k) + \frac{\Phi_0}{2\pi R_k}\dot{\gamma_k} + \frac{\Phi_0}{2\pi} C_k \ddot{\gamma_k} \tag{1.3.1}$$

$$\gamma_2 - \gamma_1 = \frac{2\pi}{\Phi_0}(\Phi_{ext} + LJ) \tag{1.3.2}$$

where Φ_0 is the flux quantum, L is the geometrical inductance of the loop, J is the circulating current and Φ_{ext} is the external flux. The response of the SQUID critical current to bias and flux is shown in Fig. 1.6 for the case $L = 0$, i.e. for a vanishing screening parameter β_L. The modulation can be used together with the previous equations to extract the CPR of an unknown junction if it is paired with a junction of much larger critical current [45]. Since their introduction, SQUIDs have

been used to measure magnetisation, susceptibility, and hysteresis of small samples across wide temperature and magnetic field ranges [4]. These instruments have become indispensable tools in condensed matter physics, chemistry, and materials science. The integration of cryocoolers into such systems has significantly reduced the complexity associated with cryogenic operation, making SQUID based measurements more accessible outside specialised low temperature laboratories [4]. In many of the applications discussed thus far, the ultimate goal is not only the measurement of magnetic fields, but the inference of the electrical currents that give rise to them. This requires solving inverse problems in which current distributions are reconstructed from measured magnetic field maps [4]. SQUIDs are widely employed as ultra low noise amplifiers [44]. By coupling an input signal through a superconducting transformer to the SQUID loop, quasistatic voltages and currents can be measured with exceptional sensitivity. These measurements can be extended to frequencies of several megahertz [4]. A particularly important application is the detection of nuclear magnetic resonance and nuclear quadrupole resonance signals at low frequencies, where conventional inductive techniques are inefficient [4]. At higher frequencies, SQUIDs function as microwave amplifiers with high gain and near quantum limited noise performance. By engineering the input circuit appropriately, SQUID amplifiers have been demonstrated up to several gigahertz [46] and play a key role in the readout of cryogenic axion detectors [47]. Miniaturised SQUIDs (nanoSQUIDs), typically based on nanobridge junctions defined by focused ion beam (FIB) milling or electron beam lithography, have extended these capabilities to the nanoscale, down to the detection of single magnetic nanoparticles [48–51]. Finally, SQUIDs occupy a unique position in fundamental physics and quantum technology. Their sensitivity has enabled experiments probing nonequilibrium superconductivity, charge imbalance phenomena, and macroscopic quantum coherence. In modern superconducting quantum circuits, SQUIDs serve not only as sensors but also as tunable circuit elements. By controlling the magnetic flux threading a SQUID loop, one can dynamically modify effective inductances, resonance frequencies, and coupling strengths. This capability is used in a wide range of quantum devices, including flux qubits [52], parametric amplifiers [53], and tunable resonators [4, 54].

1.3.2 Transmon qubit

A qubit (quantum bit) is a controllable quantum two level system that constitutes the fundamental building block of quantum computation. With its ability to exist in coherent superpositions of

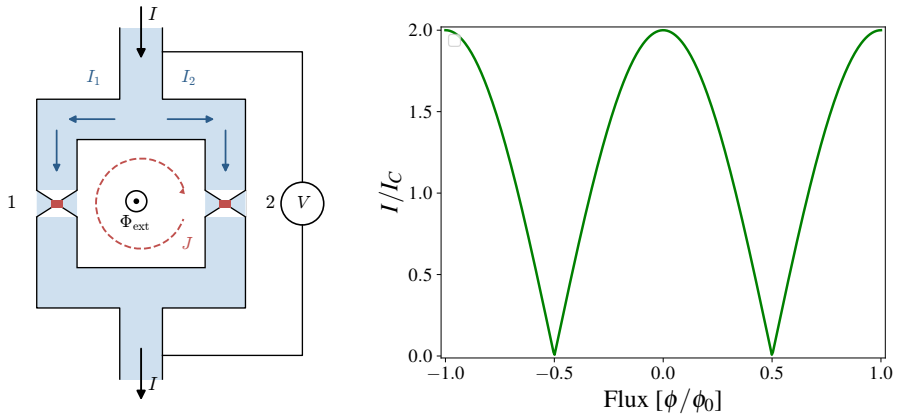

(a) (b)

Figure 1.6: (a) Superconducting Quantum Interference Device (SQUID). I represents the current supplied to the device, while the numbers 1 and 2 represent the two Josephson junctions, and H is the applied magnetic field. b) Example of SQUID critical current modulation, computed for $L = 0$ ($\beta_L = 0$). Adapted from [4].

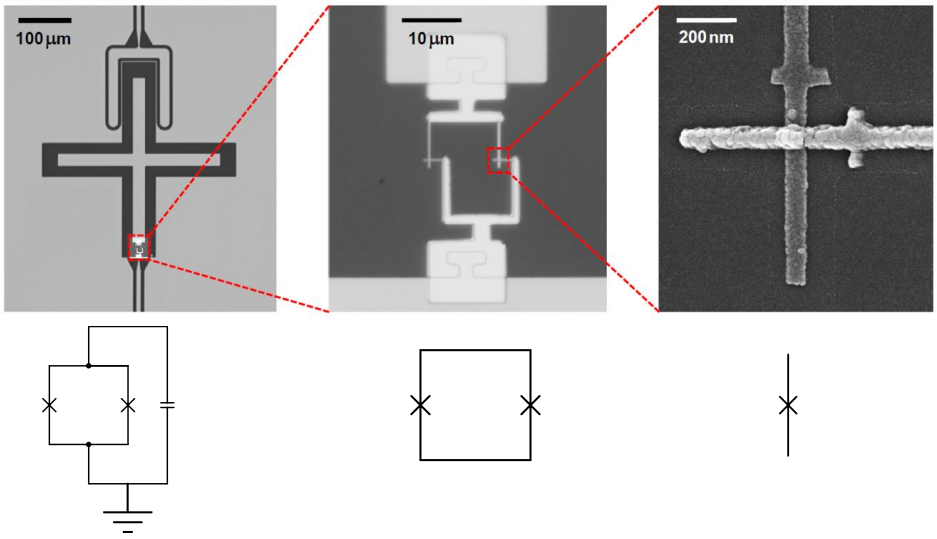

Figure 1.7: Transmon qubit, real device (up) and lumped model (down). A transmon qubit is created by shunting a SQUID with a capacitance. In this way the parameters of the Hamiltonian in Eq. (1.3.3) can be tailored to design a qubit which is controllable and resistant to noise. Adapted from [10].

the logical states 0 and 1, a qubit enables the implementation of quantum algorithms that can outperform their classical counterparts for specific computational tasks [55]. In the framework

of circuit Quantum Electrodynamics (cQED), qubits are realized using superconducting circuits, where Josephson junctions provide the essential nonlinearity required to isolate and control discrete quantum levels. One of the most widely adopted superconducting qubit architectures is the transmon qubit [10]. As shown in Fig. 1.7, a transmon consists of a superconducting quantum interference device (SQUID) shunted by a large capacitance. This configuration allows for tunability of the effective Josephson energy via an external magnetic flux, while simultaneously suppressing sensitivity to charge noise. The shunt capacitance plays a crucial role in reducing the charging energy, thereby stabilizing the qubit against fluctuations of the offset charge. The Hamiltonian of the transmon qubit can be written as

$$\hat{H} = 4E_C(\hat{n} - n_g)^2 - E_{J,1}f(\hat{\gamma}_1) - E_{J,2}f(\hat{\gamma}_2) \tag{1.3.3}$$

where $E_C = e^2/2C$ is the charging energy associated with the total shunt capacitance C, and $E_{J,i}$ are the Josephson energies of the two junctions forming the SQUID. The Josephson energy is defined as

$$E_J = \frac{\hbar I_c}{2e} \tag{1.3.4}$$

with I_c the critical current of the junction. The Josephson junction thus behaves as a nonlinear inductive element with effective inductance

$$L_J = \frac{\hbar}{2eI_c} \tag{1.3.5}$$

The operators $\hat{n}$ and $\hat{\gamma}$ satisfy the canonical commutation relation $[\hat{\gamma}, \hat{n}] = i$. The parameter n_g denotes the offset charge. In the limit where the current phase relation of each junction is well approximated by a sinusoidal form, $f(\hat{\gamma}_i) \simeq \cos\hat{\gamma}_i$, and for critical currents of the order of a few tens of nanoamperes, the transmon operates at transition frequencies in the GHz range. A defining characteristic of the transmon is its operation in the regime $E_J \gg E_C$, which exponentially suppresses charge dispersion and strongly reduces sensitivity to charge noise. Although increasing E_J/E_C lowers the anharmonicity of the spectrum, a suitable balance between these two energy scales allows for anharmonicities on the order of several hundred MHz, sufficient to selectively address the $0 \leftrightarrow 1$ transition without populating higher excited states. Fig. 1.8 illustrates the evolution of the energy levels of a transmon qubit as a function of the ratio E_J/E_C. Larger Josephson energies reduce the dependence of the transition frequencies on the offset charge n_g, as reflected by the reduced slope of the energy bands. The design of the Josephson junction must

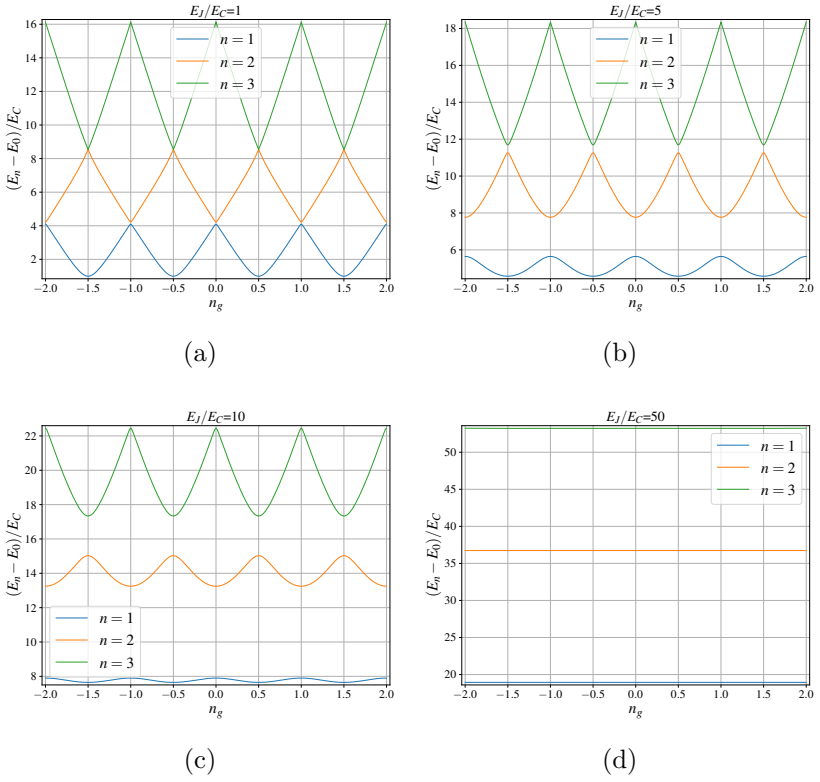

Figure 1.8: The energy levels of a Transmon qubit at different ratios of Josephson and charge energy are shown. Higher charging energy results in higher anharmonicity, but also high sensitivity to charge noise n_g (proportional to the slope of the curve). Therefore, it is important to find the right ratio of E_J and E_C to reduce noise and maintain high anharmonicity. Adapted from [10].

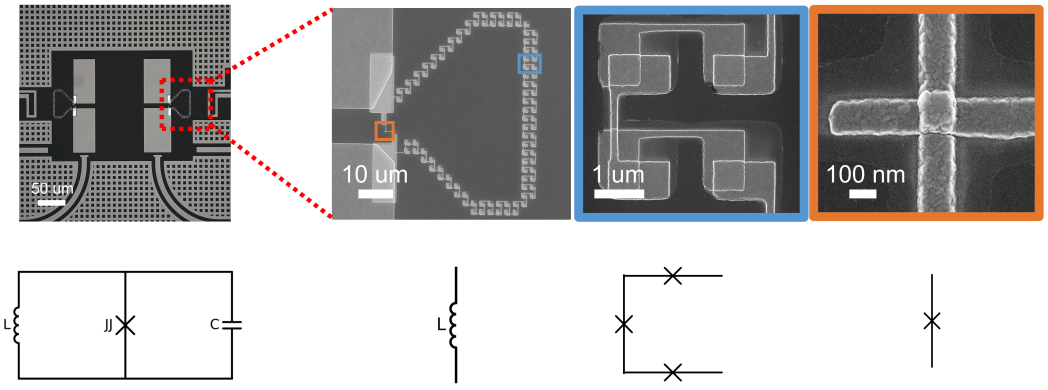

Figure 1.9: Fluxonium, real device (up), and lumped model (down). Adapted from [56].

therefore target critical currents that place the device in the optimal regime, combining low noise sensitivity with sufficient anharmonicity for high fidelity qubit control.

1.3.3 Fluxonium qubit

Josephson junctions also constitute the fundamental nonlinear element of a different class of superconducting qubits, among which the fluxonium qubit has emerged as a particularly promising architecture due to its long coherence times and strong anharmonicity [56–59]. In contrast to the transmon, where charge noise is suppressed by operating in the regime $E_J \gg E_C$ which significantly reduces anharmonicity, the fluxonium qubit achieves noise protection by shunting a small Josephson junction with a large inductance, named superinductance. A schematic representation of the fluxonium circuit consists of a single Josephson junction with Josephson energy E_J and capacitance C, shunted by a large inductance L made of a series of Josephson junctions, see Fig. 1.9. In practice, this superinductance is realized using an array of Josephson junctions, which behaves as a linear inductive element. The Hamiltonian of the fluxonium qubit reads

$$\hat{H} = 4E_C\hat{n}^2 + \frac{1}{2}E_L\hat{\gamma}^2 - E_J\cos\left(\hat{\gamma} - \gamma_{\text{ext}}\right) \tag{1.3.6}$$

where $E_C = e^2/2C$ is the charging energy, E_J is the Josephson energy of the small junction, and

$$E_L = \left(\frac{\Phi_0}{2\pi}\right)^2 \frac{1}{L} \tag{1.3.7}$$

is the inductive energy associated with the shunt inductance. The external reduced flux is

$$\gamma_{\text{ext}} = \frac{2\pi\Phi_{\text{ext}}}{\Phi_0} \tag{1.3.8}$$

The Hamiltonian in Eq. (1.3.6) illustrates the role of the Josephson junction in the fluxonium circuit. The Josephson term introduces the nonlinearity required for qubit operation, while the inductive term provides a quadratic potential that introduces a further degree of anharmonicity [58]. The resulting potential energy,

$$U(\gamma) = \frac{1}{2}E_L\gamma^2 - E_J\cos(\gamma - \gamma_{\text{ext}}) \tag{1.3.9}$$

depends on the external magnetic flux and presents multiple local minima whose position and depth can be controlled experimentally. The sensitivity of the circuit to charge noise is reduced due to the fact that an offset charge affects all the energy levels compared to the transmon where only the lowest ones are affected, allowing long coherence times to be achieved [58]. Moreover, compared to the transmon qubit, which relies on large E_J/E_C ratios to reduce charge sensitivity but has weak anharmonicity, the fluxonium operates in a different regime where strong anharmonicity and noise protection are obtained simultaneously [59] even for smaller ratios.

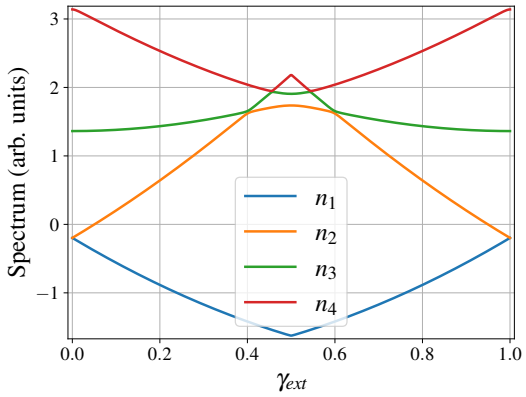

Figure 1.10: Fluxonium energy levels for $E_J = 4$ GHz, $E_C = 0.5$ GHz, $E_L = 0.1$ GHz.

1.3.4 Single Flux Quantum (SFQ) electronics

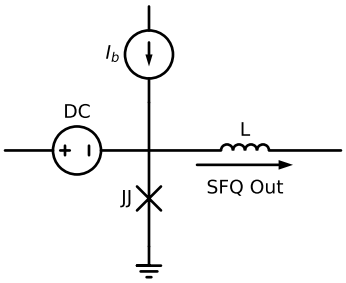

Figure 1.11: SFQ circuit model, a DC pulse at the input generates an SFQ pulse at the output. Adapted from [25].

Josephson junctions are used for ultrafast and energy efficient digital logic through Single Flux Quantum (SFQ) electronics [5, 24, 25, 60]. In SFQ circuits, information is encoded in voltage pulses whose time integral is quantized and equal to a single magnetic flux quantum,

$$\int V(t)\,dt = \Phi_0 \tag{1.3.10}$$

These pulses serve as digital bits and can be processed at clock frequencies exceeding tens of gigahertz, with power dissipation orders of magnitude lower than that of conventional CMOS technologies [24]. SFQ electronics provide a platform for classical control and readout of superconducting quantum circuits. Their compatibility with Josephson junction based qubits makes them particularly attractive for scalable cryogenic control architectures, where low dissipation and high speed operation are essential. The integration of SFQ logic with qubit devices therefore represents a promising route to large scale superconducting quantum processors. A basic SFQ pulse gener-

ator is shown schematically in Fig. 1.11. The Josephson junctions are biased with a DC current slightly below their critical current I_c, such that they initially remain in the superconducting (zero voltage) state. When an input current signal I_b temporarily raises the total current through the junction above I_c, the junction switches to a resistive state, producing a sharp voltage pulse. Due to the Josephson relation between voltage and phase evolution, this switching event corresponds to a 2π phase slip, resulting in the emission of a voltage pulse with quantized area equal to Φ_0. The typical duration of an SFQ pulse is on the order of picoseconds. The generation of SFQ pulses does not rely on an ideal sinusoidal current phase relation. In [25, 60], the circuit was simulated using a skewed current phase relation characteristic of nanobridge Josephson junctions, demonstrating that robust SFQ pulse generation persists even in the presence of higher harmonics. This result highlights the suitability of nanobridge junctions for SFQ applications, offering the potential to reduce both the device footprint and the fabrication complexity compared to conventional tunnel junction technologies.

1.4 Motivation for Nanobridge Josephson Junctions

The discussion presented in this chapter has highlighted the central role of Josephson junctions in superconducting electronics and quantum technologies. In this context, tunnel junctions have established themselves as a highly successful and widely adopted platform. However, several intrinsic limitations of this technology become increasingly relevant when targeting improved coherence, device miniaturization, and large scale integration. In particular, the presence of the amorphous oxide barrier introduces microscopic defects that act as two-level systems (TLSs), contributing to dissipation and decoherence in quantum circuits [13, 14]. At the same time, the exponential sensitivity of the tunneling current to barrier thickness imposes stringent fabrication constraints, affecting device reproducibility and scalability. The non negligible capacitance associated with the insulating layer further complicates circuit design, especially in applications requiring precise control of dynamical regimes. These considerations motivate the exploration of alternative Josephson junction implementations that can mitigate such limitations. Nanobridge Josephson junctions represent a conceptually simple yet powerful approach, in which the weak link is defined by a narrow superconducting constriction rather than an insulating barrier. This geometry inherently removes the oxide layer, thereby reducing TLS losses and significantly lowering parasitic

capacitance. In addition, nanobridge junctions are compatible with simplified fabrication processes and more compact device layouts, making them attractive for scalable superconducting circuits. Despite these advantages, the behavior of nanobridge junctions is more strongly influenced by geometry, dimensionality, and material properties than in conventional tunnel junctions. As a result, their design cannot rely on simple lumped element descriptions alone, and a deeper understanding based on realistic three-dimensional models is required. For these reasons, the remainder of this work is dedicated to the systematic investigation of nanobridge Josephson junctions. The next chapter introduces the theoretical framework and numerical methods used to model their behavior in realistic geometries. This is followed by the development of nanofabrication processes for the realization of such devices, and by their experimental characterization through transport and microwave measurements. Together, these elements aim to establish a coherent and practical approach to the design and integration of nanobridge junctions in superconducting circuits.

2. Theory and Simulations of the Nanobridge junction

This chapter presents the theoretical framework and the numerical model developed in this thesis to design nanobridge Josephson junctions. As discussed in Chapter 1, the properties of a nanobridge depend strongly on its materials and geometry, so a numerical model is needed before fabrication. The model must satisfy a few requirements set by the target applications. Superconducting qubits require junctions with small critical currents, of the order of 10 to 100 nA, and current phase relations (CPRs) as close as possible to a sinusoid, in order to obtain sufficient anharmonicity; fluxonium qubits in particular require critical currents below about 50 nA [2, 59, 61]. For SFQ circuits, larger critical currents are acceptable, but the shape of the CPR still affects the generation of the pulses [25, 60]. Moreover, to remain in the Josephson regime, the length of the bridge should not exceed about three times the superconducting coherence length [8]. The relevant dimensions are therefore of the order of the coherence length, which ranges from a few nanometres in the nitride films to about 100 nm in aluminium. The simulated devices in this chapter have widths and lengths of a few tens of nanometres (for example $W = 0.5\xi$ and $L = 2\xi$, or $W = 20$ nm and $L = 60$ nm in the multilayer SNS and SS'S junctions), comparable to the nanobridges fabricated in Chapter 3, whose lateral dimensions are also of a few tens of nanometres.

Previous models of nanobridge junctions were limited in several ways. The analytical KO-1 and KO-2 models [62, 63] describe only a one-dimensional bridge with rigid boundary conditions at its ends, and therefore neglect the suppression of the order parameter in the electrodes. Numerical solutions of the Usadel equations have been obtained for single-material bridges in two dimensions, or in three dimensions reduced to an effective two-dimensional problem using cylindrical symmetry [18], and for specific SN-N-NS geometries [17, 64, 65]. A general three-dimensional solution has also been reported [19], but it was not applied to quantum technologies. The model developed in this work differs from these approaches in three main aspects: it solves the Usadel equations in arbitrary three-dimensional geometries, including the rounded edges produced by the etching process; it can include several different materials, coupled by the boundary conditions at each interface, so that realistic multilayer stacks, such as the nitride/Nb/Al/Nb stacks of Chapter 3, can be simulated; and its output, the CPR, can be used directly in the standard design tools for

superconducting circuits to compute qubit spectra.

The chapter is organised as follows. Sections 2.1 and 2.2 review the Green's function formalism and the quasi-classical approximation that lead to the Usadel equations, mainly following Ref. [66] and partially Refs. [67, 68]. Section 2.3 introduces nanobridge junctions and the previous theoretical work. From Section 2.4, I present my own work [2]: the finite element implementation of the Usadel equations, its validation against analytical, numerical and experimental benchmarks, and its application to multilayer junctions and to the energy levels of nanobridge based qubits.

2.1 The Green Function

The formulation of superconductivity theory employing the Green function formalism is a powerful tool in quantum field theory because it allows for an easier set of equations to work with, and with the right set of approximation it is possible to cast them in a transport like equation which will then be suitable for numerical simulations. The starting point is the Hamiltonian describing the dynamics of electrons in a superconductor:

$$\hat{H} = \hat{H}_0 + \hat{V}_1 + \hat{V}_2 \tag{2.1.1}$$

$$\begin{aligned}\hat{H} = &\int d^3r \hat{\psi}^\dagger_\alpha(\mathbf{r},\tau)\left[-\frac{1}{2m}\left(\nabla - \frac{ie}{c}\mathbf{A}(\mathbf{r})\right)^2 - \mu\right]\hat{\psi}_\alpha(\mathbf{r},\tau) \\ &+ \sum_a \int d^3r \hat{\psi}^\dagger_\alpha(\mathbf{r},\tau)U(\mathbf{r}-r_a)\hat{\psi}_\alpha(\mathbf{r},\tau) \\ &- \frac{g}{2}\int d^3r \hat{\psi}^\dagger_\beta(\mathbf{r},\tau)\hat{\psi}^\dagger_\alpha(\mathbf{r},\tau)\hat{\psi}_\alpha(\mathbf{r},\tau)\hat{\psi}_\beta(\mathbf{r},\tau)\end{aligned} \tag{2.1.2}$$

Where $U(\mathbf{r}-r_a)$ is the potential due to impurities in the material and the last term is the coupling term between 2 electrons that gives rise to superconductivity, while $\tau = it$ is the imaginary time. The subscripts α and β denote the spin. Note that the impurity potential $U(\mathbf{r}-r_a)$ in Eq. (2.1.2) does not depend on spin: it describes only potential (non-magnetic) scattering, which conserves the electron spin, and the Hamiltonian contains no spin-flip or spin orbit scattering terms. This is a good approximation for the materials considered in this thesis (Al, Nb, NbN and TiN), which do not contain magnetic impurities in significant concentration. Non-magnetic impurities do not break time-reversal symmetry and, according to Anderson's theorem, do not change T_c or the gap of a conventional superconductor [69]; this is why disorder enters the theory only through the mean free time τ and, in the dirty limit, through the diffusion coefficient. Scattering by magnetic impurities

would instead require an additional exchange term of the form $\sum_a \int d^3r\, \hat{\psi}^\dagger_\alpha J(\mathbf{r}-r_a)\, \mathbf{S}_a \cdot \boldsymbol{\sigma}_{\alpha\beta}\, \hat{\psi}_\beta$, where $\mathbf{S}_a$ is the impurity spin and $\boldsymbol{\sigma}$ the vector of Pauli matrices. This term breaks time-reversal symmetry, acts as a pair-breaking mechanism with a spin-flip scattering rate $1/\tau_s$, and suppresses both T_c and the gap [70]; in the Usadel equations it would appear as an additional pair-breaking term proportional to $1/\tau_s$. It is useful to introduce the anticommutation relations and the time evolution equations:

$$\left\{\hat{\psi}_\alpha(r_1,\tau), \hat{\psi}^\dagger_\beta(r_2,\tau)\right\} = \delta_{\alpha,\beta}\delta^{(3)}(r_1-r_2) \tag{2.1.3}$$

$$\left\{\hat{\psi}_\alpha(r_1,\tau), \hat{\psi}_\beta(r_2,\tau)\right\} = \left\{\hat{\psi}^\dagger_\alpha(r_1,\tau), \hat{\psi}^\dagger_\beta(r_2,\tau)\right\} = 0 \tag{2.1.4}$$

$$\frac{\partial\hat{\psi}_\alpha}{\partial\tau} = \left[\hat{H}, \hat{\psi}_\alpha\right] \qquad \frac{\partial\hat{\psi}^\dagger_\alpha}{\partial\tau} = \left[\hat{H}, \hat{\psi}^\dagger_\alpha\right] \tag{2.1.5}$$

and to introduce the two regular and anomalous Green's Functions:

$$G_{\alpha,\beta} = -\langle\hat{T}_r\hat{\psi}_\alpha(r_1,\tau_1)\hat{\psi}^\dagger_\beta(r_2,\tau_2)\rangle \qquad F_{\alpha,\beta} = \langle\hat{T}_r\hat{\psi}_\alpha(r_1,\tau_1)\hat{\psi}_\beta(r_2,\tau_2)\rangle \tag{2.1.6}$$

where $\hat{T}_r$ is the time ordering operator, $\langle ...\rangle$ is the average over the grand canonical ensemble $\mathrm{tr}\{\exp[\beta(\Omega-\hat{H})]...\}$, and obviously Ω is the grand canonical potential and $\beta = 1/T$. One can prove using all the above equations and Wick's theorem [71], that

$$\begin{pmatrix} -\frac{\partial}{\partial\tau_1} - \mathcal{H} & \Delta(r_1) \\ -\Delta^*(r_1) & \frac{\partial}{\partial\tau_1} - \mathcal{H}^* \end{pmatrix} \breve{G} = I\delta^{(3)}(r_1-r_2) \tag{2.1.7}$$

Where

$$\mathcal{H} = -\frac{1}{2m}\left(\nabla - \frac{ie}{c}\mathbf{A}(\mathbf{r})\right)^2 - \mu + \sum_a U(r_1-r_a) \tag{2.1.8}$$

$$\breve{G} = \begin{pmatrix} G(r_1,\tau_1;r_2,\tau_2) & -F(r_1,\tau_1;r_2,\tau_2) \\ F^\dagger(r_1,\tau_1;r_2,\tau_2) & \bar{G}(r_1,\tau_1;r_2,\tau_2) \end{pmatrix} \tag{2.1.9}$$

$$G(r_1,\tau_1;r_2,\tau_2) = \langle\hat{T}_r\hat{\psi}^\dagger(r_1,\tau_1), \hat{\psi}(r_2,\tau_2)\rangle \tag{2.1.10}$$

and

$$\Delta(r_1) = g\langle\hat{T}_r\hat{\psi}(r_1,\tau_1), \hat{\psi}(r_1,\tau_1)\rangle = gF(r_1,\tau_1;r,\tau_1) \qquad \Delta^*(r_1) = gF^\dagger(r_1,\tau_1;r_1,\tau_1) \tag{2.1.11}$$

Similar equations can be obtained for variables r_2, τ_2. As the reader can see, we neglected the spin subscripts α, β because we are assuming that there is no potential acting on them. One other step is to consider the Fourier transformation of the matrix $\breve{G}$. To do that, let us first define

$$\tau = \tau_1 - \tau_2 \qquad T = \frac{(\tau_1 + \tau_2)}{2} \tag{2.1.12}$$

Since we are interested in the equilibrium problem, we can set $\frac{\partial}{\partial T} = 0$. Remembering that G is actually an average over the grand canonical ensemble of a system of electrons (fermions) one can prove that $G(\tau + \beta, r_1, r_2) = -G(\tau_0, r_1, r_2)$, so we can work on the interval $\tau \in [-\beta, \beta]$ and Fourier transform

$$G(\tau, r_1, r_2) = T \sum_{n=-\infty}^{\infty} e^{-i\omega_n \tau} G_{\omega_n}(r_1, r_2) \tag{2.1.13}$$

the same condition $G(\tau + \beta, r_1, r_2) = -G(\tau < 0, r_1, r_2)$ requires that $\omega_n = (2n+1)\pi T$, they are referred to as Matsubara frequencies, and are the poles of the Fermi-Dirac distribution. Eq.(2.1.7) thus becomes

$$\begin{pmatrix} i\omega_n - \mathcal{H} & \Delta(r_1) \\ -\Delta^*(r_1) & -i\omega_n - \mathcal{H}^* \end{pmatrix} \breve{G}_{\omega_n}(r_1, r_2) = I\delta^{(3)}(r_1 - r_2) \tag{2.1.14}$$

which is usually referred to as the Gorkov equation. A similar equation can be obtained for r_2.

2.2 Quasi-Classical Approximation

Since the temperature $T \sim 0$ and $\Delta \ll E_F$, where $E_F = \mu$ is the Fermi energy, the quasiparticle momentum p can be assumed to be close to the Fermi momentum p_F

$$\delta p \sim \frac{\xi_p}{v_F} \sim \xi^{-1} \tag{2.2.1}$$

where $\xi_p = E_n(p) - E_F = \frac{p^2}{2m} - \mu$, v_F is the Fermi velocity and ξ is the coherence length. We are considering the energy levels of an electron to be a quadratic function of momentum, effectively a kinetic energy, this is justified by the assumption that we are considering energies really close to the Fermi one and more complicated band structures can be neglected. We can now rewrite $\vec{p} \simeq \vec{p}_f$

$$\frac{d^3p}{(2\pi)^3} = \frac{d\xi_p}{v_F} \frac{d\Omega_F}{(2\pi)^3} \tag{2.2.2}$$

The quasi-classical approximation consists of integrating out $d\xi_p$ which is equivalent to assume that only the Fermi energy contributes to superconductivity and that the fast oscillations associated

with $r = r_1 - r_2$ do not contribute either. We are left only with the slow oscillations associated to $R = \frac{r_1+r_2}{2}$. We can consider new averaged Green's functions

$$\breve{g}(\vec{p}, R) = \frac{i}{\pi} \int d\xi_p \int d\vec{r} \breve{G}_{\omega_n}(\vec{R}, \vec{r}) e^{ip\vec{r}} = \begin{pmatrix} g(\vec{p}, \vec{R}) & -f(\vec{p}, \vec{R}) \\ f^\dagger(\vec{p}, \vec{R}) & \bar{g}(\vec{p}, \vec{R}) \end{pmatrix} \tag{2.2.3}$$

where g and f are defined similarly to the above integration for the single terms in the matrix. Substituting in the Gorkov equations we obtain the famous Eilenberger equations

$$i\vec{v}_f \cdot \breve{\partial}_R \breve{g} + \left[\breve{H}, \breve{g}\right] = \frac{1}{2i\tau} \left[\langle \breve{g} \rangle, \breve{g}\right] \tag{2.2.4}$$

which need to be completed with the self consistency equation for Δ:

$$\Delta \ln \frac{T}{T_c} + 2\pi T \sum_{\omega_n=0}^{\infty} \left(\frac{\Delta}{\omega_n} - \langle f \rangle \right) = 0 \tag{2.2.5}$$

and the normalization condition

$$\breve{g}^2 = 1 \tag{2.2.6}$$

that reads

$$g^2 + f f^\dagger = 1 \quad \text{and} \quad g + \bar{g} = 0 \tag{2.2.7}$$

where $\frac{1}{\tau} = 2\pi v_F |U|^2 n$ is the scattering mean free time, n is the electronic density, $\langle ... \rangle$ is the average over the Fermi surface, i.e. $\int \frac{d\Omega_F}{4\pi} ...$ and

$$\breve{H} = \begin{pmatrix} i\omega_n & \Delta \\ -\Delta^* & -i\omega_n \end{pmatrix} \tag{2.2.8}$$

$$\breve{\partial}_R = \begin{pmatrix} \nabla_R & \nabla_R - \frac{2ie}{c} A(R) \\ \left(\nabla_R - \frac{2ie}{c} A(R)\right)^* & \nabla_R \end{pmatrix} \tag{2.2.9}$$

The full calculation is beyond the scope of this thesis, but the interested reader can find it on pages 30 to 80 of Ref. [66].

2.2.1 The Usadel Equations

A further approximation to the Eilenberger equations consists in considering the superconductors to be in the dirty limit, i.e. $\xi \gg l$, where l is the electronic mean free path. In this case, scattering is strong enough to make the Green's functions nearly isotropic, so that the dependence on the direction of the Fermi velocity can be averaged out, giving [8, 38, 72]:

$$\Phi(\omega_n, \vec{r}) = \Delta(\vec{r}) + \xi^2 \frac{\pi T_{CS}}{\omega_n G} \vec{\nabla}(G^2 \vec{\nabla} \Phi(\omega_n, \vec{r})) \tag{2.2.10}$$

where $G = \frac{\omega_n}{\sqrt{\omega_n^2 + \Phi^2}}$. Φ is an auxiliary function which puts the partial differential equation (PDE) in a more convenient form, and ξ is the coherence length of the material, which is determined by its electronic diffusion coefficient $D = \frac{1}{3}\tau v_F^2$ through the expression $\xi = \sqrt{\hbar D / 2\pi k_B T_C}$. The self consistent equation then becomes

$$\Delta_S(\vec{r}) \ln \frac{T}{T_C} + 2\pi T \sum_{\omega_n}^{N} \left(\frac{\Delta(\vec{r})}{\omega_n} - \frac{G\Phi(\omega_n, \vec{r})}{\omega_n} \right) = 0 \tag{2.2.11}$$

2.2.2 Boundary conditions between 2 different materials

If we are in a condition where 2 materials either two superconductors (S-S') or a superconductor and a normal metal (N) are in contact with each other, the above equations need to be completed with boundary conditions:

$$\gamma_B \xi_{S'/N} G_{S'/N} \nabla \Phi_{S'/N} \cdot \vec{n} = G_S(\Phi_S - \Phi_{S'/N}) \tag{2.2.12}$$

$$\gamma_B \xi_S G_S \nabla \Phi_S \cdot \vec{n} = \gamma G_{S'/N}(\Phi_{S'/N} - \Phi_S) \tag{2.2.13}$$

where $\vec{n}$ is the normal at the boundary. Defining ρ_I as the resistivity of material I, $\gamma = \rho_S \xi_S / \rho_{S',N} \xi_{S',N}$ and $\gamma_B = R_B / \rho_{S',N} \xi_{S',N}$ represent the suppression parameter and the boundary resistance parameter, respectively. The suppression parameter describes how much the superconductivity is reduced going from S to a weaker (lower critical temperature) S' or N (no suppression means $\gamma = 0$), while the boundary resistance parameter describes the effect of the surface resistance (R_B) at the boundary between S and S'/N. Far from the boundary on the S surfaces not connected to the S'/N layer, this boundary condition is applied:

$$\Phi_S = \Delta_0 e^{\pm i\delta/2} \tag{2.2.14}$$

where $\Delta_0 = 1.76 k_B \cdot T_{CS}$ is the Bardeen-Cooper-Schrieffer (BCS) energy gap and δ is the phase [17]. When interested in electrical transport for a device consisting of single or multiple layers we must define the critical current flowing in the device as:

$$I_S \rho = \frac{\pi T A}{e} \sum_{n=0}^{N} Im\{G_I^2 \Phi_I^* \partial_x \Phi_I\}$$

where ρ is the resistivity of the layer in the normal state and A is the cross-sectional area.



(a) (b)

Figure 2.1: Two different types of nanobridge junctions: planar (a) and variable-thickness (b). The nanobridge is a type of Josephson junction where the connection between the two electrodes is a small constriction made of the same material or a different one. Typical dimensions of the constriction are a few tens of nanometer in length.

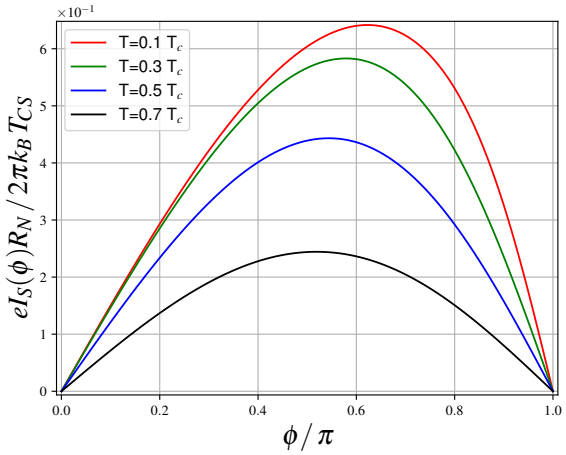

Figure 2.2: Current phase relationship (CPR) of a nanobridge junction in the limit of small length L, referred to as the KO-1 model [62].

2.3 Nanobridge junction

In this section, I will present a review of the most recent theoretical work on nanobridge junctions. As shown in Fig. 2.1, a nanobridge is a junction where the weak link is a small constriction of the same material (it can also be a different metal or semiconductor) connecting two superconducting electrodes. Let's focus for a moment on a junction made of one material. The first approximation is to consider a small bridge of length $L \ll \xi_S$. In this case, an analytical result exists in the dirty limit, which is referred to as the KO-1 model after Kulik and Omelyanchuk [8, 62]; the

corresponding result in the clean limit is known as the KO-2 model [8, 63]. The KO-1 current phase relation reads

$$I_S(\delta) = \frac{4\pi T}{eR_N} \sum_{\omega} \frac{\Delta \cos(\delta/2)}{\sqrt{\Delta^2 \cos^2(\delta/2) + \omega^2}} \arctan \frac{\Delta \sin(\delta/2)}{\sqrt{\Delta^2 \cos^2(\delta/2) + \omega^2}} \tag{2.3.1}$$

where δ is the phase difference of the wave function of the Cooper pairs in the two electrodes. As shown in Fig. 2.2, these types of junctions have a skewed current-phase relationship (CPR) compared to the sinusoidal one for tunnel junctions. Moreover, the CPR becomes more skewed at lower temperatures. This model relies on the strong assumption that the order parameter Δ changes only in the bridge. However, this is not valid for a realistic device, where the superconductivity starts to drop in a region L_{eff} inside the electrodes, worsening the skewness of the CPR. In the paper of Vijay et al. [18], 2D and 3D aluminium junctions were considered, and the Usadel equations were solved in a two-dimensional grid (the 3D model is actually a rotated 2D junction, so it was reduced due to this symmetry to the 2D case), obtaining the results in Fig. 2.3. As we can see, the CPR strongly depends on the geometry of these devices. But for a 3D variable-thickness design (when the electrodes are thicker than the bridge), the CPR starts to resemble the KO-1 limit. This is because the electrodes are effectively a "bank" or reservoir of superconductivity, and the drop of the phase shift starts to happen near the bridge compared to the 2D model, as we can see in Fig. 2.3. The work presented by the authors is the first approach to a numerical design of this type of junction. However, it lacks a more structured process since it is based on an outdated finite element analysis that makes moving to a generic 3D model harder. In a more recent work [65], 2D SNS junctions were also analyzed but the CPRs, useful for qubits and SFQs, were not calculated.

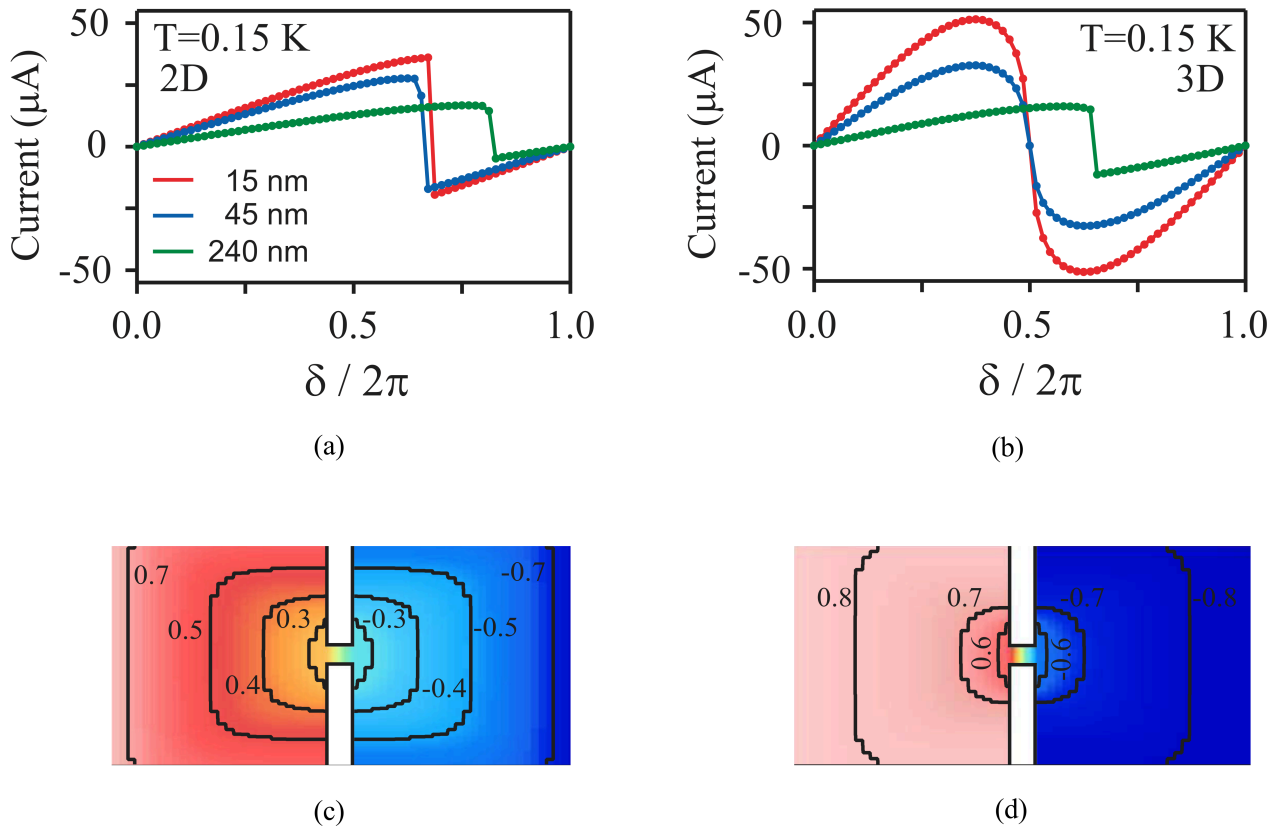

Figure 2.3: CPR of planar (a) and variable-thickness (b) nanobridge junctions for different bridge lengths; the width of the bridge is $W = 45$ nm in all cases. The junctions are considered to be made of aluminium. The phase difference of the function Φ in Eq. (2.2.10) across the nanobridge junction is shown for the planar (c) and variable-thickness (d) designs. It can be observed that in the variable-thickness design, the phase drops significantly only in a region closer to the constriction compared to the planar case. As discussed in the main text, this means that the electrodes behave as good reservoirs of superconductivity, resulting in a less skewed CPR, which will be useful in applications in quantum circuit dynamics, as discussed in the next section. Figures from [18].

2.4 Modelling realistic multilayer devices for superconducting quantum electronic circuits

As shown earlier, all the previous theoretical works were limited to 3D simulations [19] that did not include applications in quantum technologies, or to 2D designs [17, 18, 64, 65] which did not consider more elaborate shapes such as rounded edges. We aim to overcome these limitations by developing a numerical model which can interface with the standard design process of superconducting quantum devices [2].

2.4.1 The Finite Element Method

The Finite Element Method (FEM) is a numerical technique used to approximate solutions for a wide range of scientific and engineering problems involving complex geometries, physical phenomena, and boundary conditions [73]. FEM is particularly effective in areas such as structural mechanics, heat transfer, fluid dynamics, and electromagnetics. The method works by dividing a complex problem domain into smaller, simpler subdomains. In 2D, these elements are typically triangles or quadrilaterals, while in 3D they are tetrahedra or hexahedra. The behavior of the physical system within each element is approximated using mathematical functions commonly known as shape functions that represent quantities such as displacement, temperature, or pressure. FEM generally consists of four main phases [73, 74]:

- **Discretization:** The problem domain is divided into a mesh of elements. Each element contains a set of nodes, and the physical behavior within the element is approximated using interpolation functions (shape functions).
- **Formulation of Equations:** The governing differential equations describing the physical system are converted into a weak form. This weak formulation involves integrals over the domain and allows flexible handling of boundary conditions and irregular geometries.
- **Assembly:** The contributions from individual elements are combined to form the global system of equations. This involves constructing a larger matrix equation that relates the unknown quantities (e.g., displacements or temperatures) to applied forces or boundary conditions.

- **Solution:** The global system of equations is solved numerically to obtain approximate values of the unknowns. Techniques such as Gaussian elimination, iterative solvers, or sparse matrix methods can be used at this stage.

2.4.2 FEM applied to the Usadel equations

The numerical implementation is based on SfePy (Simple Finite Elements in Python), an open-source finite element package written in Python [74]. In SfePy, a problem is defined directly in its weak form, by combining predefined integral "terms" (for example diffusion, volume and surface terms) into equations, on meshes generated by external software such as gmsh. The package provides linear and non-linear solvers, including the Newton-Raphson method, and allows users to define new terms when the predefined ones are not sufficient, which was necessary in this work. As previously discussed, solving the system of partial differential equations (PDEs) of interest requires several key steps. Firstly, we need to create a 3D model of the device and mesh it, as will be elaborated in the next section. More importantly, we must express the equations in the weak form, depending on the solver employed. Given the nonlinearity of the problem and the capabilities available in SfePy, the commonly chosen solver is the Newton-Raphson method [75]. The set of equations needs to be separated into its real and imaginary parts, resulting in a dual set of equations coupled together by the absolute value of Φ, which contains both the real and imaginary parts, represented as $\|\Phi\| = \sqrt{\mathrm{Re}(\Phi_I)^2 + \mathrm{Im}(\Phi_I)^2}$. These equations are then expressed in the weak form, following the approach outlined in [17]:

For the real part:

$$\int_\Omega G_S \,\mathrm{Re}(\Phi_S(\omega_n)) \cdot s_r \, d\Omega - \int_\Omega G_S \Delta_S \cdot s_r \, d\Omega + \xi_S^2 \frac{\pi T_{CS}}{\omega_n} \int_\Omega G_S^2 \vec{\nabla}\,\mathrm{Re}(\Phi_S(\omega_n)) \vec{\nabla} \cdot s_r \, d\Omega + \xi_S \frac{\pi T_{CS}}{\omega_n} \int_{\Gamma_{S(S'/N)}} \frac{\gamma G_S G_N}{\gamma_B} (\mathrm{Re}(\Phi_S(\omega_n)) - \mathrm{Re}(\Phi_{S'/N}(\omega_n))) \cdot s_r \, d\Gamma_{S(S'/N)} = 0 \quad (2.4.1)$$

For the imaginary part:

$$\int_\Omega G_S \,\mathrm{Im}(\Phi_S(\omega_n)) \cdot s_r \, d\Omega - \int_\Omega G_S \Delta_S \cdot s_r \, d\Omega + \xi_S^2 \frac{\pi T_{CS}}{\omega_n} \int_\Omega G_S^2 \vec{\nabla}\,\mathrm{Im}(\Phi_S(\omega_n)) \vec{\nabla} \cdot s_r \, d\Omega + \xi_S \frac{\pi T_{CS}}{\omega_n} \int_{\Gamma_{S(S'/N)}} \frac{\gamma G_S G_N}{\gamma_B} (\mathrm{Im}(\Phi_S(\omega_n)) - \mathrm{Im}(\Phi_{S'/N}(\omega_n))) \cdot s_r \, d\Gamma_{S(S'/N)} = 0 \quad (2.4.2)$$

Here, $\Gamma_{S(S'/N)}$ represents the surface separating the materials S and S'/N. The equations for the second material, denoted as S'/N, are identical except for differences in the integrals over $\Gamma_{S(S'/N)}$ due to distinct boundary conditions as outlined in Eq. (2.2.12). To address the coupling effect of Δ on all the $2N$ equations, a self-consistent calculation of the order parameter Δ is required. This means treating Δ as non-dependent on Φ. In other words, an initial value Φ_0 is chosen for each ω_n, and Δ is then iteratively updated. This process continues until convergence is achieved. The Anderson acceleration algorithm [76] is employed for updating Δ. This algorithm accelerates the convergence of the iterative process and enhances the efficiency of solving the PDEs.

Algorithm 1 Anderson Acceleration for Usadel equations: $f(x) = G(x) - x$, $\Delta x_i = x_{i+1} - x_i$, $f_i = f(x_i)$, $\Delta f_i = f_{i+1} - f_i$, X_k denotes the $p \times m_k$ matrix $X_k = \left[\Delta x_{k-m_k}, \ldots, \Delta x_{k-1}\right]$, and F_k denotes the $p \times m_k$ matrix $F_k = \left[\Delta f_{k-m_k}, \ldots, \Delta f_{k-1}\right]$.

Given $x_0 \in \Omega$ and an integer $m \geq 1$. Set $c_1 = 1$, $x_1 = x_0 + f(x_0)$.

for $k = 1, 2, 3, \ldots$ until convergence **do**

$m_k = \min(m, c_k)$.

Compute $f_k = f(x_k)$.

Find the $m_k \times 1$ vector $\gamma(k)$ which solves the least-squares problem:

$\gamma(k) = \arg\min ||f_k - F_k\gamma||_2$, $\gamma \in \mathbb{R}^{m_k}$.

$x_{k+1} = x_k + f_k - (X_k + F_k)\gamma(k)$.

if $k \mod m = 0$ **then**

$c_{k+1} = 1$.

else

$c_{k+1} = c_k + 1$.

end if

end for

where in our case:

$$x = \Delta \tag{2.4.3}$$

$$G(\Delta) = \frac{\sum_{\omega_n}^{N} \frac{G_S \Phi_S(\omega_n, \Delta)}{\omega_n}}{\ln \frac{T}{T_{CS}} + 2\pi T \sum_{\omega_n}^{N} \frac{1}{\omega_n}} \tag{2.4.4}$$

As discussed above, the Usadel equations do not fall into the class of standard partial differential equations typically encountered in finite element analysis. In particular, the dependence of the

coefficients on the complex pairing function Φ through its modulus introduces non-linearities and terms that are not differentiable in the complex sense. This requires special care in the numerical implementation. To address these aspects, the equations were implemented within the SfePy Python library by defining custom non-linear terms that explicitly account for the structure of the Usadel equations. The main parts added to SfePy in this work are: (i) a non-linear diffusion term, $\int_\Omega G^2(\Phi)\,\vec{\nabla}\Phi\cdot\vec{\nabla}s\,d\Omega$, and a non-linear volume term, $\int_\Omega G(\Phi)\,\Phi\,s\,d\Omega$, in which the coefficient G depends on the solution through $|\Phi|$, together with their derivatives with respect to the real and imaginary parts of Φ, which are needed to build the Jacobian for the Newton-Raphson solver; (ii) the surface terms that couple different materials through the boundary conditions of Eqs. (2.2.12) and (2.2.13); and (iii) the outer self-consistency loop for the order parameter Δ, based on Anderson acceleration (Algorithm 1), followed by the calculation of the supercurrent from the converged solution. The code is reported in Appendix A. The two non-linear terms described in (i) have since been incorporated into the general SfePy package and are now available as part of the standard library [77, 78] (Nonlinear diffusion terms in SfePy).

2.5 Testing the Code

We explored various Josephson junction geometries in order to validate the numerical implementation across increasing levels of geometric complexity. In particular, progressively moving from effective 1D models to fully 3D structures allowed us to benchmark the code against well established theoretical results and previously published numerical studies. Three types of benchmarks are used in this thesis. The first is analytical: in the short junction limit, the model must reproduce the KO-1 CPR (Section 2.5, 1D bridge). The second is numerical: for single-material aluminium nanobridges with two- and three-dimensional banks, the model must reproduce the CPRs computed in Ref. [18] (2D and 3D tests below). The third is experimental, and is discussed in Section 2.6 and in Chapter 3.

2.5.1 1D Bridge Simulation

As an initial validation step, we designed a one-dimensional nanobridge with rigid boundary conditions imposed at both ends, ensuring that the function Φ remains fixed at the boundaries. The geometry is shown in Fig. 2.4(a). This configuration allows direct comparison with the KO-1 model

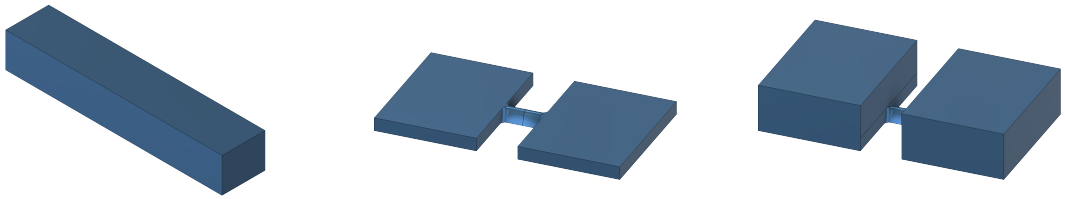

(a) (b) (c)

Figure 2.4: 3D models of the nanobridge junction considered in this work: (a) effective 1D bridge, (b) planar junction, and (c) variable thickness junction. Rigid boundary conditions are applied as described in the text.

[62], which is valid in the limit where the bridge length L is much smaller than the superconducting coherence length ξ. The resulting current phase relationships (CPRs), shown in Fig. 2.5, exhibit excellent agreement with the analytical KO-1 predictions across a range of temperatures. This agreement confirms that the numerical solver correctly reproduces the expected short junction behavior and provides a reliable baseline for more complex simulations.

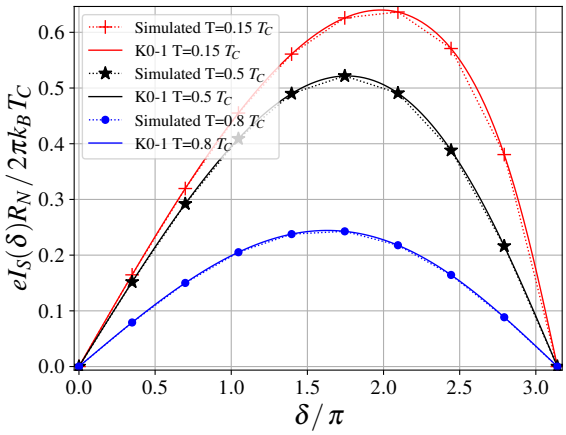

Figure 2.5: CPR (dots) obtained from simulations of a nanobridge with length $L \ll \xi$ at different temperatures, compared to the KO-1 model (solid lines).

2.5.2 2D Aluminium Junction Replication

Having established consistency in the 1D limit, we proceeded to test the code against a realistic 2-dimensional geometry by replicating the planar aluminium junction studied in Ref. [18]. The corresponding geometry is shown in Fig. 2.4(b). Following Ref. [18], the bridge has a width $W =$

45 nm and lengths $L = 15$, 45 and 240 nm, and it is connected to banks with lateral dimensions of 600 nm. The aluminium parameters are $T_C = 1.2$ K and $\xi(0) \approx 30$ nm, and the simulations are performed at $T = 0.15$ K, so that the bridge lengths range from about $0.5\,\xi$ to $8\,\xi$. The primary objective of this simulation was not to explore new physics, but rather to verify that the numerical implementation is capable of reproducing previously published results. In contrast to the KO-1 model, rigid boundary conditions were imposed at the ends of the superconducting electrodes, rather than directly at the weak link. This choice reflects a more realistic physical situation, in which the order parameter varies also in the vicinity of the junction. The resulting CPRs, shown in Fig. 2.6(a), are in good agreement with the results reported in Ref. [18], demonstrating that the code reliably captures the current transport properties of planar nanobridge junctions.

2.5.3 3D Variable Thickness Nanobridge Analysis

We further extended this validation to a fully 3-dimensional variable thickness nanobridge (VTB), using the same material parameters as in the 2D case. The geometry, shown in Fig. 2.4(c), closely follows that considered in Ref. [18], with the same bridge width and lengths as in the planar case and banks that are much thicker than the bridge. In Ref. [18] the three-dimensional banks were modelled as hemi-cylinders with a diameter of 600 nm, in order to reduce the problem to two dimensions using cylindrical symmetry; in our model the full three-dimensional geometry is solved, without symmetry assumptions, and serves as an additional benchmark for testing the robustness of the numerical approach. Figure 2.6(b) shows the CPR obtained for the VTB geometry. Compared to the planar junction, a reduced skewness is observed, a feature that is particularly relevant for applications requiring enhanced anharmonicity, as discussed in Section 1.3.2. To better understand the origin of this behavior, we also analyzed the spatial distribution of the superconducting phase across the junction. As shown in Fig. 2.6(c),(d), the phase drop in the variable thickness junction occurs closer to the bridge region than in the planar case. This localization of the phase gradient explains why the CPR increasingly resembles that of the KO-1 model, in which the phase variation is confined to the weak link itself. These observations are fully consistent with the results reported in Ref. [18], further validating the correctness of the implementation.

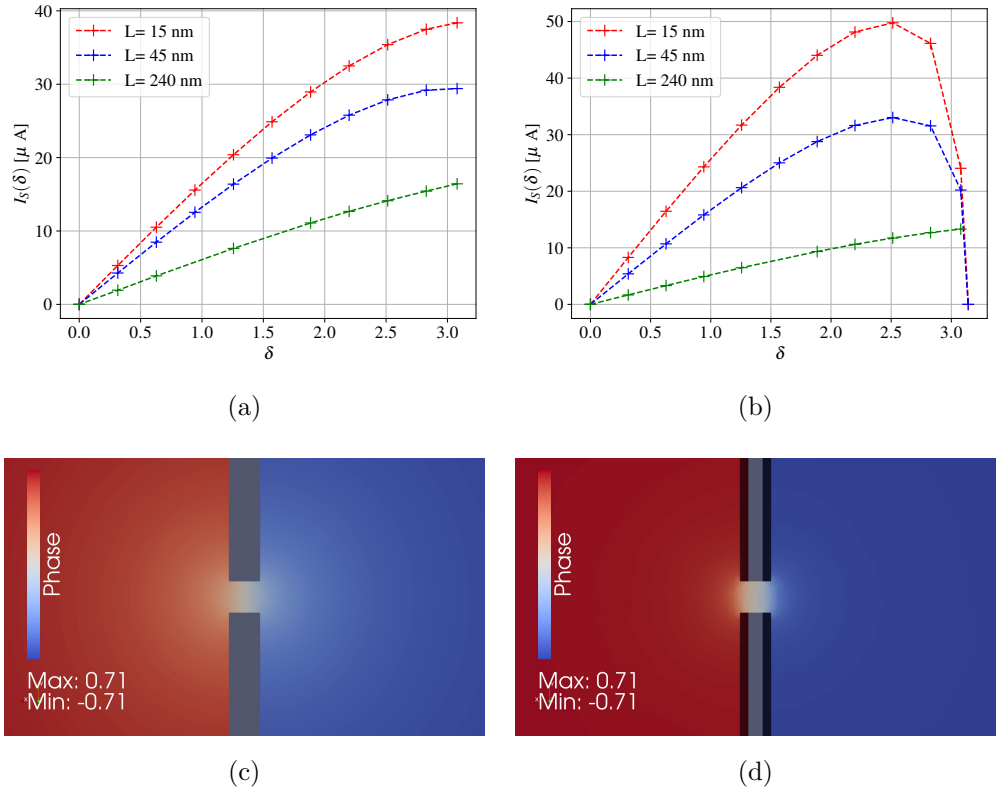

Figure 2.6: CPR calculated from the models in Fig. 2.4, replicating the junction designs of Ref. [18] in order to validate the numerical code. (a) Planar junctions. (b) Variable thickness junctions. (c) Phase variation across the planar junction. (d) Phase variation across the VTB junction.

2.5.4 Numerical Convergence

Finally, we investigated the numerical convergence of the simulations by analyzing the dependence of the critical current on the spatial discretization. Figure 2.7 shows the critical current as a function of the number of mesh elements, while keeping the number of phase steps fixed. The results demonstrate clear convergence as the mesh is refined, with variations in the critical current becoming negligible beyond a certain discretization threshold. This confirms that the chosen mesh density is sufficient to accurately capture the relevant physics and that the numerical results presented in this work are not affected by discretization artifacts.

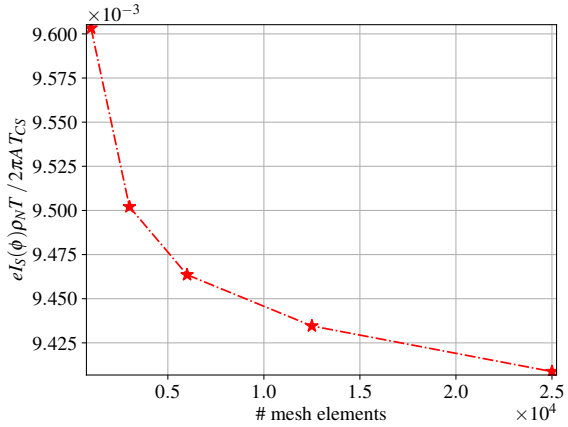

Figure 2.7: Convergence of the critical current as a function of the number of mesh elements, with the number of phase steps kept fixed. Figure from [2].

2.6 Multi-layer devices

Note: this section is mainly based on my publication [2].

2.6.1 Design

Building on the discussion in the previous section, we investigated several nanobridge layouts using numerical simulations [2]. The aim of this study is twofold: first, to benchmark the numerical model against established experimental results, and second, to use the validated model to explore junction geometries and materials that are relevant for practical devices. The geometries considered in this work are shown in Fig. 2.8 from [2]. We focused on two main classes of devices: planar

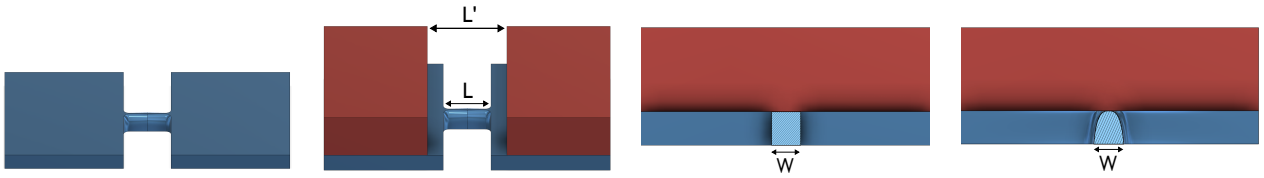

(a) (b) (c) (d)

Figure 2.8: Three-dimensional designs of the nanobridge junctions analyzed in this work. (a) Planar nanobridge junction. (b) Variable-thickness nanobridge (VTB) junction. (c) Cross-section of a simplified VTB junction with rectangular edges. (d) Cross-section of a VTB junction with realistically rounded edges. Different colors indicate the presence of different materials. Figure from [2].

nanobridge junctions and variable-thickness nanobridge (VTB) junctions of the S(S′/N)S type, each implemented with both rectangular and realistically rounded cross-sections. Rounded edges were explicitly included to account for deviations from ideal geometries introduced during the etching process, as commonly observed in experiments [2, 60]. For all simulated devices, the lateral width and length of the nanobridge were fixed to $W = 0.5\xi$ and $L = 2\xi$. The resulting current phase relations are reported in Fig. 2.9. In the case of planar junctions, the introduction of rounded edges leads to a systematic reduction of the critical current, even after normalizing for the reduced cross-sectional area [2]. In addition, a small shift of the CPR maximum toward lower phase differences is observed. This behavior can be understood as a consequence of the weakened coupling between the electrodes, which effectively brings the junction closer to the idealized one-dimensional limit described by the KO-1 model derived from the Usadel equations [2], also shown in the figure for comparison. Despite this trend, the simulated CPRs generally exhibit a reduced amplitude and an increased skewness compared to the KO-1 prediction. This deviation originates from the suppression of the superconducting energy gap more in the bridge region relative to the bulk electrodes, as illustrated in the inset of Fig. 2.9. For the same set of material and geometrical parameters, VTB junctions yield CPRs that are less skewed than those of planar junctions. As discussed earlier, this behavior is a direct consequence of the variable thickness profile: the thicker electrodes act as robust phase reservoirs, confining most of the phase variation to the narrow bridge region rather than distributing it across the banks. This mechanism enhances the effective nonlinearity of the junction and can be beneficial for qubit anharmonicity, in agreement with

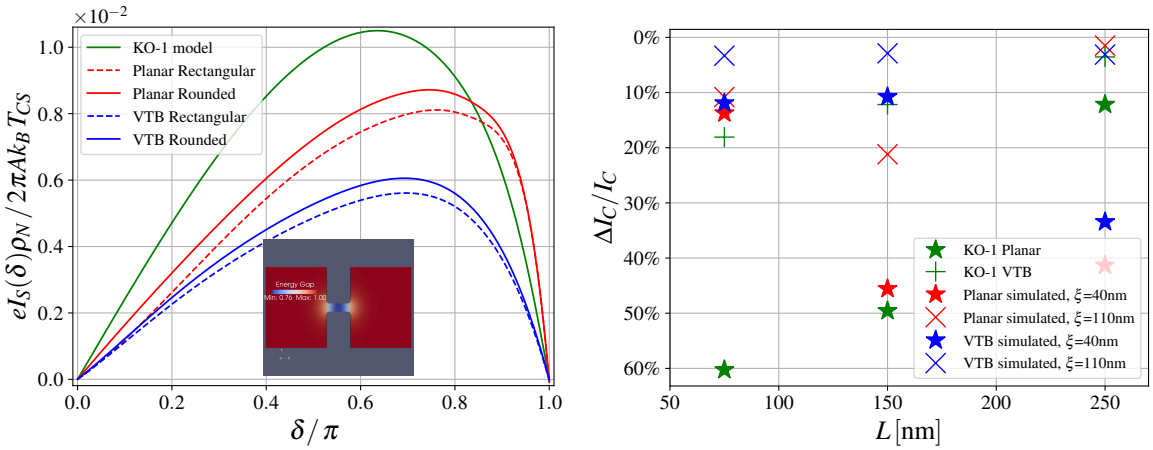

(a) (b)

Figure 2.9: (a) Simulated current phase relations (CPRs) of different nanobridge junctions. For the VTB junctions, the parameters are $L/\xi_{S'} = 2$, $L' = 2L$, $T/T_{CS'} = 0.1$, $T_{CS}/T_{CS'} = 5$, $\xi_S = 5\xi_{S'}$, $\gamma_B = 0.01$, $\gamma = 0.01$, and $T_{CS} = 5\,\mathrm{K}$. For the planar junction, a single material is considered, with parameters $L/\xi_S = 2$, $T/T_{CS} = 0.1$, and $T_{CS} = 5\,\mathrm{K}$. Here, A denotes the cross-sectional area of the nanobridge. The inset shows the normalized pair potential of the planar junction with rounded edges, simulated using the same parameters and a phase difference $\delta = 0.3\pi$, illustrating the expected suppression of the order parameter in the weak-link region. (b) Comparison between simulated and experimental critical currents from Ref. [79] as a function of nanobridge length. The percentage difference between the experimental values and those obtained from the simulations or from the KO-1 model is reported. Overall, the simulated results show good agreement with the experimental data, with improved alignment obtained by assuming a larger coherence length than the value originally reported in Ref. [79], consistent with Ref. [80]. Figure from [2].

previous experimental and theoretical studies [2, 18]. Furthermore, the use of different materials in the multilayer stack provides an additional degree of freedom for controlling the critical current I_C through the choice of the bottom-layer resistivity. Before presenting new device designs, we further validated the numerical model by comparing its predictions with experimental data. Experimental benchmarks for nanobridge models are scarce, because a quantitative comparison requires devices for which both the geometry and the material parameters (ρ, T_C and ξ) are reported. One of the few sources is that of Ref. [79], where aluminium planar and VTB nanobridges, 8 nm thick and 30 nm wide, with lengths between 75 and 400 nm, were characterized; the VTB devices had 80 nm thick banks. In the comparison below we consider the bridges with $L = 75$, 150 and

250 nm. A second experimental benchmark, for multilayer NbN and TiN based nanobridges, is provided by the devices fabricated in this thesis and is discussed in Chapter 3. The comparison is shown in Fig. 2.9(b). To reproduce the experimental CPRs, we first estimated the normal-state resistivity from the measured IV characteristics of a 75 nm long VTB junction. Simulations were then performed using both the coherence length $\xi = 40$ nm reported in the experiment and a larger value $\xi = 110$ nm taken from Ref. [80]. The latter provided a closer agreement with the experimental data, suggesting that the effective coherence length in the device may be larger than initially assumed. A possible explanation is that the coherence length inferred from resistivity measurements performed at room temperature underestimates the low-temperature value relevant for superconducting transport. The quality of this comparison should be assessed taking into account the uncertainties in the input parameters. The model reproduces the decrease of the critical current with increasing bridge length, which is the main experimental trend. Quantitatively, with $\xi = 110$ nm the simulated critical currents of the VTB devices differ from the measured ones by about 3% for all three lengths, while for the planar devices the difference is between about 2% and 21%. With the coherence length reported in the experiment, $\xi = 40$ nm, the differences increase to 11 to 33% for the VTB devices and 14 to 46% for the planar ones, and they grow with the bridge length. This is expected, since for longer bridges the critical current becomes more sensitive to the ratio L/ξ, so an error in ξ has a larger effect. The KO-1 model gives differences of 3 to 18% for the VTB devices, where the thick banks act as good phase reservoirs and the rigid boundary conditions of the model are approximately satisfied, but up to 60% for the planar devices, where the suppression of the order parameter in the banks, neglected by KO-1, is significant. The remaining discrepancy can be attributed to several factors. The resistivity was estimated from a single device and assumed to be the same for all bridges; the coherence length is not known precisely; and the actual dimensions of the bridges, in particular their 8 nm thickness, may vary by a few nanometres, which changes the cross-section by tens of percent. In addition, the measured quantity is the switching current, which can be lower than the intrinsic critical current computed by the model because of thermal fluctuations and heating. Finally, this benchmark tests only the critical current and not the full shape of the CPR, which was not measured directly. Within these limits, the comparison shows that the numerical framework captures both the qualitative trends and the order of magnitude of the experimental critical currents [2].

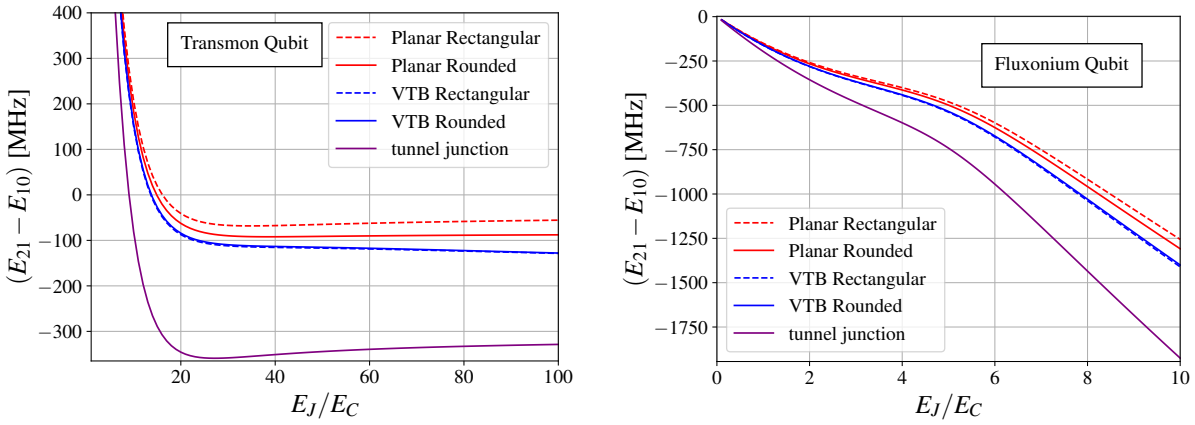

(a) (b)

Figure 2.10: Simulated anharmonicities of (a) Transmon and (b) Fluxonium qubits using the CPR from Fig. 2.9, assuming the same Josephson energy for all devices. Both qubits use $E_C = 300$ MHz, and the Fluxonium also uses $E_L = 0.53\,E_C$ [57]. For the Fluxonium, smaller E_J values were explored, as it operates in the regime $E_J < 10\,E_C$ [59]. Figure from [2].

2.6.2 Qubit energy levels

The numerical framework developed in this chapter can be directly applied to the study of superconducting qubits based on nanobridge Josephson junctions. In particular, the non sinusoidal current phase relations (CPRs) obtained from the microscopic simulations can be incorporated into effective circuit Hamiltonians to evaluate their impact on qubit energy spectra [2, 61]. For a transmon qubit, the Hamiltonian describing the phase dynamics in the presence of a generic CPR can be written as

$$\hat{H} = 4E_C(\hat{n} - n_g)^2 - E_J f(\hat{\delta}) \tag{2.6.1}$$

where E_C is the charging energy, n_g the offset charge, and $f(\hat{\delta})$ encodes the CPR of the junction. In the case of a fluxonium qubit, the Hamiltonian includes an additional inductive term arising from the superinductance [57–59]:

$$\hat{H} = 4E_C(\hat{n} - n_g)^2 - E_J f(\hat{\delta}) + \frac{E_L}{2}\hat{\delta}^2 \tag{2.6.2}$$

Fluxonium qubits operate in a parameter regime that distinguishes them from other inductively shunted circuits, requiring $E_L \ll E_J$ and $E_J < 10E_C$ [59]. These constraints impose an upper bound on the critical current of the nanobridge junction, which must remain below approximately

50 nA. Although such values are relatively small for nanobridge junctions, they can be achieved by engineering highly resistive weak-link layers, as discussed earlier in this chapter. The Josephson energy associated with a given CPR is obtained directly from the numerically computed supercurrent according to [61]

$$E_J f(\hat{\delta}) = \int I_J(\delta) \frac{\Phi_0}{2\pi} d\delta \tag{2.6.3}$$

where $I_J(\delta)$ is the phase-dependent supercurrent and Φ_0 is the superconducting flux quantum. This procedure allows the CPR to be consistently mapped onto the effective circuit Hamiltonian. To determine the qubit energy levels, we implemented custom Hamiltonians in the phase basis within the scqubits framework [81] and integrated them into Qiskit Metal [82]. The resulting eigenvalue problem was solved numerically using scipy.linalg.eigh [83], following a methodology similar to that described in Ref. [61]. Calculations were performed for several realistic values of the ratio E_J/E_C, corresponding to experimentally relevant operating regimes. From the computed spectra, we extracted the qubit anharmonicities, which are shown in Fig. 2.10. As expected, junctions characterized by non-sinusoidal CPRs exhibit reduced anharmonicity compared to conventional tunnel junctions, in agreement with previous studies [61, 84]. Notably, the multilayer SS'S junction design partially restores the anharmonicity typical of planar junctions. This improvement can be traced back to the less skewed CPR enabled by the multilayer geometry, demonstrating that nanobridge based qubits can be engineered to meet the requirements of superconducting quantum circuits [2].

2.6.3 Density of states DOS

The local density of states (DOS) can be computed starting from Eq. (2.2.10) by performing an analytical continuation of the Matsubara frequencies, $\omega_n \to iE$, while keeping the order parameter $\Delta(\vec{r}, T)$ obtained from the self-consistent solution of the Usadel equations prior to the continuation. Following Ref. [2, 17], we employ the θ-parametrization of Eq. (2.2.10), which provides a convenient representation of the quasiclassical Green's functions and leads to the following set of coupled equations:

$$\xi_I^2 \nabla \cdot \left(\sin^2 \theta_I \nabla \chi_I \right) = \frac{i}{2} \sin\theta_I (\Delta_I e^{-i\chi_I} - \Delta_I^* e^{i\chi_I}) \tag{2.6.4}$$

$$-\xi_I^2 \nabla^2 \theta_I + \xi_I^2 \sin\theta_I \cos\theta_I (\nabla\chi_I)^2 = iE \sin\theta_I + \frac{1}{2} \cos\theta_I (\Delta_I e^{-i\chi_I} + \Delta_I^* e^{i\chi_I}) \tag{2.6.5}$$

and the boundary conditions in Eqs. (2.2.12), (2.2.13) and (2.2.14) become

$$\cos\theta_S = \frac{E}{\sqrt{E^2 - \Delta_0^2}} \tag{2.6.6}$$

$$\chi_S = \pm\frac{\delta}{2} \tag{2.6.7}$$

$$\gamma_B \xi_{S'/N} \sin^2\theta_{S'/N} \nabla\chi_{S'/N} \cdot \vec{n} = \sin\theta_S \sin\theta_{S'/N} \sin(\chi_S - \chi_{S'/N}) \tag{2.6.8}$$

$$\gamma_B \xi_{S'/N} \nabla\theta_{S'/N} \cdot \vec{n} = \sin\theta_S \cos\theta_{S'/N} \cos(\chi_S - \chi_{S'/N}) - \cos\theta_S \sin\theta_{S'/N} \tag{2.6.9}$$

$$\gamma_B \xi_S \sin^2\theta_S \nabla\chi_S \cdot \vec{n} = \gamma \sin\theta_{S'/N} \sin\theta_S \sin(\chi_{S'/N} - \chi_S) \tag{2.6.10}$$

$$\gamma_B \xi_S \nabla\theta_S \cdot \vec{n} = \gamma \sin\theta_{S'/N} \cos\theta_S \cos(\chi_{S'/N} - \chi_S) - \gamma \cos\theta_{S'/N} \sin\theta_S \tag{2.6.11}$$

2.7 Further simulations

In this section, we explore different combinations of materials and model parameters in order to further extend and validate the numerical simulations.

2.7.1 SNS junction

We first consider nanobridge Josephson junctions in which the weak link consists of a normal metal layer, so that the superconducting gap vanishes inside the interlayer ($\Delta = 0$) [2]. In SNS junctions, the two superconducting banks are connected through a metallic contact; therefore, we focus on the regime of highly transparent interfaces and fix the interface transparency parameter to $\gamma_B = 0.01$ throughout this analysis. Using the variable-thickness nanobridge (VTB) geometry introduced in Fig. 2.8, we performed simulations for several values of the normalized junction length L/ξ_N and of the parameter γ. For each configuration, the current phase relation (CPR) was computed and is reported in Fig. 2.11(a) for different values of the normal-metal coherence length ξ_N. From these CPRs, the corresponding critical current I_C was extracted and analyzed as a function of γ, as shown in Fig. 2.11(b). To further characterize the SNS junction, we calculated the local density of states within the nanobridge for a representative case with $L/\xi_N = 0.5$. This analysis allows us to identify the energy range in which quasiparticle states emerge inside the weak link. The resulting density of states is shown in Fig. 2.12. The dependence of the critical current on γ and ξ_N follows the expected trends predicted by the original theoretical framework and by previously reported two-dimensional numerical models [17, 85]. In particular, increasing γ or reducing ξ_N leads to a

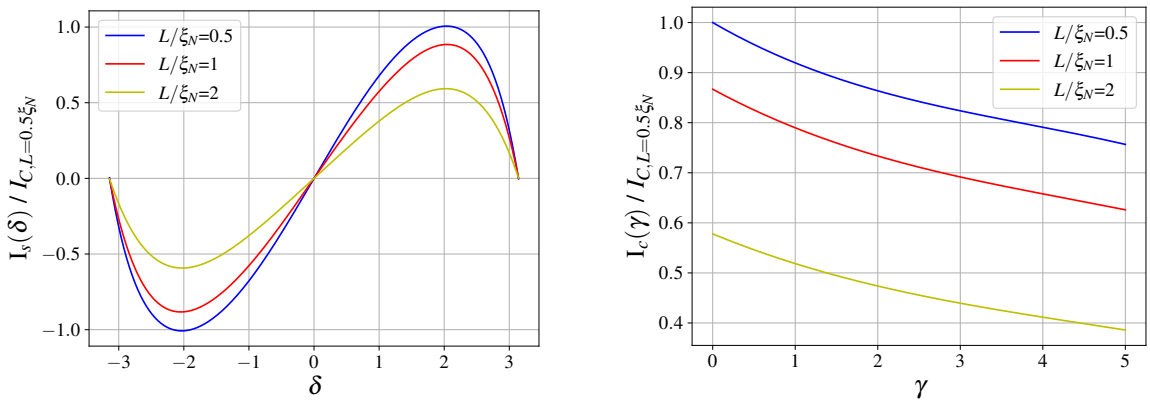

(a) (b)

Figure 2.11: (a) Simulated current phase relations (CPR) of the variable-thickness nanobridge (VTB) junction with rounded cross-section shown in Fig. 2.8, for different values of the normal metal coherence length ξ_N. The simulations were performed using $T/T_C = 0.1$, $\xi_S = 200$ nm, $L = 60$ nm, $L' = 2L$, $\gamma_B = 0.01$, and $\gamma = 0.01$. (b) Dependence of the critical current I_C on the parameter γ for different values of ξ_N. The remaining parameters were fixed to $T/T_C = 0.1$, $\xi_S = 200$ nm, $L = 60$ nm, and $\gamma_B = 0.01$. Adapted from [2].

suppression of the critical current, while the overall shape of the CPR remains largely unchanged [2], which interestingly contrasts with what is observed in SS'S junctions, where the CPR exhibits a slightly stronger dependence on the coherence length.

2.7.2 SS'S junction with $T_{CS'} > T_{CS}$

For superconducting quantum devices, junctions characterized by low critical currents and nearly sinusoidal CPRs are generally preferred [2]. These conditions are typically achieved using materials with long coherence lengths and relatively high resistivity. A straightforward approach to increase the junction resistance consists in reducing the thickness of the superconducting weak link to a few tens of nanometers. However, excessively thin films often suffer from degraded material quality, leading to a reduction in the critical temperature T_C, the electronic mean free path l, and, consequently, the coherence length [2]. To overcome these limitations, we investigate a multilayer SS'S junction design in which the bottom superconducting layer has a higher critical temperature than the top superconductor. The thickness of the lower layer is chosen to provide the desired

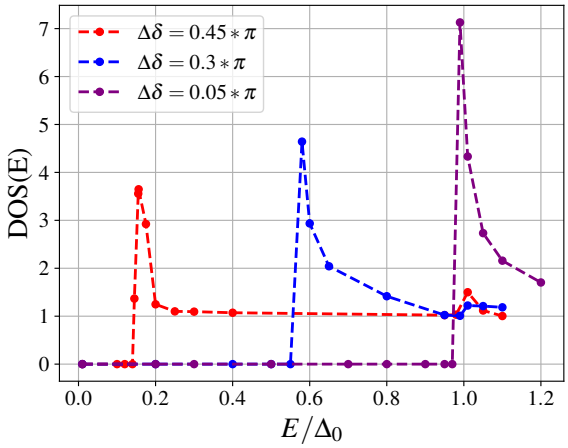

Figure 2.12: Density of states DOS(E) calculated inside the SNS nanobridge for different values of the superconducting phase difference $\Delta\delta$. The parameters used were $T/T_C = 0.1$, $\xi_S = 200$ nm, $\xi_N = 120$ nm, $W = 20$ nm, $L = 60$ nm, $L' = 2L$, $\gamma_B = 0.01$, and $\gamma = 0.01$. The results illustrate the emergence of quasiparticle states within the normal metal weak link. Figure from [2].

resistance, while the upper layer is selected to have a lower T_C [2]. This configuration is motivated by the renormalization of the Usadel equation, which leads to an effective coherence length scaling as $\sqrt{T_{CS'}/T_{CS}}$. Using the VTB SS'S geometry with rounded edges shown in Fig. 2.8, we performed simulations for different values of the ratio $L/\xi_{S'}$ and the interface parameter γ. We also investigated the dependence on L', since having a superconducting bottom layer makes it particularly relevant to assess whether pushing the top superconducting layer farther away from the weak link affects the junction properties through proximity effect. The resulting CPRs are reported in Fig. 2.13. As the coherence length of the superconducting layer $\xi_{S'}$ increases, the critical current decreases and the CPR becomes more skewed. This behavior originates from the fact that a larger $\xi_{S'}$ allows the suppression of the superconducting order parameter induced by the top layer to penetrate deeper into the bottom superconducting electrode, effectively weakening the junction. This trend differs from the SNS case. In SNS junctions, variations in the coherence length of the normal metal ξ_N have a much weaker impact on the skewness of the CPR, since the normal metal already constitutes an intrinsically weak link. However, the magnitude of the critical current in SNS junctions follows the opposite trend, increasing with ξ_N, as a longer coherence length enhances the propagation of superconducting correlations through the normal region. The dependence on the proximity parameter γ is also different from both the SNS case and SS'S junctions with a higher T_c superconductor. In the SS'S geometry considered here, increasing γ leads

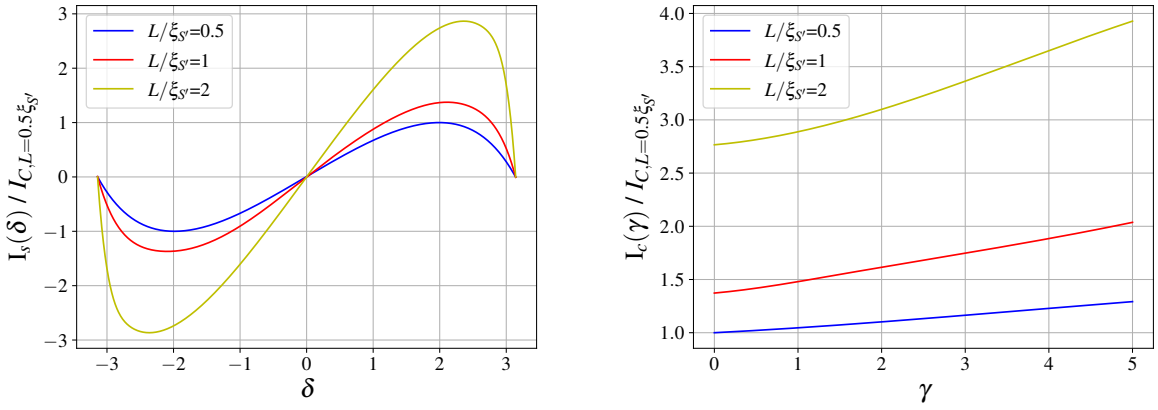

(a) (b)

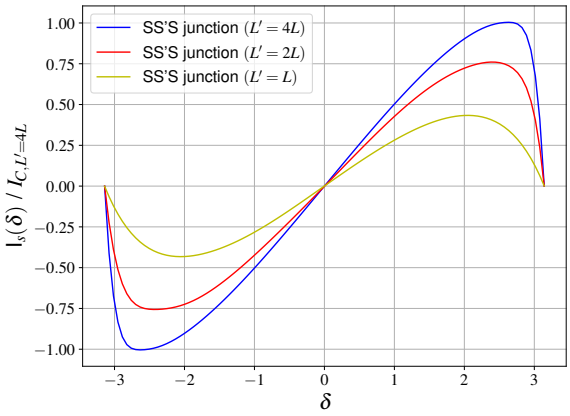

(c)

Figure 2.13: (a) Simulated current phase relations (CPR) of the SS'S variable-thickness nanobridge (VTB) junction with rounded cross-section shown in Fig. 2.8 for different values of $\xi_{S'}$. The parameters used were $T/T_{CS} = 0.1$, $T_{CS} = 1$, $T_{CS'} = 5$, $\xi_S = 200$ nm, $W = 20$ nm, $L = 60$ nm, $L' = 2L$, $\gamma_B = 0.01$, and $\gamma = 0.01$. (b) Dependence of the critical current I_C on the parameter γ for different values of $\xi_{S'}$. The remaining parameters were fixed to $T/T_C = 0.1$, $\xi_S = 200$ nm, $L = 60$ nm. (c) CPR for different distances between the banks, $\xi_{S'} = 30$ nm, $L = 60$ nm.

to an increase in the critical current. This behavior can be understood by noting that the bottom layer is the stronger superconductor, while the top layer induces a suppression of superconducting order parameter through the proximity effect. The parameter γ quantifies the relative strength of this coupling: increasing γ effectively weakens the suppression induced by the top layer. As a result, the superconducting order parameter in the bottom layer is less reduced, allowing it to sustain a larger supercurrent. As the distance between the superconducting banks increases, the

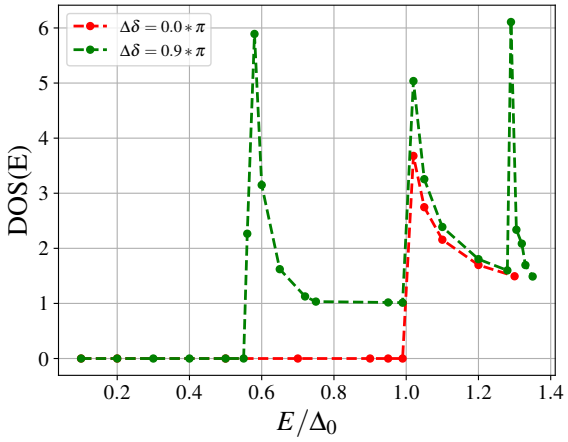

Figure 2.14: Density of states DOS(E) calculated for an SS'S nanobridge junction with $L/\xi_{S'} = 2$. The parameters used were $T/T_{CS} = 0.1$, $T_{CS} = 1$, $T_{CS'} = 5$, $\xi_S = 200$ nm, $\xi_{S'} = 30$ nm, $W = 20$ nm, $L = 60$ nm, $\gamma_B = 0.01$, and $\gamma = 0.01$. In addition to the standard quasiparticle peaks, extra features appear at higher energies due to the larger superconducting gap of the bottom layer. Figure from [2].

CPR progressively deviates from a sinusoidal form and approaches the behavior typical of planar junctions. This trend is expected, since the S' layer has a shorter coherence length and recovers its bulk superconducting properties over distances of only a few coherence lengths, thereby reducing the influence of the variable-thickness geometry [2]. Finally, we computed the density of states for a representative SS'S junction configuration to gain insight into the energy scales associated with quasiparticle generation. As shown in Fig. 2.14, the presence of two superconducting layers gives rise to additional features in the density of states at higher energies. These features originate from the bottom superconducting layer, which has a larger superconducting gap and therefore requires higher excitation energies for quasiparticle formation.

2.8 Conclusions

In this chapter, we analyzed nanobridge Josephson junctions with increasing geometric complexity, from simple one-dimensional bridges to fully three-dimensional variable thickness structures. We began by presenting the theoretical framework for these junctions, covering Green's functions and the approximations that lead to the Usadel equations. Building on this, we developed a numerical model using the finite element method (FEM) and implemented custom functions in SfePy to

solve the resulting equations. The numerical model was then validated in two stages. First, in the short junction limit, it reproduces the KO-1 model, and for two and three-dimensional geometries, it closely matches results reported in the literature, confirming the robustness of the implementation. Second, we tested the model against experimental data, demonstrating that the simulations accurately capture key features observed in real nanobridge junctions. Finally, the calculated CPRs were incorporated into standard software for superconducting quantum circuits, enabling the study of the effect of non-sinusoidal CPRs on qubit spectra. The results show that even with non-ideal CPRs, nanobridge junctions can support anharmonic qubit levels, illustrating their flexibility and suitability for quantum device applications. Overall, the numerical framework developed here represents a significant improvement over previous methods. It is not limited to two-dimensional geometries and can be extended to fully three-dimensional junction designs, making it a versatile and scalable tool for exploring novel junction geometries and integrating them into next generation superconducting circuits.

3. Nanofabrication and DC nanobridge devices

This chapter describes the nanofabrication procedures used to realize the devices investigated in this thesis. The fabrication workflow is based on standard micro and nanofabrication techniques and was optimized to achieve reliable and reproducible device production. The process includes substrate preparation, thin film deposition, lithographic patterning, dry etching, and SEM characterization. All fabrication steps were carried out in the JWNC cleanroom. A general overview of the main stages of the fabrication flow is given in the next sections, following [25, 26].

The aim of this chapter is to realise the multilayer nanobridge junctions designed with the numerical model of Chapter 2 and to verify experimentally their behaviour, both as single junctions and as elements of dc SQUIDs. The chapter is organised as follows. We first describe the general fabrication techniques used in this work: substrate preparation, sputter deposition of thin films, electron beam lithography, dry etching and structural characterisation. We then present the fabrication process developed for the gap engineered multilayer nanobridges, based on two lithography and etching steps, together with the characterisation of the superconducting films and the reproducibility of the process. The second part of the chapter is devoted to the cryogenic DC characterisation of the devices. The critical currents of NbN and TiN based nanobridges are compared with the predictions of the KO-1 model and of the three-dimensional Usadel model, and the role of heating in the measured current voltage characteristics is discussed. Finally, dc SQUIDs based on two nanobridges are characterised, and their interference patterns are analysed with a dc SQUID model that includes the current phase relation obtained from our simulations, the loop inductance and the asymmetry between the junctions.

3.0.1 Properties of silicon wafers and substrate preparation

Silicon wafers are among the most widely used substrates in nanofabrication due to their exceptional material quality, well established processing protocols, and compatibility with a broad range of deposition and patterning techniques [86]. Despite these advantages, the silicon surface forms a native oxide layer when exposed to ambient conditions. This native oxide can introduce unwanted dielectric loss and two level systems (TLS) which are particularly detrimental in superconducting quantum circuits [15, 16]. As a result, careful substrate preparation is a critical prerequisite for

nanofabrication of superconductors.

3.0.2 Substrate cleaning and surface preparation

Prior to device fabrication, wafers must undergo rigorous cleaning to remove organic contaminants, particulates, and residues introduced during handling and storage. A common preliminary cleaning procedure involves sequential rinsing in organic solvents such as acetone and isopropyl alcohol to dissolve organic residues, followed by drying with nitrogen gas. More advanced cleaning protocols may include wet chemical treatments such as piranha etching, which are designed to remove specific classes of contaminants. For applications involving superconducting circuits and resonant structures, particular attention is paid to the removal of silicon oxide. This is often achieved through a brief immersion in a hydrofluoric acid (HF) solution. To further ensure a clean interface, surface treatments such as argon ion milling can be performed immediately prior to metal deposition, even though recent studies [87, 88] have shown that this can damage the substrate surface, increasing the density of TLSs in superconducting circuits. For this reason, this process was not used for our devices.

3.0.3 Thin film deposition techniques

The deposition of thin metallic films is the second step for the nanofabrication of superconducting devices. Among the various physical deposition methods, magnetron sputtering is widely used due to its versatility, scalability, and ability to produce uniform films with well controlled thickness and composition [26, 60, 89, 90]. In sputtering, a target material is bombarded by energetic ions generated in a plasma, causing atoms to be ejected from the target surface. These atoms travel through the vacuum chamber and condense onto the substrate, forming a thin film. The process can be performed in direct current (DC) or radio frequency (RF) configurations, depending on the electrical properties of the target material, see Fig. 3.1 for a simple schematic and a picture of the tool main chamber. Deposition parameters include the base pressure of the chamber, sputtering power, gas pressure, substrate temperature. These parameters strongly influence film structure, stress, surface roughness, and electrical properties. In superconducting films, they also affect the critical temperature, penetration depth, and coherence length, making precise control essential. Multilayer structures can be fabricated by sequential deposition of different materials without breaking vacuum, preserving clean interfaces and reducing contamination. The sputtering system

used in this work hosts several targets in the same chamber (Fig. 3.1(b)), which in principle introduces a risk of cross-contamination between the targets and of the chamber walls. To limit this, each target is equipped with its own shutter, so that only the target in use faces the substrate, and every deposition was preceded by a pre-sputtering step with the shutter closed, in order to remove from the target surface any material redeposited during previous runs. It should also be noted that the aim of this thesis was not a detailed materials study, nor the search for an optimal superconductor. The main requirement on the films was that they were superconducting with reproducible critical temperature and resistivity (Section 3.1.3), since the goal was to show that many different material combinations can be used to realise nanobridges with the desired specifications.

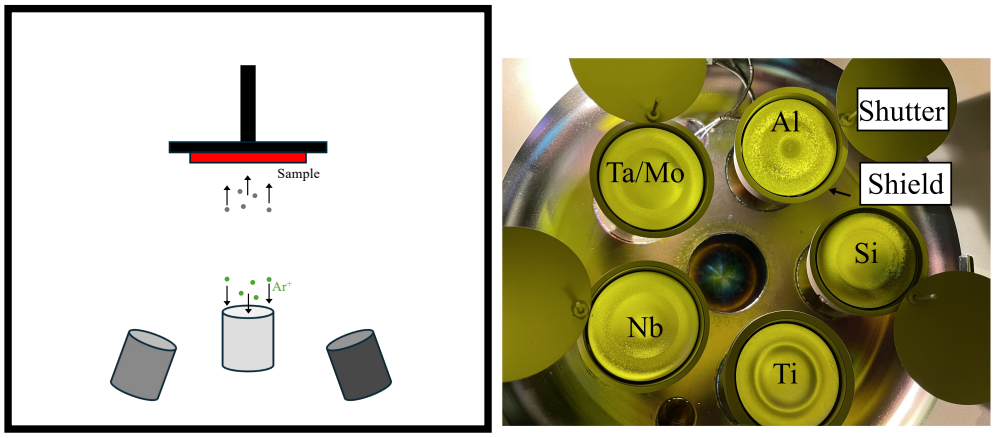

(a) (b)

Figure 3.1: a) Simple schematic overview of the sputtering process, b) Picture of the main chamber of the sputtering tool used in this work, where all the different targets are shown. Adapted from [26].

3.0.4 Resist materials and spin coating

Lithographic patterning requires the use of sensitive polymer films known as resists. These materials undergo chemical changes upon exposure to electrons or photons, enabling selective removal of specific regions during development. Resist application is typically performed by spin coating, a process in which a small volume of liquid resist is dispensed onto the sample and spread uniformly by rapid rotation. The final film thickness is determined by the resist viscosity, spin speed, and acceleration profile. Achieving a uniform resist layer is essential for accurate pattern development.

After coating, the resist is baked on a hot plate to evaporate residual solvents and improve adhesion to the substrate. The baking temperature and duration must be carefully chosen, as insufficient baking can lead to pattern collapse or poor development, while excessive baking can reduce resist sensitivity. Two main types of resist, as shown in Fig. 3.2, exist [25, 26]:

- **Negative resist:** the exposed regions become insoluble in the developer. As a result, the unexposed areas are removed during development.
- **Positive resist:** the exposed regions are removed during development, while the unexposed areas remain intact. In this work, we employed the positive tone electron beam resist CSAR [91], chosen for its high sensitivity, excellent resolution and resistance to the most common dry etching recipes.

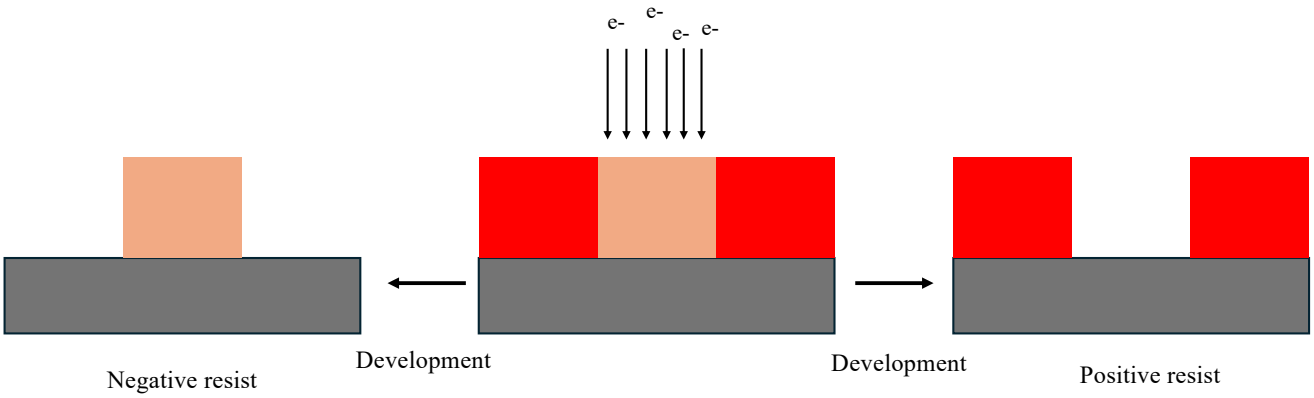

Figure 3.2: Schematic example of positive and negative tone resist. Adapted from [25].

3.0.5 Lithographic pattern definition

Lithography is the process by which patterns are transferred from a design file to the resist coated substrate. The two most commonly used techniques in nanofabrication are optical lithography and electron beam lithography. Optical lithography employs ultraviolet light to expose large areas of resist simultaneously, making it well suited for fabrication of micron scale features. Electron beam lithography, by contrast, uses a focused electron beam to write patterns directly into the resist, enabling feature sizes that can go below 20 nm at the expense of longer exposure times [92], see Fig. 3.3 for a schematic overview. During exposure, the resist undergoes a chemical

modification that alters its solubility in a developer solution. The required exposure dose depends on the resist type, thickness, and beam parameters. In electron beam lithography, additional considerations such as proximity effects, beam scattering, and charging must be accounted for to ensure pattern fidelity [25, 26]. Following exposure, the resist is developed by immersing the sample in a suitable developer solution. This step selectively removes either the exposed or unexposed regions of the resist, depending on whether a positive or negative resist is used. Development conditions, including time, temperature, and agitation, play a critical role in determining feature resolution and sidewall profile [93]. Precise control is required to avoid incomplete development or excessive erosion of fine features. After development, the sample is rinsed and dried to prevent residue formation. The resulting resist pattern serves as a mask for subsequent fabrication steps such as metal lift-off or etching.

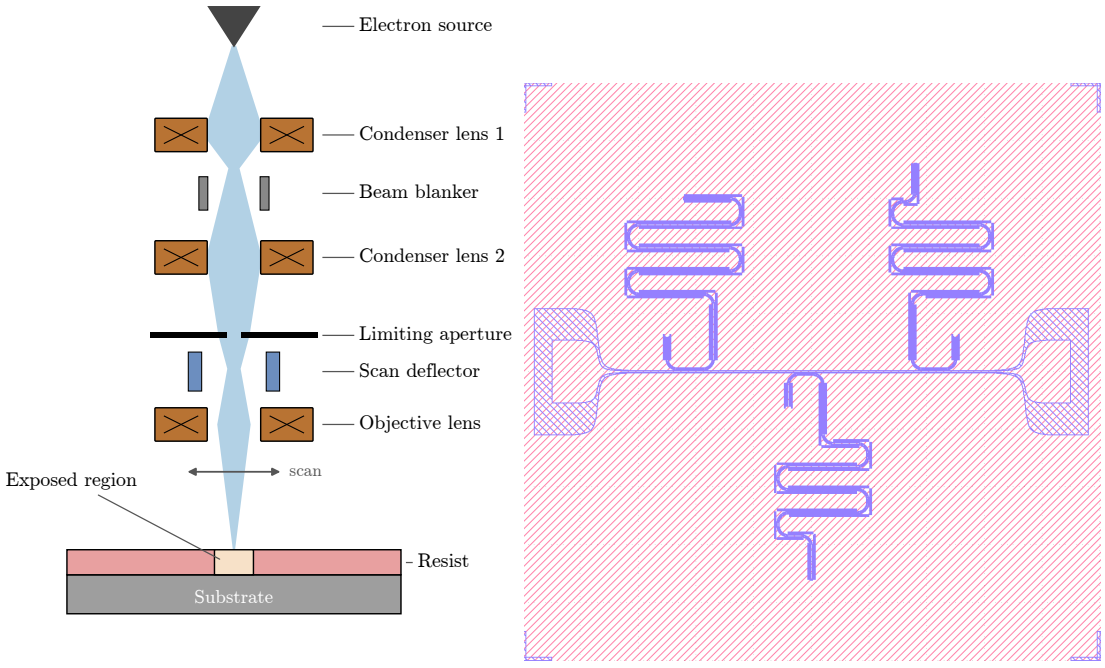

Figure 3.3: (a) Schematic overview of an electron beam lithography system, adapted from [94]. Electrons emitted from the source are focused by lenses into a finely controlled beam, which is scanned across the substrate to locally expose the resist according to the desired pattern. (b) Example of a lithographic pattern written on the substrate.

3.0.6 Dry etching techniques

The selective removal of material from the surface of a sample to define nanoscale features is a fundamental step in the fabrication of multilayer nanobridge Josephson junctions and superconducting resonators. Etching processes are generally classified into wet and dry techniques; however, the fabrication workflows adopted in this work rely exclusively on dry etching. In dry etching reactive species are generated and directed toward the surface of the sample, leading to material removal through physical sputtering, chemical reactions, or a combination of both [95]. Since the resist is also exposed to the plasma, its thickness and etch resistance must be sufficient to withstand the full duration of the process, particularly when etching multilayer stacks. Dry etching is preferred over wet etching for the fabrication of nanobridge junctions and resonators because it provides enhanced control over key parameters such as etch rate, anisotropy, and uniformity across the sample. These aspects are critical when defining narrow superconducting bridges with lateral dimensions on the order of tens of nanometers, where small deviations can significantly impact the critical current, inductance, and overall device performance. The etching processes described in this work were performed using an Inductively Coupled Plasma (ICP) system. In this configuration, an RF driven coil surrounding the chamber generates a high density plasma by inducing strong electromagnetic fields, see Fig. 3.4. The coil is powered independently from the RF source biasing the substrate electrode, allowing separate control over plasma density and ion energy. This flexibility is particularly advantageous for superconducting device fabrication, where high plasma density is required to ensure uniform etching, while excessive ion bombardment must be avoided to limit damage, redeposition, or modification of superconducting properties at the etched surfaces. Depending on the gas chemistry employed, the etch process can be predominantly reactive, physical, or mixed. Reactive etching generally offers higher etch rates and better material selectivity but tends to be more isotropic, whereas physical sputtering provides improved directionality at the expense of increased surface damage. The addition of inert gases such as Ar is commonly used to stabilize the plasma and improve uniformity, although this introduces a trade off by increasing the physical component of the etch, potentially leading to defect formation in sensitive superconducting films. Several aspects must be carefully optimized when developing an etch recipe for multilayer superconducting devices. These include the etch rate and its reproducibility, which are particularly critical when removing only a few nanometers of material, and the selectivity between different layers in the stack. Additional attention must be paid when etching features with varying aspect

ratios, as narrow nanobridges tend to etch more slowly than larger structures due to reduced flux of reactive species reaching the bottom of the features.

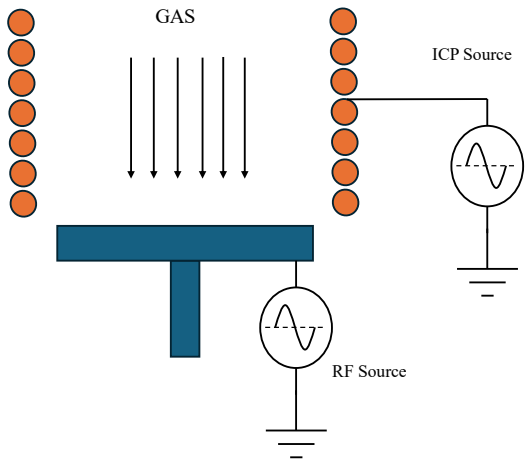

Figure 3.4: Schematic overview of an inductively coupled plasma (ICP) dry etching system. An RF-driven coil surrounding the chamber inductively couples energy into the system, while an independently powered RF bias is applied to the substrate electrode, enabling separate control of plasma density and ion energy.

3.0.7 Structural characterization and inspection

Throughout the fabrication process, structural characterization is essential for verifying dimensional accuracy and overall device quality. Scanning electron microscopy (SEM) is one of the most widely used tools for this purpose. SEM operates by scanning a focused beam of high energy electrons across the sample surface and detecting secondary or backscattered electrons emitted from the material, producing high resolution images with nanometer scale detail. This makes SEM particularly suitable for the analysis of micro and nanostructures [96]. By selecting different detection modes, it is possible to enhance either topographical contrast or compositional contrast, providing further insight into material inhomogeneities and layer structures. SEM can also be combined with energy dispersive X ray spectroscopy to obtain elemental information, which is useful for verifying material composition and detecting contamination. It provides high resolution images of surface morphology and feature geometry, enabling detailed inspection of linewidths, edge roughness, and alignment accuracy, as shown in Fig. 3.5. It also allows identification of fabrication defects such as resist residues, contamination, and incomplete etching. In advanced fabrication processes, SEM is

routinely used at multiple stages to monitor critical dimensions and ensure process reproducibility. Exposure to the electron beam can in principle modify the sample, for example through charging of the substrate or the deposition of a thin hydrocarbon contamination layer. For this reason, all SEM images in this work were acquired at a low accelerating voltage of 3 kV, with an emission current of 1 μA. At these energies the electrons cannot displace atoms in the metallic films, since knock-on damage requires electron energies of the order of hundreds of keV [96]. In addition, SEM was used mainly at the beginning of this work, on test devices, to verify that the fabrication process worked as intended; once the process was established, the devices characterised at cryogenic temperatures were not imaged by SEM before the measurements, so that any possible effect of the electron beam on the measured junctions can be excluded. Complementary techniques such as atomic force microscopy (AFM) and profilometry may be used to assess surface roughness and film thickness with high vertical resolution. AFM, in particular, enables nanoscale topographical mapping and can provide quantitative roughness measurements, while profilometry is well suited for rapid thickness evaluation over larger areas. Together, these characterization methods play an important role in process optimization, failure analysis, and overall quality control. In this work, AFM imaging of the nanobridges was attempted on a test sample, but it did not produce reliable images: the lateral dimensions of the bridges, of a few tens of nanometres, are comparable to the radius of the AFM tip, so that the measured profile is dominated by the convolution with the tip shape, particularly inside the narrow etched trenches of the variable thickness geometry. For this reason, the dimensions of the nanobridges were characterised by SEM only.

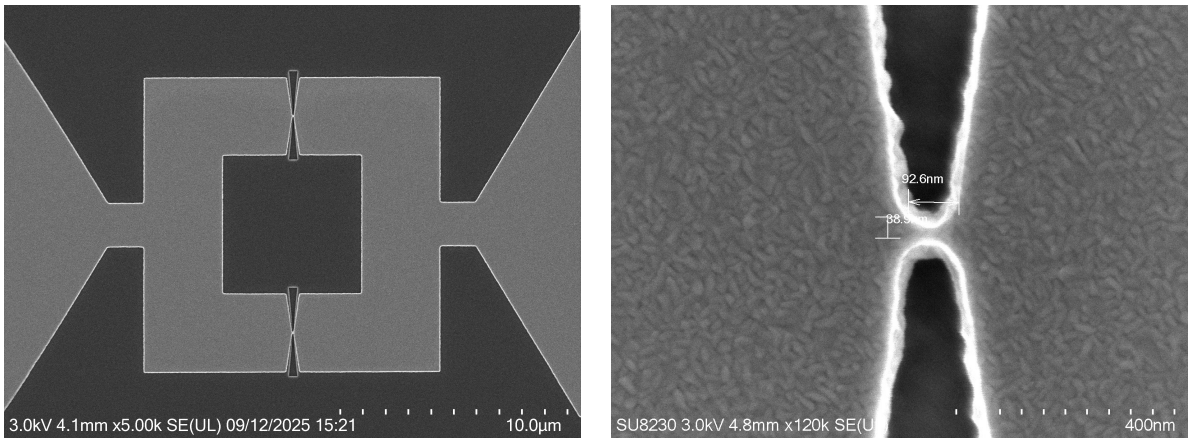

(a) (b)

Figure 3.5: Examples of SEM images taken for two samples: (a) a SQUID, where SEM was used to check that no residues or other contaminants were present near the structure, and to verify the alignment of features after multiple exposures; (b) a planar nanobridge, showing the typical size of the fabricated devices.

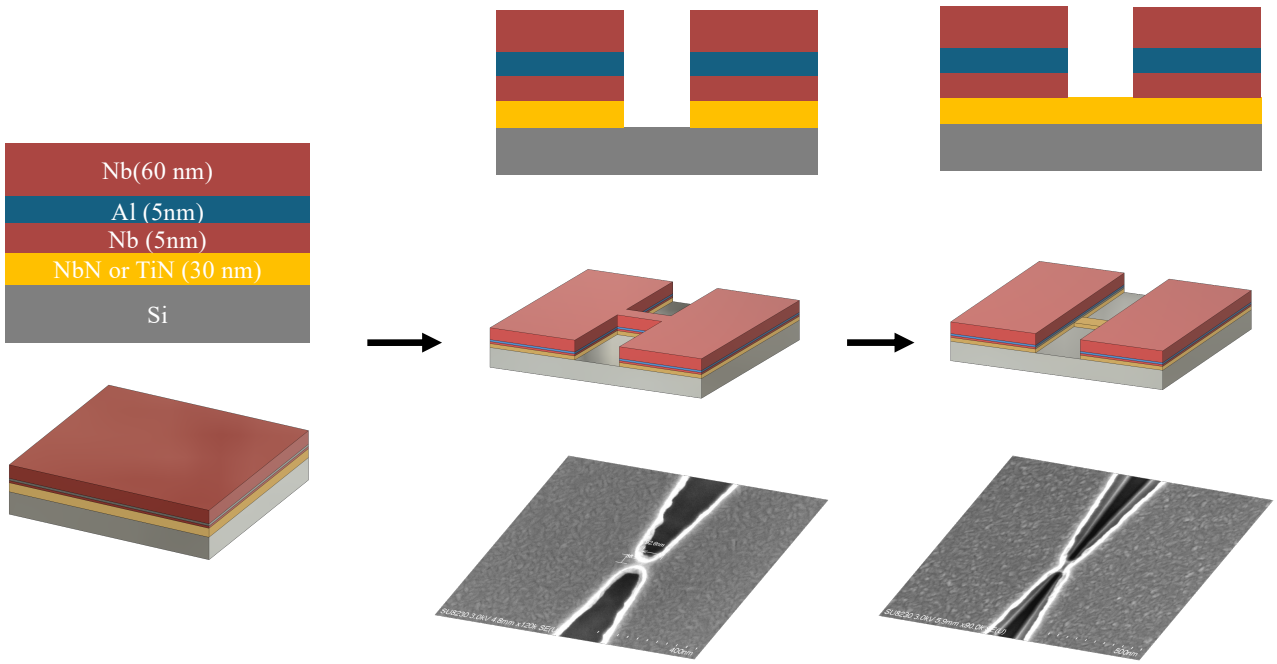

Figure 3.6: Schematic illustration of the two step fabrication process used to realize multilayer 3D nanobridges. Large features and the planar bridge are first defined, followed by a second etching step that selectively removes only the top Nb layer above the bridge. This leaves the bottom nitride layer intact, forming a high resistance three-dimensional weak link. Figure from [1].

3.1 Gap Engineered Superconducting Multilayer Nanobridges

Note to the reader: The following sections are based on my (under review) manuscript Ref. [1].

3.1.1 Fabrication of the Nanobridges

We describe here the fabrication procedure used to realize the devices investigated in this work, following the design guidelines derived from the simulations discussed in Chapter 2. These simulations were used to choose the material stack and geometrical parameters, ensuring consistency between the modeled and fabricated structures [1]. Devices were fabricated on 525 μm thick silicon substrates. The wafers were cleaned in an ultrasonic acetone bath for 5 minutes, followed by 5 minutes in isopropanol (IPA), and dried with nitrogen. The native oxide was removed by immersion in a 1:10 HF solution for 2 minutes prior to loading into the sputtering chamber. Two

multilayer stacks were investigated:

- **Sample A:** Si / NbN (50 nm) / Nb (5 nm) / Al (5 nm) / Nb (60 nm)
- **Sample B:** Si / TiN (35 nm) / Nb (5 nm) / Al (5 nm) / Nb (60 nm)

All films were deposited at room temperature by dc magnetron sputtering with a base pressure below 10^{-8} Torr [97–100]. The process starts with the deposition of the nitride layer, followed by thin Nb and Al interlayers, and finally the top Nb film. The deposition parameters (Table 3.1) were optimized based on prior work using the same system [60, 89, 90, 101]. The multilayer design ensures clean interfaces without intermediate oxidation. The Al layer acts as an etch stop, enabling controlled removal of the top Nb during fabrication. A thin Nb spacer is deposited between the nitride and the Al layer to avoid direct contact between them. If Al were deposited directly on the nitride surface, it could react with nitrogen and form a thin AlN layer at the interface. AlN is an insulator, and it is in fact used as tunnel barrier in Nb and NbN based Josephson junctions [102]; in our stack, such a layer would act as an unwanted barrier and reduce the transparency of the interface. The Nb spacer therefore preserves a good metallic coupling between the layers, while the nitride layer still defines the effective weak link [1].

Material	Gas [sccm]	Pressure [mTorr]	I [A]	V [V]	P [W]
Nb	Ar: 45	3.72	0.9	260	230
NbN	Ar: 30, N_2: 2.6	3.67	0.85	268	227
TiN	Ar: 30, N_2: 3.5	4.08	0.85	304	259
Al	Ar: 25	2.91	0.4	350	140

Table 3.1: Sputtering parameters for the deposited materials, optimized based on literature and previous work using the same deposition system. Table from [1].

3.1.2 Etching of Nanobridges and Micrometer Features

The multilayer structures were patterned using a two-step chlorine based ICP-RIE dry etching process, optimized to achieve high selectivity between Nb, NbN/TiN, and the silicon substrate. All etching steps were carried out using a $BCl_3/Cl_2/Ar$ gas mixture, which ensures smooth sidewalls and suppresses redeposition effects [1, 103]:

- BCl_3/Cl_2/Ar flow: 30/30/10 sccm
- ICP power: 300 W
- Bias (HF) power: 50 W
- Chuck temperature: 20°C
- Etch rate: ∼100 nm/min (Nb/NbN) and ∼50 nm/min (TiN)

In the first lithographic step, the full multilayer stack is etched to define the nanobridge geometry and the surrounding leads. After this complete etch, a second lithography step (including resist coating, exposure, and dry etching) is performed to selectively remove only the top Nb/Al/Nb layers in the junction region. This exposes the underlying nitride layer, which defines the effective weak link, as schematically illustrated in Fig. 3.6 [1]. This fabrication route enables the realization of an intrinsic three-dimensional nanobridge geometry with improved scalability compared to focused ion beam (FIB) milling approaches [48, 49, 104–110]. FIB milling has been very successful for the fabrication of nanobridge junctions and nanoSQUIDs, since it allows direct patterning of features down to a few tens of nanometres, including three-dimensional geometries, without resist or lift-off steps. Niobium nanoSQUIDs patterned by Ga FIB have shown very low flux noise [48, 49] and have been used, for example, to detect the magnetisation reversal of a single magnetic nanoparticle [50], while Ne FIB has recently been used to realise SQUID-embedded tunable resonators [107, 111], operating down to millikelvin temperatures [107]. The technique has, however, some limitations. The implantation of ions and the associated lattice damage suppress superconductivity in a surface layer of the milled film, which for Ga ions in Nb can extend to several tens of nanometres and becomes comparable to the size of the nanobridge itself [48, 51, 104]. Lighter or noble-gas ions such as Ne and Xe reduce this problem [106, 107], but damage and amorphisation of the substrate and of oxide layers remain a concern [108–110]. Moreover, FIB is a serial technique, in which each device is milled individually: it is ideal for a small number of devices with short lead times [105], but it is difficult to scale to circuits containing many junctions. The process developed in this work, based only on electron beam lithography and dry etching, avoids ion implantation in the weak link and can be applied in parallel to all the devices on a chip.

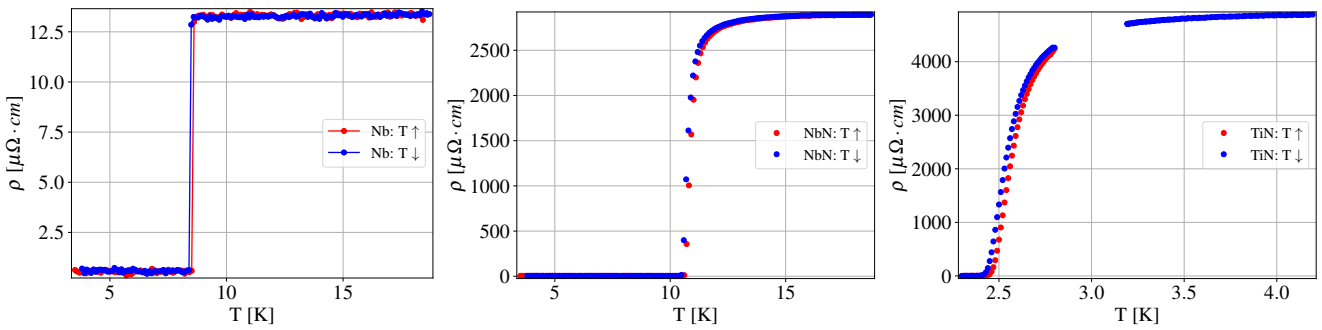

(a) (b) (c)

Figure 3.7: Critical temperature T_C and resistivity characterization of the materials used for nanobridge fabrication: (a) Nb, (b) NbN, and (c) TiN. The absence of data points around 3 K for TiN is due to measurements performed in a different cryostat, which did not allow fine temperature control in this range. Figure from [1].

Material	T_C [K]	t [nm]	ρ [$\mu\Omega$·cm]	RRR	E_F [eV]	ξ [nm]
Nb	8.45	60	13	2.79	5.3[112]	29
NbN	10.55	80	2890	0.75	1.7[113]	2.2
TiN	2.35	60	4810	0.94	2.9[114]	3.5

Table 3.2: Superconducting film properties. Table from [1].

3.1.3 Film Characterization

The superconducting thin films (Nb, NbN, and TiN) used for nanobridge fabrication were deposited and independently characterized via four point resistivity measurements in order to determine their critical temperature T_C and normal state resistivity (see Fig. 3.7) [1]. Measurements were performed using a standard four probe configuration on patterned 10 square wire structures, a geometry chosen to improve the accuracy of resistivity extraction by minimizing the impact of contact resistance. The resistance was recorded as a function of temperature during controlled cooling and warming cycles, enabling precise identification of the superconducting transition. The critical temperature T_C was defined as the midpoint of the resistive transition, while the normal state resistivity was extracted from the linear region above T_C. The resulting material parameters

are reported in Table 3.2. The measured residual resistivity ratios are consistent with values typically reported for sputtered thin films [34, 115, 116]. Using the extracted resistivity and critical temperature, the dirty limit coherence length was estimated as [9, 117]:

$$\xi = \sqrt{\frac{\hbar}{\rho \cdot 1.76 k_B T_C e^2 N_F(E_F)}} \tag{3.1.1}$$

where $N_F(E_F)$ is the density of states at the Fermi level. Literature values were used to approximate the Fermi energy and corresponding density of states for each material. For the nitride films, this procedure yields relatively short coherence lengths. However, due to the sensitivity of ξ to uncertainties in $N_F(E_F)$ and to the level of disorder in the films, the actual values are expected to differ from this simplified estimate. For this reason, in the numerical modeling we adopt an effective coherence length of $\xi = 10$ nm for the nitride layers. This choice provides a physically consistent description of the experimental trends discussed in the main text. The independently measured material parameters were then used as input for the numerical simulations of the nanobridge Josephson junctions [1].

3.1.4 Reproducibility of the Nanobridge Fabrication Process

To assess the reproducibility of the nanofabrication process, the room temperature resistance of a set of nominally identical multilayer nanobridges was measured using a probe station. Each device was individually contacted and its resistance recorded under ambient conditions. The results are reported in Fig. 3.8 as a function of the junction index [1]. The measured resistance values are centered around $R \approx 198\ \Omega$, with a device to device variation of approximately 20%. This spread is attributed to fabrication induced inhomogeneities at the nanoscale. The device with a noticeably higher resistance than the others is most likely the result of a local variation in the etching process, which removed slightly more material from the weak link. Since the resistance of the bridge scales as $R = \rho L/(Wt)$, where W and t are the width and thickness of the remaining nitride layer, and the nitride films have a high resistivity (Table 3.2), a variation of only a few nanometres in t or W produces a clearly visible change in R. Nevertheless, the absence of systematic outliers and the consistency of the overall resistance scale indicate a good level of reproducibility of the fabrication process [1].

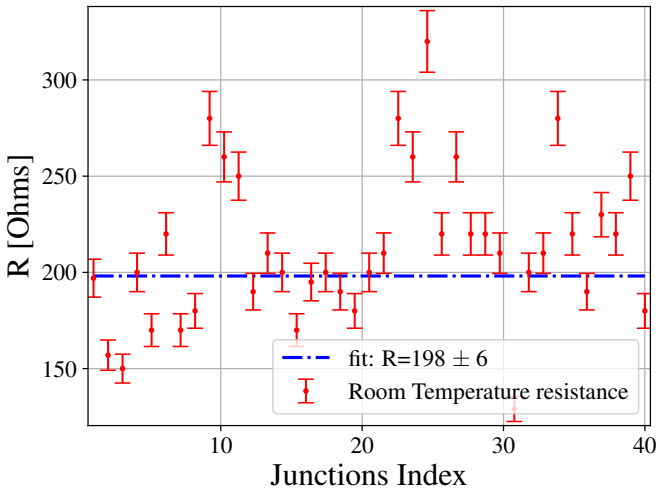

Figure 3.8: Room temperature resistance of multilayer nanobridges measured using a probe station. The resistance is shown as a function of the junction index for a set of nominally identical devices. The distribution is centered at $R = 198\ \Omega$, with a spread of $\sim 20\%$, reflecting moderate variability likely arising from nanoscale fabrication inhomogeneities. Overall, the results confirm the reproducibility of the process. Figure from [1].

3.2 Cryogenic Characterization of Nanobridge Junctions

Nanobridge junctions from samples A and B were characterized in a dilution refrigerator at a base temperature of 40 mK. Representative current voltage characteristics for NbN based devices are shown in Fig. 3.9(a) [1]. The junctions exhibit a sharp transition to a resistive state, consistent with Josephson behavior, with I_cR_N products in the range of 1 to 8 mV. These values are compatible with superconducting electronic applications such as RSFQ circuits, SQUIDs, and flux tunable resonators [5, 107, 111, 118, 119]. Some of the junctions, in particular those with the largest critical currents, such as the 29 μA device in Fig. 3.9(a), show a hysteretic IV characteristic, with a retrapping current lower than the switching current. Since the capacitance of a nanobridge is negligible ($\beta_c \ll 1$), this hysteresis cannot be explained by the RCSJ model and is of thermal origin. Once the junction switches to the resistive state, the Joule power dissipated in the weak link, $P \approx I_c^2 R_N = I_c\,(I_cR_N)$, heats the bridge above the bath temperature, and the junction returns to the superconducting state only when the current is reduced to a value at which this heat can be removed [120–122]. For junctions with similar I_cR_N products the dissipated power grows linearly with I_c, which explains why the hysteresis was observed only in the devices with the highest critical

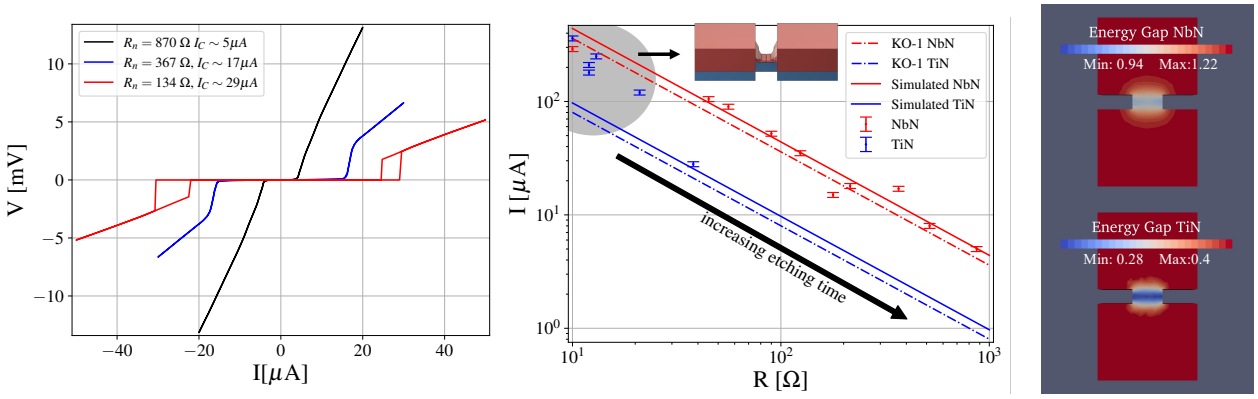

(a) (b) (c)

Figure 3.9: (a) Representative current voltage characteristics of NbN nanobridge Josephson junctions. All curves were measured at the base temperature of the dilution refrigerator, 40 mK. (b) Critical current as a function of normal state resistance. Two device populations are observed: low resistance junctions (gray region), attributed to incomplete etching and residual Nb, exhibit an I_cR_N independent of the nitride layer; properly defined junctions follow the expected trend. Solid lines correspond to simulations based on the KO-1 model and the three-dimensional Usadel model ($L = 30$ nm, $\xi = 10$ nm), with the effective cross section adjusted to match R_N. The agreement is quantified by $\chi^2_{\text{norm}} = 0.96$ (Usadel) and 3.5 (KO-1). (c) Simulated spatial profiles of the superconducting gap for NbN and TiN multilayer nanobridges at $T = 0.1T_c$ ($L = 30$ nm, $W = 60$ nm). Proximity effects lead to a $\sim 5\%$ suppression in NbN and a $\sim 60\%$ enhancement in TiN. Figure from [1].

currents, and not systematically in every measurement. The variable thickness geometry helps in this respect: the weak link is connected to banks much thicker than the bridge, which increase the cross-section available for heat conduction away from the constriction compared to planar Dayem bridges of uniform thickness [121, 122]. Non-hysteretic operation of variable thickness nanobridges has indeed been reported, for example in TiN devices [123]. To systematically evaluate device performance, the critical current I_c and normal state resistance R_N were extracted from a series of nominally identical junctions fabricated under identical conditions, while varying the etching time in the final fabrication step. The resulting distribution is shown in Fig. 3.9(b), where two distinct device populations can be identified. Junctions that underwent incomplete etching (gray region) display lower resistance values due to the presence of residual Nb in the junction region. In this regime, both TiN and NbN based devices exhibit similar transport characteristics, indicating that

conduction is dominated by the metallic Nb layer. In contrast, properly etched junctions follow the trends predicted by both the KO-1 model and the three-dimensional Usadel based simulations. The numerical modeling was performed assuming a bridge length $L = 30$ nm and a coherence length $\xi = 10$ nm for the nitride layers. The effective cross section was adjusted to reproduce the experimentally measured normal state resistance, without introducing additional free parameters. The simulations capture the spatial redistribution of the superconducting order parameter within the multilayer stack, highlighting the role of proximity effects between the nitride weak link and the Nb layer. The agreement between experimental data and theoretical predictions was quantified using a normalized χ^2 metric:

$$\chi^2_{norm} = \sum_{i=1}^{N} \frac{(O_i - E_i)^2}{N E_i} \tag{3.2.1}$$

where O_i represents the measured critical current and E_i the corresponding value obtained from either the KO-1 model or the three-dimensional simulations. For the NbN devices, which constitute the largest dataset, the analysis yields $\chi^2_{norm} = 0.96$ for the three-dimensional model and 3.5 for the KO-1 model. The lower χ^2_{norm} obtained with the three-dimensional approach indicates a significantly improved agreement with the experimental data, underscoring the importance of explicitly accounting for multilayer geometry and proximity effects in the modeling of nanobridge junctions. The simulated superconducting gap profiles, shown in Fig. 3.9(c), provide further insight into the role of proximity effects within the multilayer structure. In NbN based junctions, the superconducting gap is reduced by approximately 5% due to coupling with the Nb layer. In contrast, TiN based junctions exhibit a substantial enhancement of the gap, on the order of 60%, indicating a stronger redistribution of superconducting correlations within the stack. These results demonstrate how the multilayer architecture can be exploited to engineer the effective superconducting properties of the weak link, with direct consequences on the critical current and overall transport behavior [1].

3.3 SQUIDs

SQUID devices were realized by integrating two nanobridge junctions into a superconducting loop with lateral dimensions of approximately 4×4 μm^2. The choice of a micron-scale loop, rather than a nanoscale geometry, allows magnetic flux tuning via an on-chip flux line, avoiding the need for externally applied magnetic fields and enabling straightforward experimental control. Although

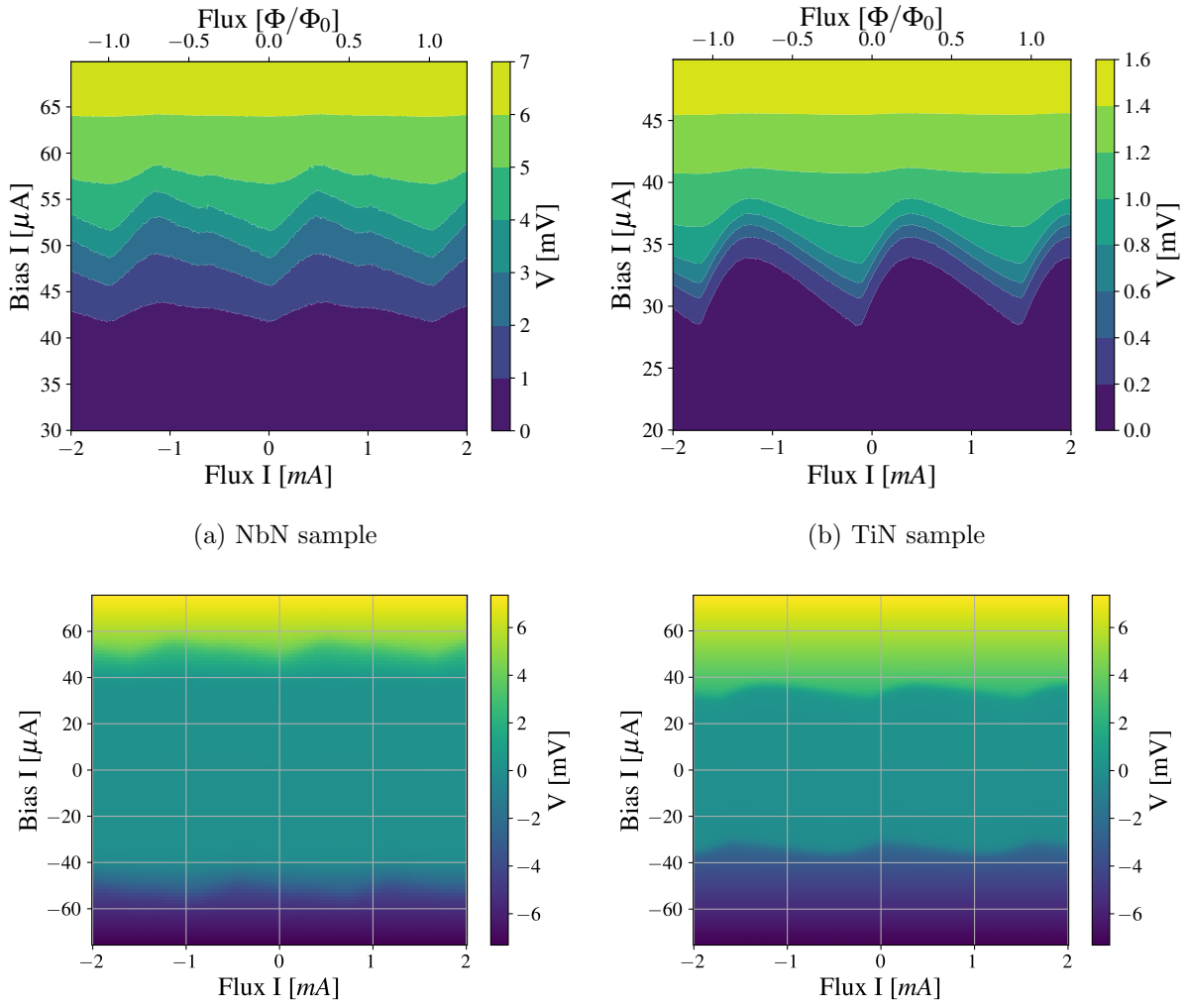

(a) NbN sample

(b) TiN sample

(c) NbN sample

(d) TiN sample

Figure 3.10: Flux modulation of the critical current in SQUIDs based on (a,c) NbN (Sample A) and (b,d) TiN (Sample B). The NbN device shows a modulation depth of about 5%, while the TiN device reaches approximately 20%. The relatively limited modulation depth is mainly attributed to the asymmetry between the two nanobridges, while the loop inductance ($\beta_L \approx 0.25$) plays only a minor role. Panels (c) and (d) display the full modulation under positive and negative current bias, highlighting asymmetries arising from differences in critical current and CPR between the two nanobridges. Figure adapted from [1].

larger than typical nanoSQUIDs reported in the literature [48, 49, 51, 107, 111, 119, 124, 125], the devices exhibit clear periodic modulation of the critical current, with amplitudes of about 20% for TiN based SQUIDs and 5% for NbN based ones (Fig. 3.10). The reduced modulation depth observed in NbN devices is likely related to fabrication induced variations, such as non uniform

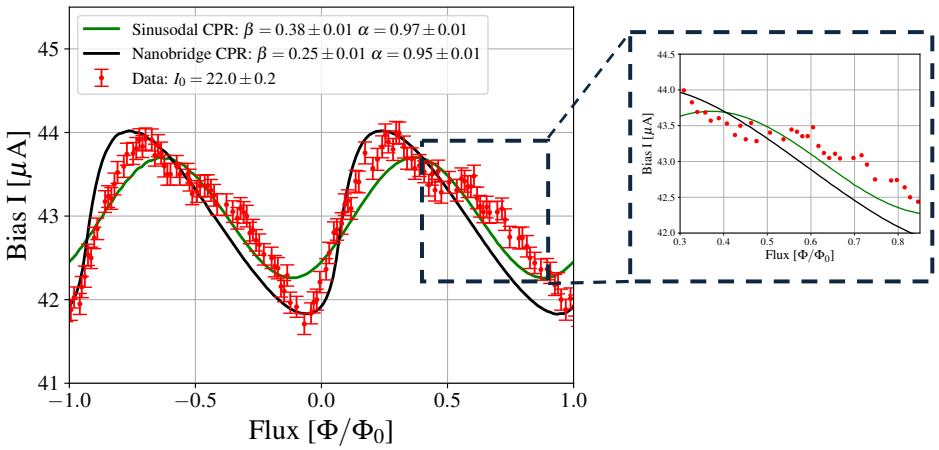

(a)

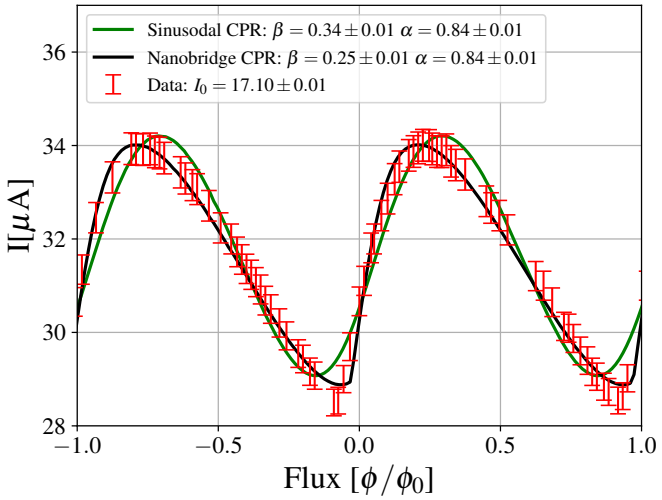

(b)

Figure 3.11: Measured SQUID critical current as a function of magnetic flux together with theoretical fits. (a) NbN based SQUID, with inset showing a zoom of a small feature associated with higher harmonic contributions to the CPR. (b) TiN based SQUID. Solid lines represent fits obtained using an asymmetric dc SQUID model including finite loop inductance, comparing both sinusoidal and nanobridge specific CPRs [2]. Figure adapted from [1].

etching or thickness fluctuations. This interpretation is supported by the spread in critical currents measured across nominally identical NbN nanobridges on the same chip, which range from a few tens of μA up to ~ 50 μA in the SQUID configuration. In the following analysis, heat flow in the junction region is not included. This is justified because the quantity analysed is the switching current from the zero-voltage state, where no power is dissipated in the nanobridges: heating only takes place after the switching event, in the resistive state, and it therefore affects the retrapping

current but not the measured $I_c(\Phi)$ [121]. To quantitatively describe the experimental interference patterns, the data were analyzed within the framework of an asymmetric dc SQUID model. In this formalism, the normalized total current i and circulating current j are expressed as [4]

$$i = (1-\alpha)I(\pi\delta_1) + (1+\alpha)I(\pi\delta_2) \tag{3.3.1}$$

$$j = (1-\alpha)I(\pi\delta_1) - (1+\alpha)I(\pi\delta_2) \tag{3.3.2}$$

where α quantifies the asymmetry between the two junctions, δ_1 and δ_2 are the phase differences across each junction, and $I(\delta)$ denotes the current-phase relation (CPR). Flux quantization imposes the constraint

$$\delta_2 - \delta_1 = 2\pi\Phi_{\text{ext}} + \pi\beta_L\, j \tag{3.3.3}$$

where Φ_{ext} is the externally applied magnetic flux normalized to the flux quantum. Both i and j are normalized to the average critical current I_0. The screening parameter β_L, which determines the importance of inductive effects, is given by [126]

$$\beta_L = \frac{2L_{\text{loop}}I_0}{\Phi_0} \tag{3.3.4}$$

with L_{loop} the geometric inductance of the loop. This is the definition used for the dc SQUID in The SQUID Handbook [4], which follows Tesche and Clarke [126], with I_0 the critical current of a single junction. Physically, β_L compares the flux generated in the loop by a circulating current equal to I_0, $L_{\text{loop}}I_0$, with half a flux quantum. Equivalently, using the Josephson inductance $L_J = \Phi_0/(2\pi I_0)$, $\beta_L = L_{\text{loop}}/(\pi L_J)$. For $\beta_L \ll 1$ the loop cannot screen the applied flux, the phase difference imposed by the external flux is fully transferred to the junctions and the critical current modulation is maximal; for $\beta_L \gtrsim 1$ the circulating current partially screens the applied flux and the modulation depth decreases, approximately as $\Delta I_c/I_{c,\max} \approx 1/(1+\beta_L)$ for a symmetric SQUID [126]. A second definition, $\beta_L' = 2\pi L_{\text{loop}}I_0/\Phi_0 = L_{\text{loop}}/L_J$, is also found in the literature, in particular for rf SQUIDs; it is larger by a factor π than the one used here. For the TiN based SQUID (Sample B), fitting the data assuming a sinusoidal CPR yields $\beta_L \approx 0.34 \pm 0.01$. When instead adopting the nanobridge CPR derived in Ref. [2], the extracted value decreases to $\beta_L = 0.25 \pm 0.01$, with a corresponding critical current $I_0 = 17.10 \pm 0.01$ μA. This result is consistent with an independent estimate based on the loop geometry, which gives $L_{\text{loop}} \approx 15$ pH and, via Eq. 3.3.4, $\beta_L = 2 \times 15$ pH $\times$ 17.1 μA$/(2.07 \times 10^{-15}$ Wb$) \approx 0.25$ (with the alternative definition $\beta_L' = \pi\beta_L \approx 0.78$). A similar trend is observed for the NbN based SQUID. In this case, a sinusoidal

CPR leads to $\beta_L \approx 0.38$, while the nanobridge CPR yields $\beta_L \approx 0.25$. However, both values deviate from the geometrical estimate of $\beta_L \approx 0.32$, suggesting that neither model fully captures the behavior of NbN nanobridges. This discrepancy can be attributed to the short coherence length of NbN, which promotes the emergence of higher harmonics and potentially multivalued CPRs, as reported in previous works [117, 127, 128]. Consistently, a small bump is visible near $0.5\,\Phi_0$ in Fig. 3.11(a), a characteristic signature of higher order harmonic contributions [127]. Additional deviations may arise from differences in the CPRs of the two junctions forming the SQUID, further reducing the modulation depth. At present, the combined effects of higher harmonics, multivalued CPR behavior, and junction asymmetry make a fully quantitative description challenging. Finally, both TiN and NbN SQUIDs exhibit a strong asymmetry parameter ($\alpha > 0.8$), which is the main reason for the limited modulation depth. For $\beta_L \to 0$, the junction critical currents are $(1 \mp \alpha)I_0$ and the SQUID critical current varies between $I_{c,\max} = 2I_0$ at integer flux quanta and $I_{c,\min} = 2\alpha I_0$ at half-integer flux quanta, so that the modulation depth is $\Delta I_c/I_{c,\max} = 1 - \alpha$. The measured modulation depths of about 20% (TiN) and 5% (NbN) therefore correspond to $\alpha \approx 0.8$ and $\alpha \approx 0.95$, respectively, consistent with the fits. By comparison, a symmetric SQUID with $\beta_L \approx 0.25$ would show a modulation depth close to 80%, so the loop inductance plays only a minor role. This pronounced imbalance likely originates from the extreme sensitivity of nanobridge critical currents to small geometric variations, given that the junction dimensions are comparable to the superconducting coherence length. Fabrication induced inhomogeneities and possible contamination effects may therefore play a significant role in determining both the critical current and the effective CPR of each junction [1].

3.4 Conclusions

In this chapter, we have demonstrated a multilayer nanobridge fabrication process based entirely on electron beam lithography and chlorine based dry etching, enabling the realization of variable thickness nanobridge (VTB) Josephson junctions without the use of focused ion beam milling. Using this approach, we successfully fabricated Nb/NbN and Nb/TiN nanobridges that exhibit well defined switching behavior and clear SQUID interference patterns, confirming that Josephson junctions and functional SQUIDs can be reliably realized with this process. While the measured device characteristics show a strong dependence on the geometric dimensions of the nanobridge,

which are currently difficult to control with high precision in the present fabrication flow, the overall results are encouraging. The observation of reproducible Josephson behavior across multiple devices demonstrates the robustness of the multilayer approach and validates the feasibility of nanobridge based junctions fabricated using standard nanofabrication techniques. The use of multilayer superconducting stacks provides additional degrees of freedom for engineering junction properties, including the critical current and the current phase relation, which are not easily accessible in conventional tunnel junctions. Future work should focus on two main improvements. The first is a better dimensional control of the second etching step. This can be achieved by choosing material combinations with a higher etch selectivity in the chosen etching chemistry, so that the second etch stops reliably on the weak-link layer and the thickness of the bridge is set by the deposited film thickness rather than by the etching time. Since the nitride layers have a high resistivity, this would also reduce the spread in normal state resistance and critical current observed in Section 3.1.4. The second is an improved symmetry between the two junctions of the SQUID. As discussed in Section 3.3, the modulation depth of our devices is limited mainly by the junction asymmetry, $\Delta I_c/I_{c,\max} = 1 - \alpha$, rather than by the loop inductance; a better control of the bridge dimensions, obtained with the more selective etching described above, would therefore directly increase the flux modulation depth and the device uniformity. These improvements will be essential for transitioning nanobridge Josephson junctions to scalable elements for superconducting quantum circuits [1].

4. Microwave Circuits

In the previous chapters, we described the design, fabrication and DC characterisation of nanobridge junctions and SQUIDs. We now turn to the remaining building blocks of superconducting circuits: transmission lines and resonators. In circuit quantum electrodynamics, coplanar waveguide (CPW) resonators are used for qubit readout, as coupling buses and as filters, and their internal quality factor is a direct measure of the microwave losses of the materials and of the fabrication process [20, 21]. Since the nanobridges of Chapter 3 are made from multilayer stacks, it is important to know how these stacks behave at microwave frequencies, in terms of both losses and kinetic inductance, before they can be used in quantum circuits.

The objectives of this chapter are therefore: to design and characterise CPW resonators made from the same NbN and TiN based multilayer stacks used for the nanobridges; to study how the multilayer structure affects the kinetic inductance, using the numerical model of Chapter 2 to describe the proximity effect; and to combine resonators and nanobridge SQUIDs into flux-tunable resonators. The chapter is organised as follows. Sections 4.1 to 4.4 review the theory of transmission lines, lumped and distributed resonators, coupling and scattering parameters, largely following Ref. [129]. Section 4.5 introduces coplanar waveguides, the transmission spectrum of notch-type resonators and the kinetic inductance of single-layer and multilayer films. Section 4.6 describes the design and fabrication of the devices and the sample package, and Section 4.7 presents the cryogenic setup and the measurements of the internal quality factors and of the kinetic inductance. Finally, Section 4.8 discusses the flux-tunable resonators, and Section 4.9 summarises the results and the future developments.

4.1 Transmission line basics

A transmission line is a distributed electrical system and can be modeled as a cascade of infinitesimal lumped elements, as shown in Fig. 4.1. In this representation, R and L denote the series resistance and inductance per unit length, while C and G represent the shunt capacitance and conductance per unit length, respectively. Applying Kirchhoff's voltage and current laws to this

model leads to the telegrapher's equations

$$\frac{dV(z)}{dz} = -(R + j\omega L)I(z) \tag{4.1.1}$$

$$\frac{dI(z)}{dz} = -(G + j\omega C)V(z) \tag{4.1.2}$$

Combining these equations yields a second-order differential equation for the current

$$\frac{d^2I(z)}{dz^2} - \gamma^2 I(z) = 0 \tag{4.1.3}$$

where the complex propagation constant is defined as

$$\gamma = \alpha + j\beta = \sqrt{(R + j\omega L)(G + j\omega C)} \tag{4.1.4}$$

The general solutions for voltage and current along the line can be written as

$$V(z) = V_0^+ e^{-j\beta z} + V_0^- e^{+j\beta z} \tag{4.1.5}$$

$$I(z) = \frac{V_0^+}{Z_0} e^{-j\beta z} - \frac{V_0^-}{Z_0} e^{+j\beta z} \tag{4.1.6}$$

where V_0^+ and V_0^- are the amplitudes of the forward- and backward propagating waves, and the characteristic impedance of the line is

$$Z_0 = \frac{R + j\omega L}{\gamma} \tag{4.1.7}$$

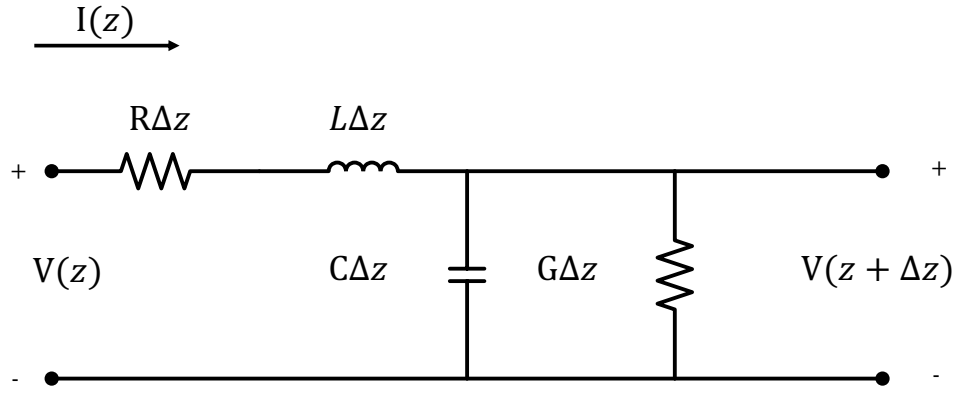

Figure 4.1: Lumped-element representation of a transmission line. Adapted from [129].

When the transmission line is terminated by a load impedance Z_L, as illustrated in Fig. 4.2, part of the incident wave is reflected. The reflection coefficient at the load ($z = 0$) is given by

$$\Gamma = \frac{V_0^-}{V_0^+} = \frac{Z_L - Z_0}{Z_L + Z_0} \tag{4.1.8}$$

When the load has the same impedance as the line, the line is said to be impedance matched and no reflection occurs. The voltage and current distributions along the line then become

$$V(z) = V_0^+ \left(e^{-j\beta z} + \Gamma e^{+j\beta z}\right) \tag{4.1.9}$$

$$I(z) = \frac{V_0^+}{Z_0} \left(e^{-j\beta z} - \Gamma e^{+j\beta z}\right) \tag{4.1.10}$$

From these expressions, the input impedance measured at a distance $l = -z$ from the load can be written as

$$Z_{in} = Z_0 \frac{Z_L + jZ_0 \tan(\beta l)}{Z_0 + jZ_L \tan(\beta l)} \tag{4.1.11}$$

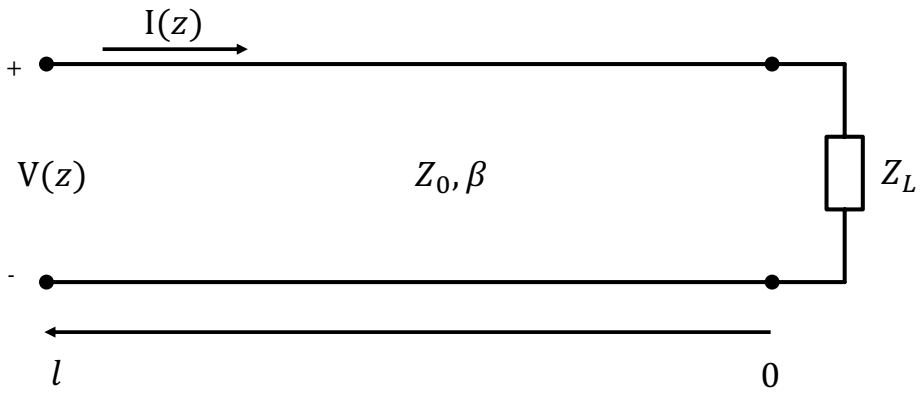

Figure 4.2: Transmission line terminated by a load impedance. Adapted from [129].

4.2 Resonators

Resonators are central elements in circuit QED, as they define well controlled electromagnetic modes that can be coupled to quantum systems. In many situations, their behavior can be accurately captured using simple lumped-element models, with the simplest representations being series or parallel resonators.

4.2.1 Series resonator

We first consider the series resonator shown in Fig. 4.3. Its input impedance is

$$Z_{in} = R + j\omega L - j\frac{1}{\omega C} \tag{4.2.1}$$

which can be rewritten as

$$Z_{in} = R + j\omega L\left(\frac{\omega^2 - \omega_0^2}{\omega^2}\right) \simeq R + j2L(\omega - \omega_0) \tag{4.2.2}$$

where the resonance frequency is

$$\omega_0 = \frac{1}{\sqrt{LC}} \tag{4.2.3}$$

The quality factor is defined as

$$Q = \omega \frac{\text{average stored energy}}{\text{power dissipated}} \tag{4.2.4}$$

where the magnetic and electric energies stored in the resonator are

$$W_m = \frac{1}{4}|I|^2 L, \qquad W_e = \frac{1}{4}|I|^2 \frac{1}{\omega^2 C} \tag{4.2.5}$$

and the power dissipated in the resistor is

$$P_{\text{loss}} = \frac{1}{2}|I|^2 R \tag{4.2.6}$$

At resonance, where $W_m = W_e$, the unloaded quality factor becomes

$$Q_0 = \frac{\omega_0 L}{R} = \frac{1}{\omega_0 RC} \tag{4.2.7}$$

The quality factor quantifies the losses in the resonator: higher Q_0 corresponds to lower dissipation. For instance, in superconducting circuits, loss mechanisms include conductor losses, dielectric losses, and radiation losses, with conductor losses typically small but not zero [27]. Near resonance, the input impedance can be expressed in terms of the quality factor as

$$Z_{in} = R\left(1 + j\frac{2Q_0\Delta\omega}{\omega_0}\right) \tag{4.2.8}$$

The complex power delivered to the resonator is

$$P_{in} = \frac{1}{2}Z_{in}|I|^2 \tag{4.2.9}$$

The half-power condition corresponds to $|Z_{in}|^2 = 2R^2$, leading to the familiar relation between bandwidth (BW=$2\Delta\omega/\omega_0$) and quality factor,

$$\text{BW} = \frac{1}{Q_0} \tag{4.2.10}$$

Losses can also be incorporated phenomenologically by introducing a complex resonance frequency,

$$\omega_0 \to \omega_0\left(1 + \frac{j}{2Q_0}\right) \tag{4.2.11}$$

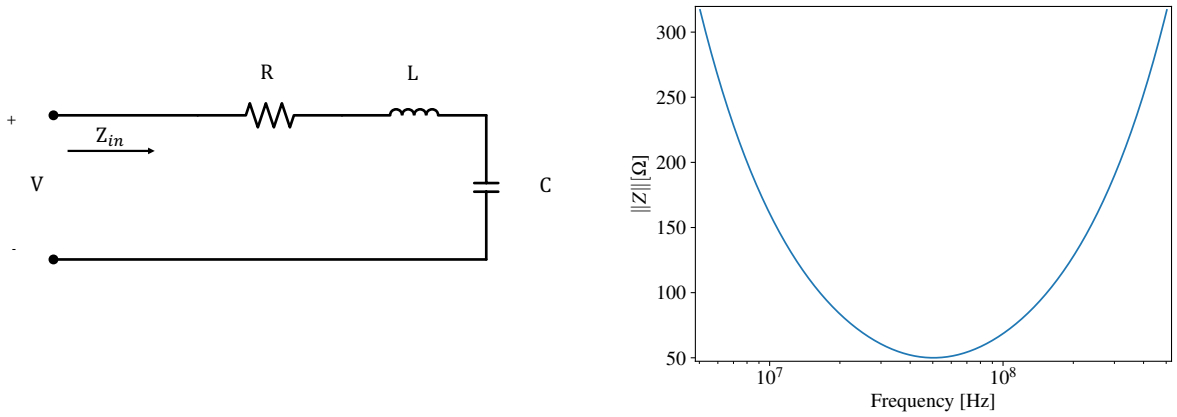

(a) (b)

Figure 4.3: (a) Lumped-element model of a series resonator and (b) corresponding input impedance. Adapted from [129].

4.2.2 Parallel resonator

A parallel resonator, shown in Fig. 4.4, has an input impedance

$$Z_{in} = \left(\frac{1}{R} + \frac{1}{j\omega L} + j\omega C\right)^{-1} \simeq \frac{R}{1 + 2j\Delta\omega RC} \tag{4.2.12}$$

Using arguments analogous to those for the series resonator, the unloaded quality factor is found to be

$$Q_0 = \frac{R}{\omega_0 L} \tag{4.2.13}$$

which allows the impedance to be written as

$$Z_{in} = \frac{R}{1 + 2jQ_0\Delta\omega/\omega_0} \tag{4.2.14}$$

In contrast to the series case, a parallel resonator exhibits an impedance maximum at resonance, often referred to as an antiresonance. The half-power condition $|Z_{in}|^2 = R^2/2$ again leads to

$$\text{BW} = \frac{1}{Q_0} \tag{4.2.15}$$

4.3 Transmission line resonators

Sections of transmission line can also function as resonators, with their behavior determined by the boundary conditions imposed at the terminations. In the following, we discuss two configurations

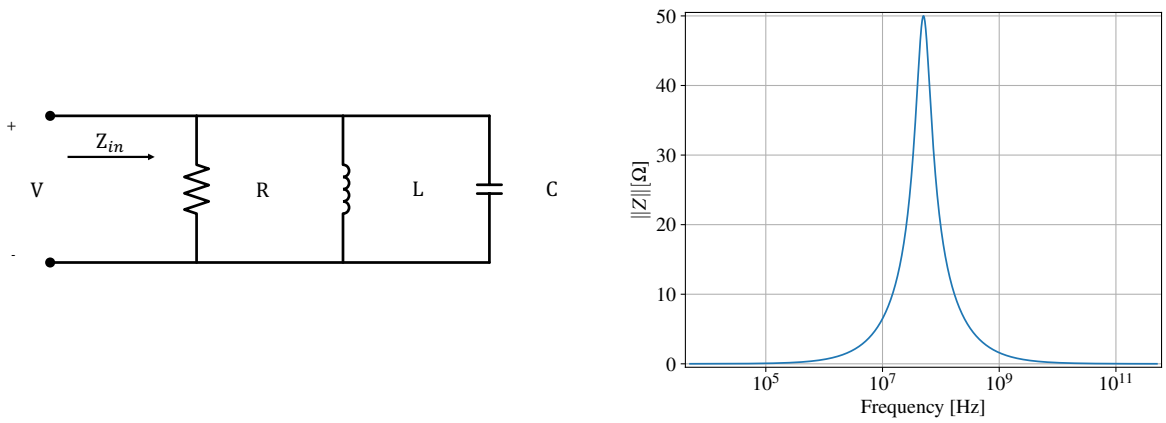

(a) (b)

Figure 4.4: (a) Lumped-element model of a parallel resonator and (b) corresponding input impedance. Adapted from [129].

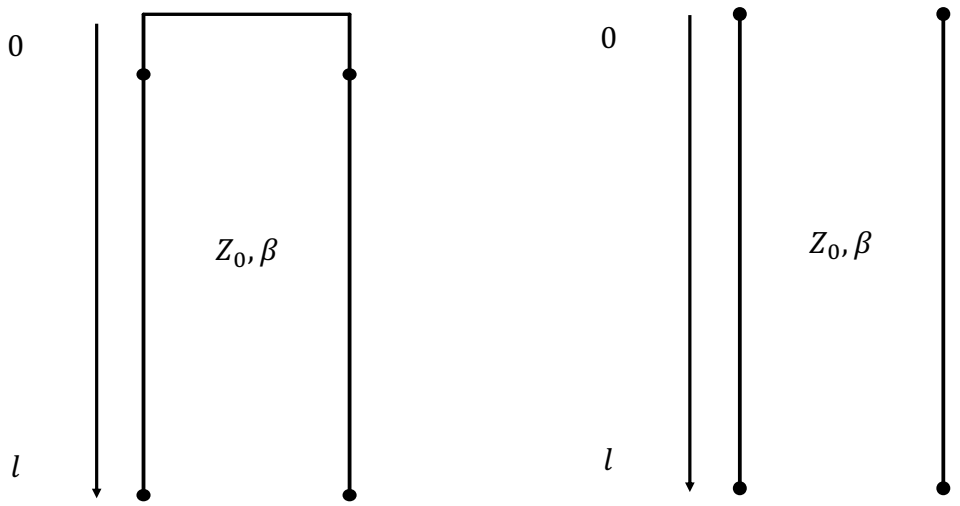

(a) (b)

Figure 4.5: Schematic overview of a) Short-circuited $\lambda/4$ line b) Open-circuited $\lambda/2$ line

commonly used in this thesis.

4.3.1 Short-circuited $\lambda/4$ line

For a short-circuited transmission line ($Z_L = 0$, Fig. 4.5(a)), Eq. 4.1.11 gives

$$Z_{in} = Z_0 \tanh\left((\alpha + j\beta)l\right) \tag{4.3.1}$$

For low-loss lines, $\tanh(\alpha l) \simeq \alpha l$. Near resonance, $\omega = \omega_0 + \Delta\omega$, a quarter-wavelength line satisfies

$$\beta l = \frac{\pi}{2} + \frac{\pi \Delta\omega}{2\omega_0} \tag{4.3.2}$$

Under these conditions, the input impedance becomes

$$Z_{in} \simeq Z_0 \left(\alpha l + j \frac{\pi \Delta\omega}{2\omega_0} \right)^{-1} \tag{4.3.3}$$

which has the same functional form as a parallel RLC resonator with effective parameters

$$R = \frac{Z_0}{\alpha l}, \quad L = \frac{4Z_0}{\pi\omega_0}, \quad C = \frac{\pi}{4\omega_0 Z_0} \tag{4.3.4}$$

The corresponding quality factor is

$$Q_0 = \omega_0 RC = \frac{\beta}{2\alpha} \tag{4.3.5}$$

4.3.2 Open-circuited $\lambda/2$ line

A half-wavelength open-circuited transmission line ($Z_L \to \infty$, Fig. 4.5(b)) has an input impedance

$$Z_{in} = \frac{Z_0}{\alpha l + j(\pi \Delta\omega / \omega_0)} \tag{4.3.6}$$

which again corresponds to a parallel resonator with

$$R = \frac{Z_0}{\alpha l}, \quad C = \frac{\pi}{2 Z_0 \omega_0}, \quad L = \frac{1}{\omega_0^2 C} \tag{4.3.7}$$

and quality factor

$$Q_0 = \omega_0 RC = \frac{\beta}{2\alpha} \tag{4.3.8}$$

4.4 Loaded quality factor and coupling

When a resonator is coupled to an external circuit, energy can leak out through the coupling channel. The resulting loaded quality factor is defined as

$$Q_L^{-1} = Q_c^{-1} + Q_0^{-1} \tag{4.4.1}$$

where Q_c accounts for coupling losses and Q_0 is the internal quality factor. A useful dimensionless parameter is the coupling coefficient

$$g = \frac{Q_0}{Q_c} \tag{4.4.2}$$

The resonator is said to be undercoupled for $g < 1$, critically coupled for $g = 1$, and overcoupled for $g > 1$. As a relevant example, we consider a gap-coupled open-circuited $\lambda/4$ resonator, shown in Fig. 4.6. Assuming initially a lossless system, the normalized input impedance is

$$z = \frac{Z}{Z_0} = -j\left(\frac{\tan\beta l + b_c}{b_c \tan\beta l}\right) \tag{4.4.3}$$

where $b_c = Z_0\omega C$ characterizes the coupling strength. Resonance occurs when $z = 0$, i.e.

$$\tan\beta l + b_c = 0 \tag{4.4.4}$$

Since typically $b_c \ll 1$, the resonance frequency ω_1 is close to that of the unloaded resonator, for which $\beta l = \pi/2$.

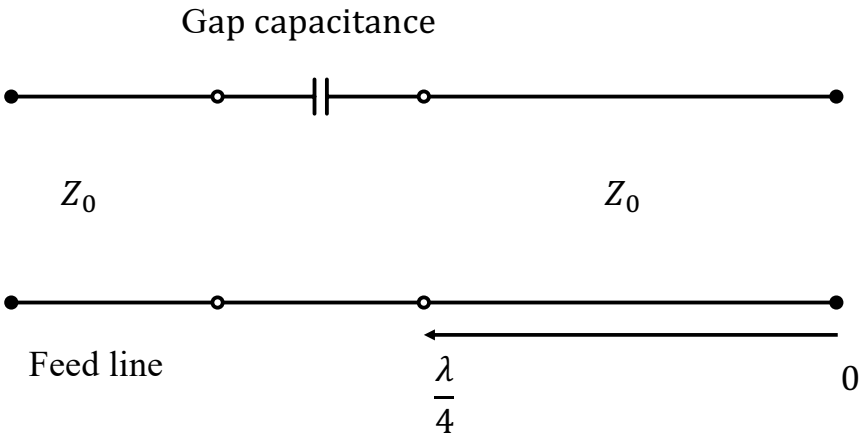

Figure 4.6: Capacitive coupling between a feedline and a resonator. Adapted from [129].

Expanding the impedance around ω_1 yields

$$z(\omega) \simeq (\omega - \omega_1)\frac{dz}{d\beta l}\frac{d(\beta l)}{d\omega}\bigg|_{\omega_1} \tag{4.4.5}$$

Evaluating the derivatives gives

$$\frac{dz}{d\beta l}\bigg|_{\omega_1} \simeq \frac{j}{b_c^2}, \qquad \frac{d(\beta l)}{d\omega} = \frac{l}{v_p} \tag{4.4.6}$$

so that

$$z(\omega) \simeq \frac{j\pi(\omega - \omega_1)}{\omega_1 b_c^2} \tag{4.4.7}$$

Including losses via a complex resonance frequency $\omega_1(1 + j/2Q_0)$ leads to

$$z(\omega) = \frac{\pi}{2Q_0 b_c^2} + j\frac{\pi(\omega - \omega_1)}{\omega_1 b_c^2} \tag{4.4.8}$$

The coupled resonator therefore behaves as a series RLC circuit with an effective resistance

$$R = \frac{Z_0 \pi}{2 Q_0 b_c^2} \tag{4.4.9}$$

The coupling coefficient can then be written as

$$g = \frac{Z_0}{R} = \frac{2 Q_0 b_c^2}{\pi} \tag{4.4.10}$$

By adjusting the coupling capacitance, the resonator can be tuned between the undercoupled, critically coupled, and overcoupled regimes. In superconducting circuits, accurate extraction of the internal quality factor typically requires $g < 10$ [27, 130].

4.4.1 Scattering matrix

In practical microwave applications, the characterization of an N-port network is most conveniently performed in terms of propagating waves rather than voltages and currents. In particular, describing the incident, transmitted, and reflected signal components at each port provides a complete representation of the network response. This formalism leads naturally to the definition of the scattering matrix, or S-matrix, which relates the incident voltage waves at the ports to the reflected ones [129]. The scattering matrix elements are defined as

$$\hat{S}_{ij} = \left. \frac{V_i^{\text{out}}}{V_j^{\text{in}}} \right|_{V_k^{\text{in}}=0,\, k \neq j} \tag{4.4.11}$$

where V_j^{in} is the incident wave amplitude at port j and V_i^{out} is the outgoing wave amplitude at port i. Equation (4.4.11) requires the network to be excited at a single port j, while all other ports are terminated with a Z_0 load. In this thesis, however, we will restrict our analysis to two-port networks, which is sufficient to fully characterize superconducting microwave resonators coupled to a transmission line. In this case, the S-matrix can be written as

$$\begin{pmatrix} V_1^{\text{out}} \\ V_2^{\text{out}} \end{pmatrix} = \begin{pmatrix} S_{11} & S_{12} \\ S_{21} & S_{22} \end{pmatrix} \begin{pmatrix} V_1^{\text{in}} \\ V_2^{\text{in}} \end{pmatrix} \tag{4.4.12}$$

All scattering parameters S_{ij} can be directly measured using a Vector Network Analyzer (VNA), which probes the network response over a range of frequencies and input power levels. This capability makes S-parameters a powerful and experimentally accessible tool for characterizing superconducting microwave resonators.

4.5 Ungrounded coplanar waveguides

In circuit QED, a commonly used transmission line geometry is the ungrounded coplanar waveguide (CPW). As shown in Fig. 4.7, it consists of a central conductor of width W and thickness t, separated by gaps of width S from the adjacent ground planes. The term ungrounded distinguishes this geometry from variants that include an additional ground plane beneath the substrate.

CPWs support quasi-TEM modes, with electric and magnetic fields predominantly transverse to the direction of propagation. This allows the characteristic impedance to be determined using conformal mapping techniques. Conformal mapping is a method from complex analysis in which the cross-section of the line, described in the complex plane $z = x + iy$, is transformed by an analytic function (for the CPW, a Schwarz-Christoffel transformation) into a simpler geometry, such as a parallel-plate capacitor, whose capacitance is known. Since conformal transformations preserve the solutions of Laplace's equation, the electrostatic problem can be solved in the simpler geometry and the capacitance per unit length of the original line obtained analytically [129]. In the quasi-TEM approximation, the inductance per unit length then follows from $L_g C = \epsilon_{\text{eff}}/c^2$, and the characteristic impedance from $Z_0 = \sqrt{L_g/C}$. In the limit of zero conductor thickness, the geometric inductance and capacitance per unit length are given by [27]

$$L_g = \frac{\mu_0 K(\kappa')}{4K(\kappa)}, \qquad C = 4\epsilon_0 \epsilon_{\text{eff}} \frac{K(\kappa)}{K(\kappa')} \tag{4.5.1}$$

where $\epsilon_{\text{eff}} = (1 + \epsilon_r)/2$, K is the complete elliptic integral of the first kind, $\kappa = S/(S + 2W)$, and $\kappa' = \sqrt{1 - \kappa^2}$ [131]. For finite conductor thickness, these expressions become more involved and numerical tools such as Sonnet or HFSS are typically used. However, at GHz frequencies the skin depth is of the order of a micron, while the film thickness in our devices is approximately 100 nm, making the zero-thickness approximation sufficiently accurate.

4.5.1 Transmission spectrum of microwave resonators

The superconducting microwave resonators implemented in this thesis are notch-type resonators coupled to a transmission line. In a notch-type configuration, the resonator is not placed in series between the input and output ports, but is side-coupled, here capacitively, to a feedline that passes by it. Away from resonance the signal is transmitted along the feedline almost unperturbed, while at resonance the field interferes destructively with the transmitted wave, producing a dip, or notch,

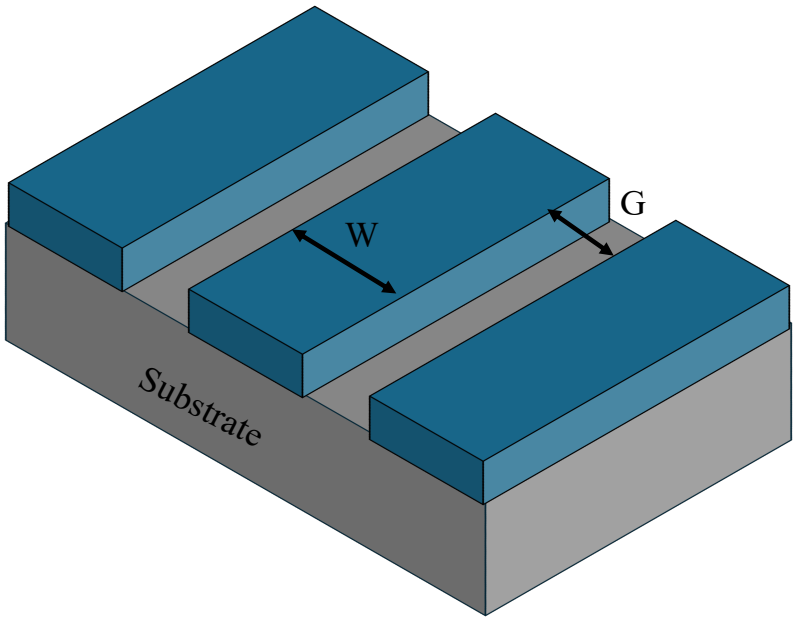

Figure 4.7: Geometry of a coplanar waveguide: central conductor of width W, separated by G from the ground plane. Adapted from [131].

in $|S_{21}|$. This is different from transmission-type resonators, coupled in series between two ports, which show a peak in transmission at resonance. A practical advantage of the notch configuration is that several resonators with different frequencies can be coupled to the same feedline and measured at once, as done in this work. For these devices the S-matrix can be expressed as [26, 132]

$$\mathbf{S} = \begin{pmatrix} \frac{Z_0}{Z_0+2Z} & \frac{2Z}{Z_0+2Z} \\ \frac{2Z}{Z_0+2Z} & \frac{Z_0}{Z_0+2Z} \end{pmatrix} \tag{4.5.2}$$

where Z_0 is the characteristic impedance of the transmission line and Z is the input impedance of the resonator. Equation (4.5.2) can be derived from the general two-port relations by treating the resonator as an impedance Z connected in shunt across the transmission line [129]. For the characterization of notch-type resonators, the relevant scattering parameter is the transmission coefficient

$$S_{21} = \frac{2Z}{Z_0+2Z} \tag{4.5.3}$$

The resonator input impedance can be expressed in terms of the resonance frequency ω_r and

the quality factors as [26, 132]

$$Z = Z_0 \frac{Q_c}{2Q_l + iQ_c\left(\frac{\omega}{\omega_r} - 1\right)} \tag{4.5.4}$$

where Q_l is the loaded quality factor and Q_c is the coupling quality factor. Substituting Eq. (4.5.4) into Eq. (4.5.3) yields the transmission response of a notch-type resonator:

$$S_{21} = 1 - \frac{Q_l/Q_c}{1 + 2iQ_l\left(\frac{\omega}{\omega_r} - 1\right)} \tag{4.5.5}$$

In the complex plane, the transmission coefficient S_{21} traces a circle with diameter $d = Q_l/Q_c$. This geometric property enables extraction of the resonator parameters through the circle fitting technique [133]. This approach accounts for experimental imperfections and environmental effects by extending Eq. (4.5.5) to

$$S_{21} = ae^{i\alpha}e^{-i\omega\tau}\left[1 - \frac{Q_l/Q_c\, e^{i\phi}}{1 + 2iQ_l\left(\frac{\omega}{\omega_r} - 1\right)}\right] \tag{4.5.6}$$

where the prefactor models external contributions to the measured signal. The parameter a represents an overall amplitude scaling, α is a constant phase offset, and τ accounts for the electronic delay introduced by the transmission line. The phase ϕ captures impedance mismatches at the input and output ports of the resonator. By fitting the full complex transmission response using Eq. (4.5.6), both internal and coupling quality factors can be extracted with high accuracy.

4.5.2 Kinetic Inductance

Kinetic inductance is a fundamental property of superconductors that becomes particularly important in thin films. Unlike geometric or self-inductance, which stores energy in magnetic fields, kinetic inductance stores energy in the kinetic energy of charge carriers. For a CPW, the total inductance per unit length can be expressed as

$$L_{total} = L_g + L_k = L_g + L_s \cdot g_{Kin} \tag{4.5.7}$$

where L_g is the geometric (magnetic) inductance per unit length, determined only by the cross-sectional geometry of the CPW, L_k is the kinetic inductance per unit length, L_s is the sheet kinetic inductance of the superconductor and g_{Kin} is a geometrical correction factor taking the form $g_{Kin} = g_c + g_g$ [27, 131]:

$$g_c = \frac{1}{4S(1-k^2)K^2(k)}\left[\pi + \ln\frac{4\pi S}{t} - k\ln\frac{1+k}{1-k}\right] \tag{4.5.8}$$

$$g_g = \frac{k}{4S(1-k^2)K^2(k)}\left[\pi + \ln\frac{4\pi(S+2W)}{t} - \frac{1}{k}\ln\frac{1+k}{1-k}\right] \tag{4.5.9}$$

which are valid when $t > \lambda_S/2$, $t < 0.05S$ and $k < 0.8$. A simpler approximate formula can be used for thin films [134]:

$$L_k = \frac{l}{w}\frac{R_{sq}\hbar}{\pi\Delta}\frac{1}{\tanh\left(\Delta/2k_BT\right)} \tag{4.5.10}$$

The origin of the high kinetic inductance of materials such as NbN and TiN can be understood from Eq. (4.5.10). At $T \ll T_C$, $\tanh(\Delta/2k_BT) \to 1$ and the sheet kinetic inductance reduces to $L_{k,\square} = \hbar R_{sq}/(\pi\Delta)$, with $R_{sq} = \rho/t$. The kinetic inductance is therefore proportional to the normal state resistivity and inversely proportional to the superconducting gap. Nitride films such as NbN and TiN are strongly disordered, with a very short electronic mean free path, and their normal state resistivity is more than two orders of magnitude higher than that of Nb (Table 3.2). Physically, a high resistivity corresponds to a low density of superconducting electrons, n_s, and since the kinetic inductance originates from the inertia of the Cooper pairs, $L_k \propto m/(n_s e^2)$, a lower n_s means that a larger kinetic energy, and therefore a larger inductance, is needed to carry the same current. Using the values of Table 3.2 with $\Delta = 1.76\,k_BT_C$, we obtain $L_{k,\square} \approx 0.35$ pH/$\square$ for the 60 nm Nb film, ≈ 47 pH/$\square$ for the 80 nm NbN film and ≈ 470 pH/$\square$ for the 60 nm TiN film. The lower T_C of TiN further increases its kinetic inductance compared to NbN. These high values make nitride films valuable for compact inductive circuit elements and sensitive detectors.

4.5.3 Kinetic inductance in multi-layer devices

The discussion so far has focused on the kinetic inductance of single layer superconducting films. In the devices analyzed in this thesis, however, multiple superconducting layers are present. In this case, the superconducting properties of the film can be modified by the proximity effect, and the resulting kinetic inductance can no longer be described by the single layer model alone. In this section, we analyze the proximity effect using the numerical framework introduced in Chapter 2. The discussion builds upon the results presented in my previous work [2]. A relevant experimental example is the encapsulation technique recently reported in Ref. [140], where a normal metal or a secondary superconducting layer is deposited on top of a superconducting film in order to mitigate surface oxides and improve qubit coherence times. While encapsulation is advantageous, it can introduce proximity effects that redistribute the superconducting order parameter across the multilayer stack. In particular, the superconducting energy gap Δ is reduced in the stronger

Mat.	t [nm]	$\rho[\mu\Omega\cdot\text{cm}]$	ξ [nm]	γ	T_C [K]	$\frac{\min(\Delta_{cap})}{\Delta_0}$ [%]	$L_{k,\text{cap}}/L_{k,0}$	References
Au	10	20	88	0.16	0	95	0.97	Refs. [135, 136]
TiN	15	300	53.6	0.02	4.5	99	0.99	Refs. [97, 115, 125, 137]
Al	10	1.5	110	1.69	1.2	97	0.69	Ref. [80]
Ta	10	21	77	0.17	4.4	99	0.96	Refs. [138, 139]

Table 4.1: Simulated superconducting energy gap (Δ) and kinetic inductance of a 100 nm-thick Nb coplanar waveguide (CPW) with a 10 μm-wide central conductor, assuming $T_C = 9$ K, $\xi = 40$ nm, and $\rho = 7$ $\mu\Omega\cdot$cm [99]. The CPW is capped with the metals listed in Ref. [140], evaluated at $T = 0.1\,T_C$ for Au and $T = 0.1\,T_{CS'}$ for the other materials. Here $\gamma = \rho_S\xi_S/(\rho_N\xi_N)$ is the suppression parameter introduced in Eq. (2.2.12) and discussed in Section 4.5.3. The parameters γ and T_C were obtained or estimated from the cited literature, selecting representative values within the reported ranges. For the kinetic inductance, we show the ratio between the capped ($L_{k,\text{cap}}$) and uncapped ($L_{k,0}$) CPW, highlighting how variations in resistivity and/or superconducting gap influence the kinetic inductance. Table from [2].

superconductor and enhanced in the weaker one. This redistribution has direct consequences for device performance. A reduced gap allows quasiparticle excitations at lower frequencies, while changes in the kinetic inductance can introduce additional impedance mismatches in microwave circuits. Since the condition $\hbar\omega \ll \Delta$ must be satisfied throughout the entire device to suppress quasiparticle generation [9], multilayers can become more sensitive to environmental noise in a cryogenic setting [141]. For this reason, the choice of the encapsulating layer is critical and must account for both its thickness and resistivity. The strength of the proximity effect in such structures is quantified by the parameter

$$\gamma = \frac{\rho_S\xi_S}{\rho_N\xi_N} \tag{4.5.11}$$

where ρ and ξ denote the resistivity and coherence length of the superconducting (S) and normal (N) layers, respectively. The parameter γ, already introduced in the boundary conditions of Eq. (2.2.12), compares the normal state conductance of the two layers over a distance equal to their coherence lengths, ξ/ρ. Its significance is that it sets how strongly the capping layer perturbs the superconductor at the interface: for $\gamma \ll 1$ the capping layer is a poor conductor compared to S and can only weakly draw Cooper pairs from it, so the order parameter in S is almost

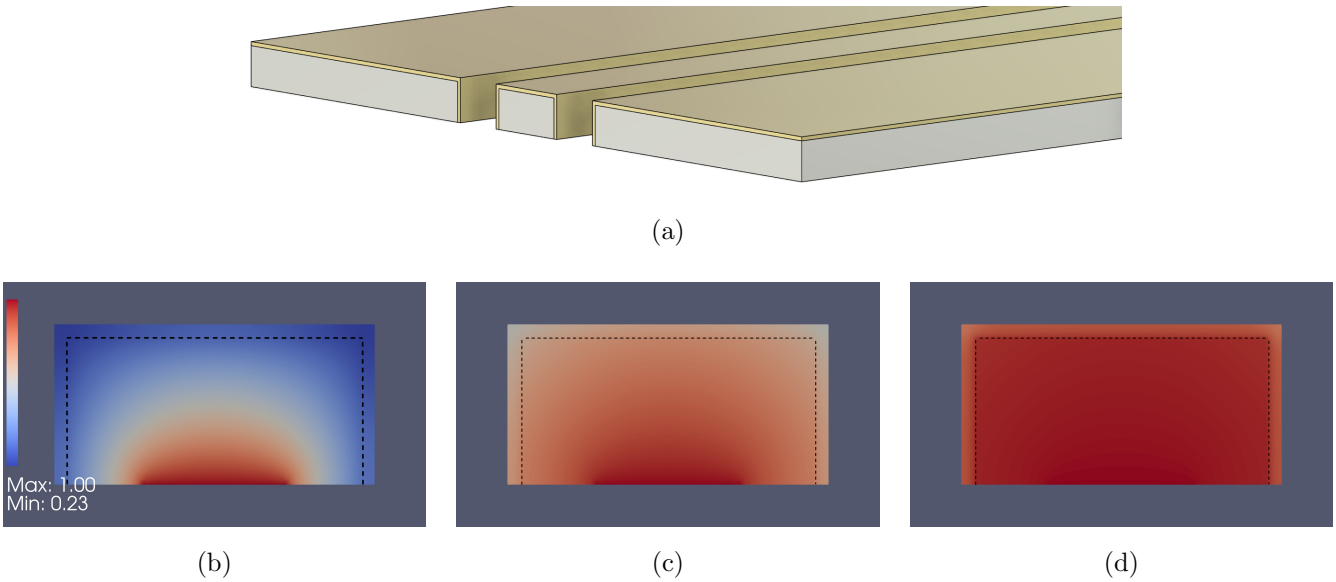

(a) (b) (c) (d)

Figure 4.8: (a) 3D schematic of a multilayer CPW (not to scale). Panels (b) to (d) show the magnitude of the function Φ in the CPW for different values of γ: (b) $\gamma = 10$, (c) $\gamma = 1$, and (d) $\gamma = 0.1$. The dotted line marks the interface between the niobium layer and the encapsulating material. The simulations used $\xi_S = 5\,\xi_N$, $\xi_N = 30$ nm, $\gamma_b = 0.01$, $T/T_{CS} = 0.1$, and layer thicknesses of 200 nm for the superconductor and 20 nm for the normal metal. These results illustrate that the proximity effect strongly depends on γ: larger values of γ significantly suppress the magnitude of Φ, even when the encapsulating layer is thinner than the coherence length. Figure from [2].

unaffected, while for $\gamma \gtrsim 1$ the coupling is strong and the order parameter in S is significantly suppressed near the interface. Figure 4.8 shows the proximity effect in a superconducting coplanar waveguide capped with a normal metal, where an increase in γ results in a reduction of the superconducting gap, in agreement with theoretical expectations. The calculated reductions in Δ for the materials considered in Ref. [140] are summarized in Table 4.1 and Fig. 4.9. A decrease in the superconducting gap leads to an increased quasiparticle density, which in turn degrades the internal quality factor of the resonator and, in the case of qubits, shortens the relaxation time [142]. To minimize quasiparticle generation and associated losses, it is therefore advantageous to select materials with critical temperature T_C similar to the original film and combinations of resistivity and coherence length such that $\gamma < 1$, as is the case for materials such as tantalum and TiN. The modified superconducting gap is then used to evaluate the kinetic inductance of the multilayer film, integrating the contributions of the individual layers in parallel, using Eq. (4.5.10).

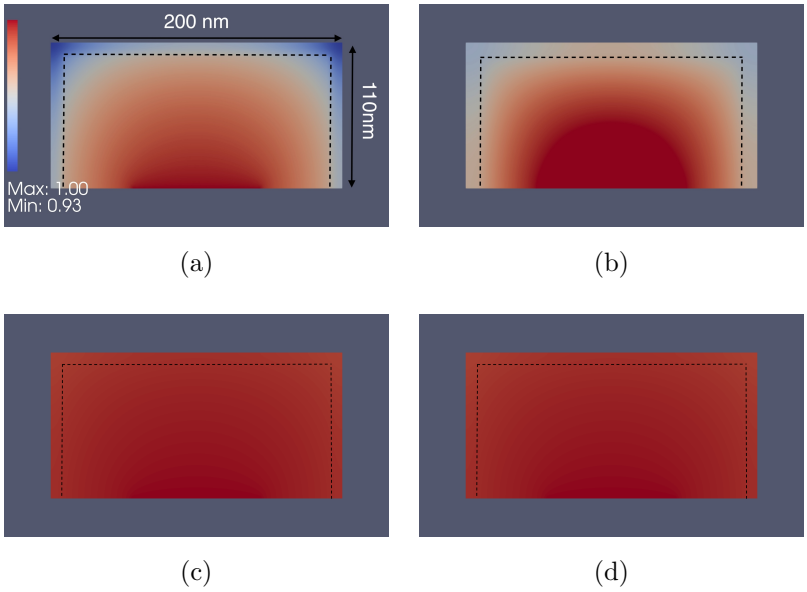

Figure 4.9: Simulated magnitude of the function Φ in a CPW (not to scale for clarity), capped with the materials listed in Tab. 4.1: (a) Au, (b) Al, (c) TiN, and (d) Ta. The dotted line marks the interface between the niobium and the encapsulating layer. As expected, materials with low γ have only a minor effect on Φ, while larger γ values lead to a more pronounced suppression. Figure from [2].

The ratio of the kinetic inductance with and without the capping layer is reported in Table 4.1. The largest variations in kinetic inductance are observed for materials exhibiting the strongest reduction in the superconducting gap, as well as for aluminium, due to its low resistivity. These results indicate that even when the change in Δ is modest, the resistivity of the encapsulating layer plays a dominant role in determining the total kinetic inductance, even for relatively small capping layer thicknesses.

4.6 Design of Superconducting Transmission Lines and Resonators

The superconducting transmission lines and resonators were designed using the conformal mapping equations for coplanar waveguides. These analytical expressions were used to obtain an initial estimate of the geometrical parameters required to achieve a target characteristic impedance of 50 Ω. The resulting design was then implemented in Qiskit Metal [82] and refined through full-

wave electromagnetic simulations using Ansys HFSS [143], as shown in Fig. 4.10. By iteratively adjusting the geometry, a characteristic impedance of 50 Ω was obtained for a central conductor width $W = 10$ μm and a gap $S = 6$ μm on a silicon substrate with thickness 525 μm. To estimate the coupling strength between the resonator and the transmission line, the open-source software developed in [144] was used. This tool allows for a rapid evaluation of the loaded quality factor by varying the length and separation of two coupled coplanar waveguides, as shown in Fig. 4.11.

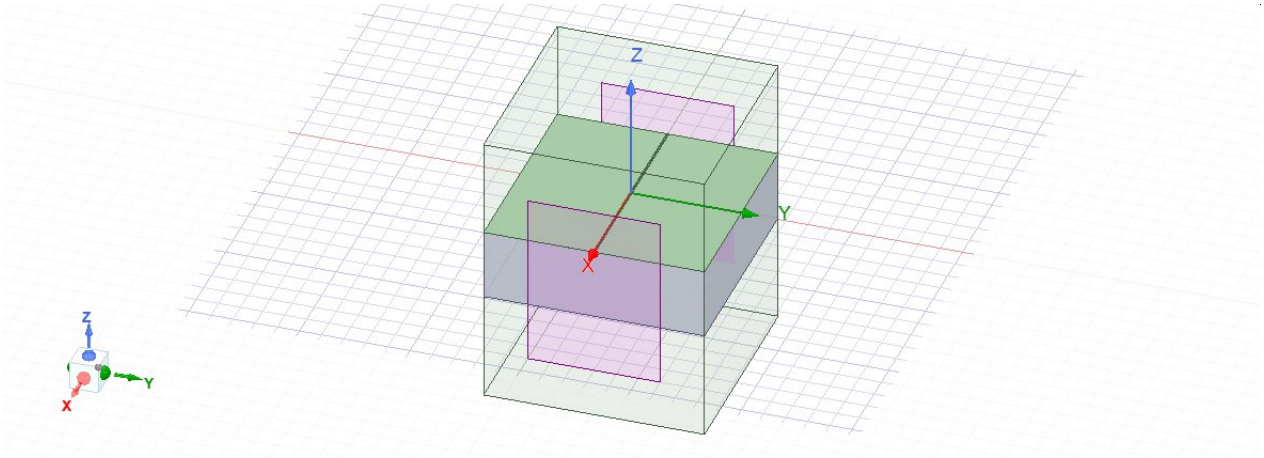

Figure 4.10: Coplanar waveguide simulated in HFSS to extract the characteristic impedance and match it to 50 Ω. As described in [143], a wave port (pink rectangle) with dimensions larger than $3(2S + W)$ in width and $2t$ in height was used.

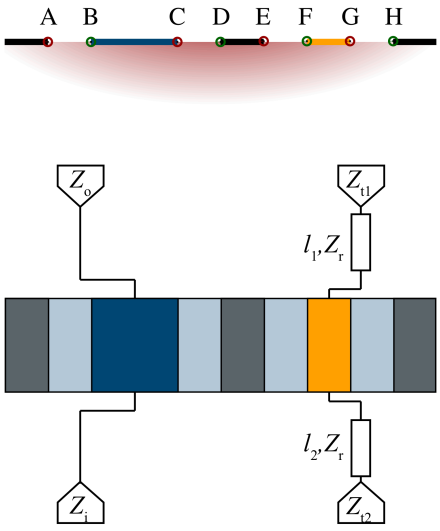

Figure 4.11: Coupling strength and quality factor extraction performed by setting the lengths and separation of two CPWs, using the open-source code from [144].

An initial estimate of the resonator lengths was obtained in Qiskit Metal using the conformal mapping results. Subsequently, eigenmode simulations were performed to extract the resonant frequencies. Five quarter-wave resonators were included in the design, targeting five resonances within the 4 to 8 GHz band. The complete design is shown in Fig. 4.12. Figure 4.13 shows the electric field distribution at the surface of one of the resonators, while Fig. 4.14 reports the convergence of the extracted resonant frequencies.

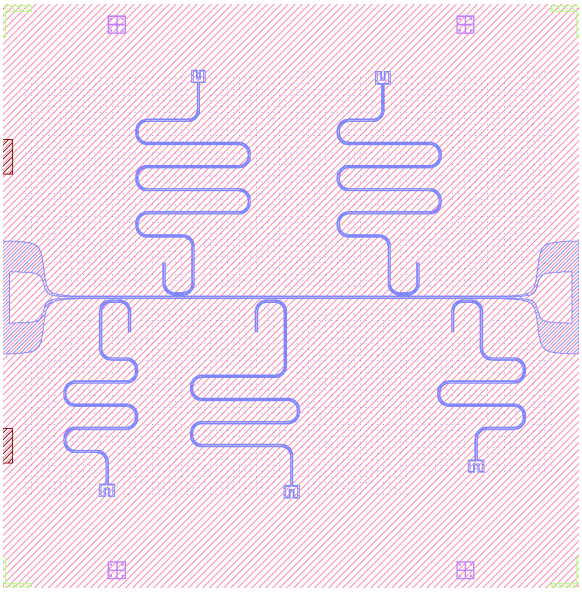

Figure 4.12: Design of five CPW resonators coupled to the same feedline in a hanging-resonator configuration.

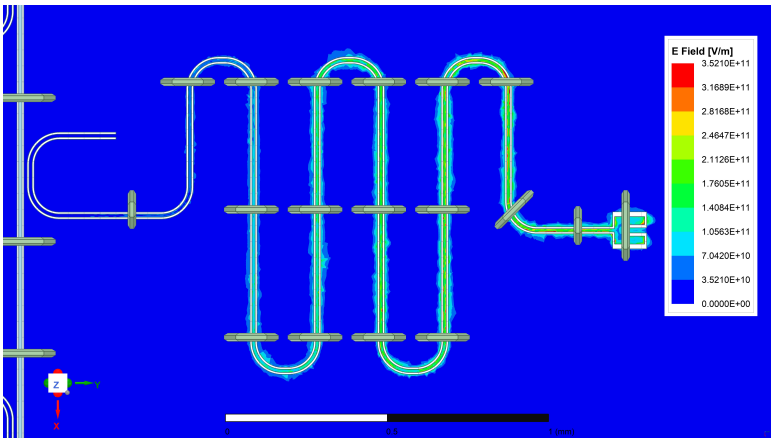

Figure 4.13: Eigenmode simulation of one of the quarter-wave resonators showing the electric field distribution on the chip surface.

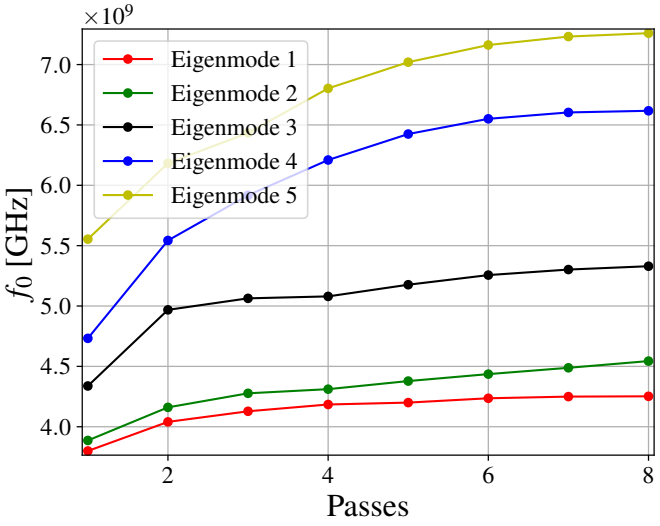

Figure 4.14: Convergence behavior of the eigenmode solver. Simulations were stopped when the relative frequency variation was below 5%.

These simulations were repeated for all five resonators. An additional step in the characterization of the resonators is the analysis of the response of the scattering parameters. To this end, the design was exported once again to HFSS, this time employing a driven-mode simulation rather than an eigenmode analysis. An interpolating frequency sweep of 10001 points in the 4 to 8 GHz range was performed. A maximum mesh length of 50 μm was manually assigned to the surfaces of the resonators to avoid mesh artifacts. The resulting transmission spectra S_{21} are shown in Fig. 4.15. These data are used to extract the coupling factor, since the preliminary estimates obtained from the analytical tool mentioned earlier do not take into account the curved part of the resonators, which has a non-negligible contribution to the coupling factor. We obtained $Q_C \sim 10^5$ for all the resonators, so an internal quality factor of around 10^6 can be accurately estimated with the circle fit technique.

4.6.1 Fabrication of the microwave devices

The microwave devices were fabricated with the same process described in Chapter 3 for the nanobridge junctions. The silicon substrates were cleaned in acetone and IPA, the native oxide was removed by a dip in HF, and the multilayer stacks of Sample A (NbN based) and Sample B (TiN based) were deposited by dc magnetron sputtering without breaking vacuum (Table 3.1). The patterns were defined by electron beam lithography in CSAR resist and transferred to the

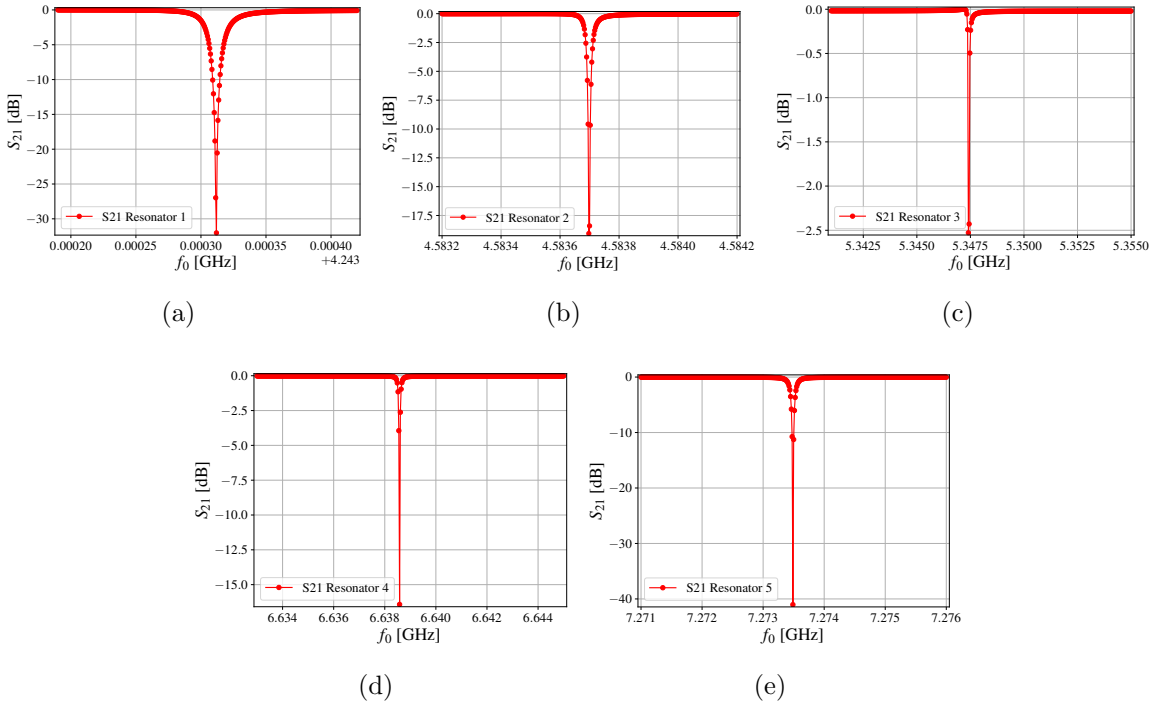

Figure 4.15: Simulated S_{21} of the five-resonator sample: (a) $f_0 = 4.24$ GHz, $Q_C \sim 1 \cdot 10^5$; (b) $f_0 = 4.58$ GHz, $Q_C \sim 1.15 \cdot 10^5$; (c) $f_0 = 5.34$ GHz, $Q_C \sim 1.37 \cdot 10^5$; (d) $f_0 = 6.639$ GHz, $Q_C \sim 0.55 \cdot 10^5$; (e) $f_0 = 7.27$ GHz, $Q_C \sim 0.6 \cdot 10^5$.

films with the $BCl_3/Cl_2/Ar$ ICP etching recipe described in Section 3.1.2. For the fixed-frequency resonators and the feedline, a single etching step through the full multilayer stack is sufficient, since no weak link is required. For the flux-tunable resonators, the two-step process of Chapter 3 was used: after the first etch defining the resonator, the feedline and the SQUID loop, a second lithography and etching step removes the top Nb/Al/Nb layers above the nanobridges, forming the variable thickness junctions of the SQUID.

4.6.2 Package for resonator samples

The design of the sample box and printed circuit board (PCB) is a critical aspect of microwave measurements, particularly for superconducting circuits. The wrong package dimensions can introduce spurious resonant modes in the same frequency range as the on-chip resonators, potentially masking the measured response or, in the case of qubits, providing an additional and unwanted relaxation channel. For this reason, the dimensions of the three-dimensional (3D) package must be carefully chosen such that its modes lie above the operating frequency range of the device. For

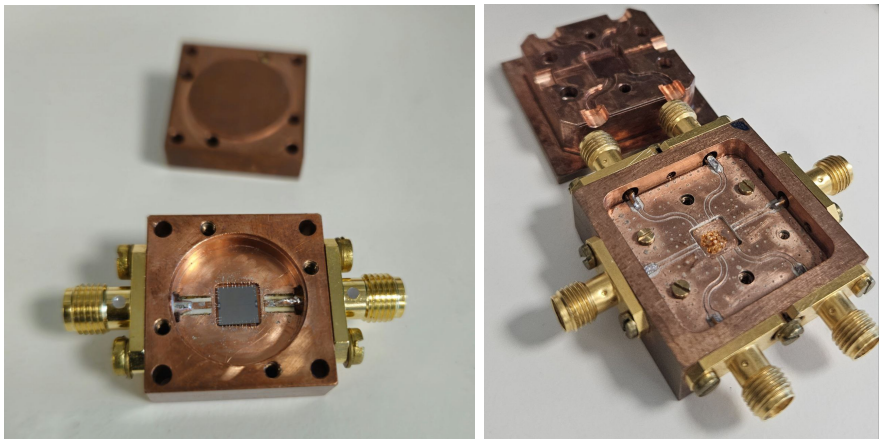

(a) (b)

Figure 4.16: (a) Package used for fixed-frequency resonators (diameter of internal cavity: 1.5 cm). (b) Package used for flux-tunable resonators ($3 \times 3 \times 2$ cm^3).

an ideal rectangular metallic cavity with dimensions $a \times b \times d$, the resonant frequencies are given by [129]

$$f_{mnp} = \frac{c}{2}\sqrt{\left(\frac{m}{a}\right)^2 + \left(\frac{n}{b}\right)^2 + \left(\frac{p}{d}\right)^2} \tag{4.6.1}$$

where m, n, p are non-negative integers and c is the speed of light. This expression provides a first estimate of the cavity mode spectrum and guides the choice of the package dimensions. Figure 4.16 shows the sample boxes used in our experiments. The package shown in Fig. 4.16(a) is used for fixed-frequency resonators, while the one in Fig. 4.16(b) is used for flux-tunable resonators. Both enclosures are designed such that all cavity resonances lie above 10 GHz, well separated from the operating frequencies of the devices. Although the latter enclosure has overall dimensions of $3 \times 3 \times 2$ cm^3, which would place the lowest package mode around 7 GHz, its lid is designed to make contact with the ground plane, reducing the effective package volume above the sample and shifting the resonant modes to higher frequencies.

In addition to the available sample boxes, a custom 3D package was designed as shown in Fig. 4.18(c). The geometry was modelled in HFSS and its eigenmodes were simulated with the lid closed. The lid incorporates metallic pillars surrounding the sample region, effectively creating a local Faraday cage. This design strongly suppresses low-frequency cavity modes, even though the overall dimensions of the enclosure are larger than those of the previous boxes. Due to time constraints, this custom package could not be employed for the measurements presented in this thesis; nevertheless, the design and simulation results are reported here as they represent a viable



(a) (b) (c)

Figure 4.17: RF connectors considered for the package design.

solution for future experiments. Figure 4.19 shows the first two simulated eigenmodes of the package.

We now consider the RF connectors used to connect the package to the external wiring. All connectors have a nominal impedance of 50 Ω; however, their geometry and the extent to which they protrude into the package introduce important differences. As shown in Fig. 4.17, connector (a) lacks dielectric material around the inner conductor, leading to a vacuum-filled section inside the package and a local impedance increase before the transition to the PCB. Connector (b) provides good impedance matching but is mechanically large and requires a significant amount of solder, which can adversely affect insertion losses. The SMA connector shown in Fig. 4.17(c) was selected for the custom package: its compact size and integrated dielectric facilitate soldering and help minimize insertion losses.

Finally, the PCB was designed in Altium Designer. A 12-port coplanar waveguide (CPW) layout was implemented with central conductor width $w = 0.2$ mm and gap $g = 0.13$ mm, giving a characteristic impedance of 50 Ω. Grounded shielding vias were added along the transmission lines to shield the lines from signals up to 10 GHz and to ensure robust grounding, following standard microwave design guidelines [129]. The PCB layout is shown in Fig. 4.18. The measured transmission and reflection parameters S_{21}, S_{11}, and S_{22} are reported in Fig. 4.20, confirming good impedance matching and low insertion losses across the frequency range of interest.

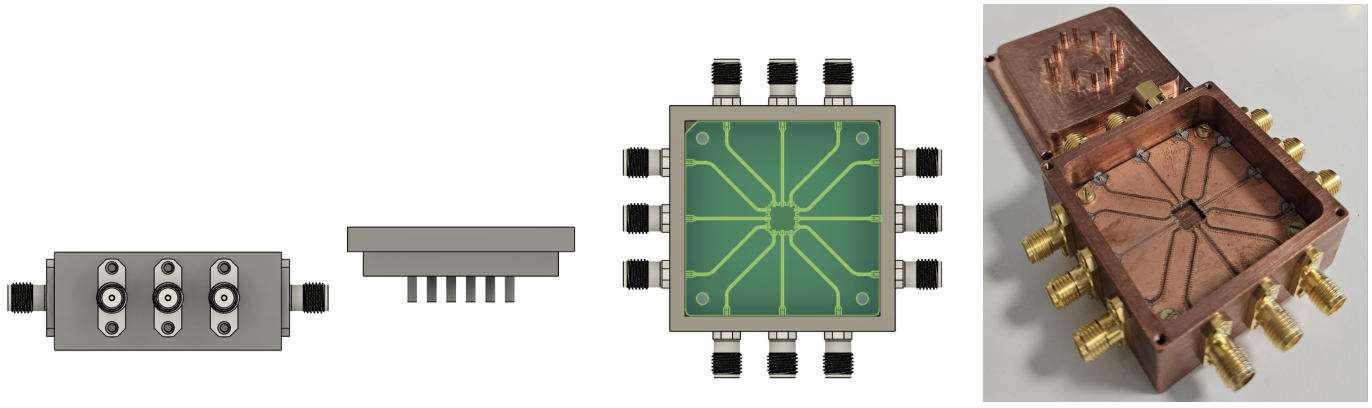

(a) (b) (c)

Figure 4.18: (a) Designed package, y-view. (b) Designed package, z-view. (c) Picture of the fabricated package ($4 \times 4 \times 2$ cm^3).

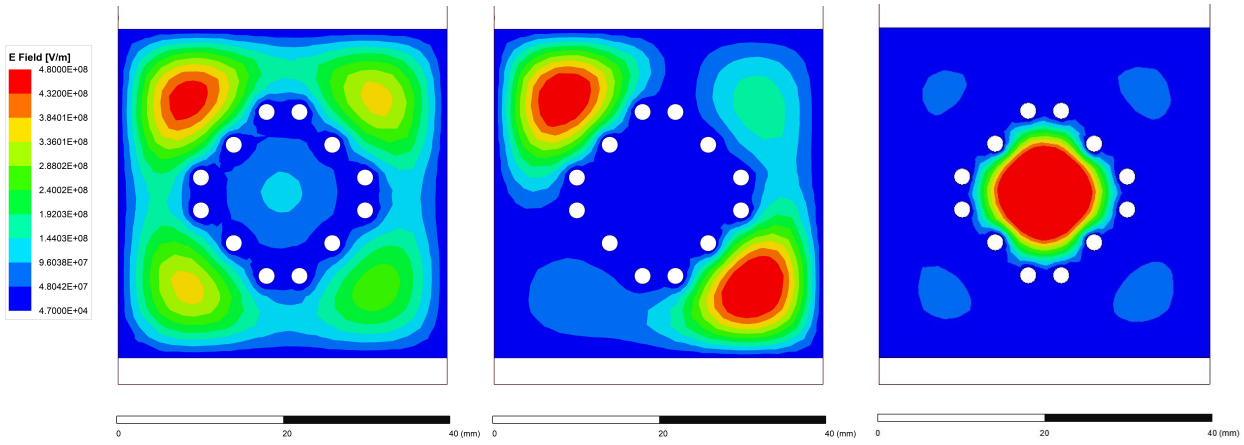

(a) (b) (c)

Figure 4.19: Simulated eigenmodes of the custom package: (a) first resonance $\sim$ 11 GHz, (b) second resonance $\sim$ 12 GHz, (c) fifth resonance $\sim$ 13 GHz.

4.7 Resonators: Device Characterization

4.7.1 Cryogenic microwave setup

The microwave characterisation of superconducting resonators is performed at millikelvin temperatures using a dilution refrigerator, in order to suppress thermal excitations and access the quantum regime of the device. Dilution refrigerators are the standard platform for continuous operation below 100 mK. A schematic of the cryogenic setup and temperature stages is shown in Fig. 4.21. The

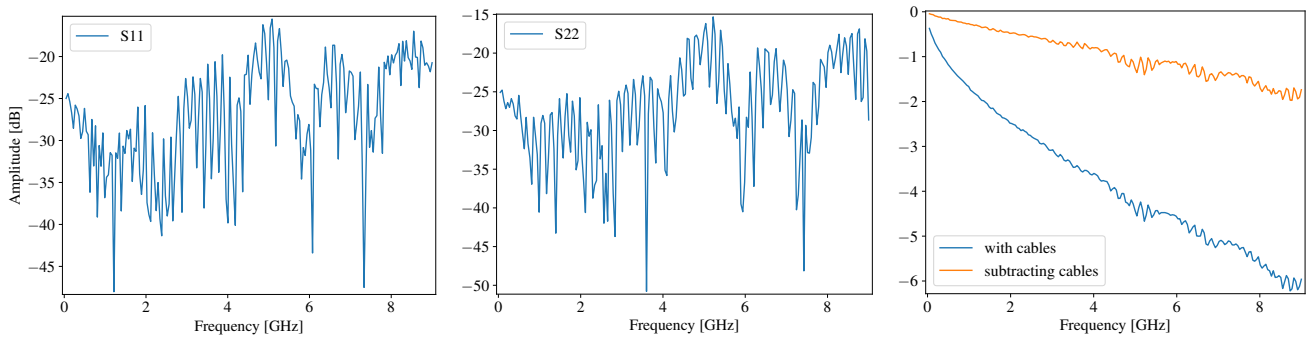

(a) (b) (c)

Figure 4.20: Measured scattering parameters of the PCB and package assembly: (a) S_{11}, (b) S_{22}, and (c) S_{21}.

samples are mounted on the coldest temperature stage of the cryostat (mixing chamber: 40 mK) and enclosed in a sample box to ensure both proper thermalisation and electromagnetic shielding from environmental noise. Electrical connection between the on-chip transmission line and the coaxial connectors of the sample box is achieved via aluminium wirebonds. Additional wirebonds are placed between the ground plane of the chip and the sample holder to minimise parasitic modes, suppress cross-talk, and ensure a uniform ground potential across the device. The device under test is measured in transmission configuration. The input microwave line is attenuated by four 20 dB attenuators, as shown in Fig. 4.21(b): one at room temperature, outside the cryostat, and one at each of the 77 K, 4 K and 150 mK stages. This attenuation scheme has multiple reasons. First, it reduces the room-temperature microwave signal generated by the vector network analyser (VNA) down to the single photon power regime at the resonator. Second, it provides thermal anchoring of the coaxial cables at each temperature stage, limiting heat flow towards the mixing chamber. Finally, it suppresses the propagation of noise from higher temperature stages into the device. An attenuator thermalised at a temperature T_i reduces the incoming noise by its attenuation factor A_i and, at the same time, adds the thermal noise of its own stage. In terms of the average number of thermal photons at frequency f, the noise after the i-th attenuator is [145]

$$n_i = \frac{n_{i-1}}{A_i} + \left(1 - \frac{1}{A_i}\right) n_{\mathrm{BE}}(T_i, f), \qquad n_{\mathrm{BE}}(T, f) = \frac{1}{e^{hf/k_B T} - 1} \tag{4.7.1}$$

where $n_0 = n_{\mathrm{BE}}(300\ \mathrm{K}, f)$ is the noise generated at room temperature. With $A_i = 100$ (20 dB) at $T_i = 300$ K, 77 K, 4 K and 150 mK, Eq. (4.7.1) gives $n \approx 0.33$ thermal photons at 6 GHz (≈ 0.6 at 4 GHz and ≈ 0.2 at 8 GHz). This corresponds to an effective noise temperature

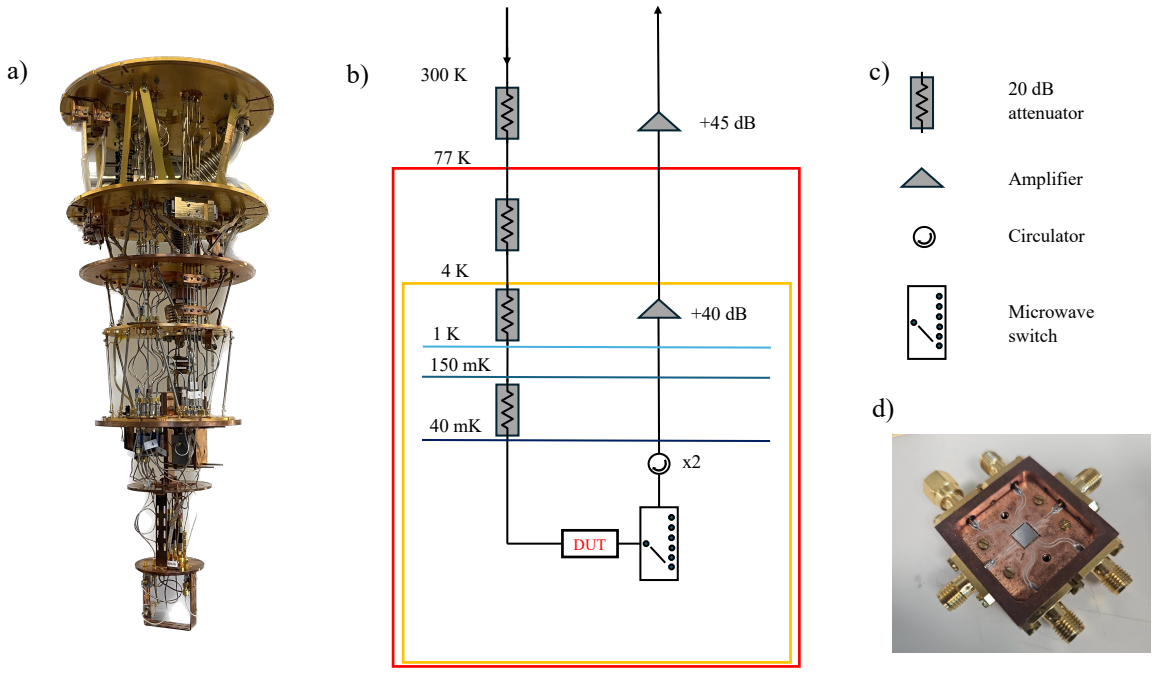

Figure 4.21: a) Photograph of the cryostat used for microwave measurements adapted from [24, 26]. b) Electrical wiring diagram of the cryogenic measurement setup, showing signal flow through attenuators, circulators, amplifiers, and temperature stages (300 K to 40 mK). c) Legend of symbols used in the schematic. d) Close-up view of the superconducting sample mounted in the copper sample box at the mixing chamber stage (40 mK).

$T_{\text{noise}} = hf/[k_B \ln(1 + 1/n)] \approx 0.2$ K over the 4 to 8 GHz band. Since the last attenuator is placed at the 150 mK stage, the noise reaching the sample is set mainly by the temperature of this stage, rather than by the 40 mK of the mixing chamber. This level of thermal noise would be detrimental for qubits, where it would cause a residual excited-state population and dephasing, and an additional attenuator at the mixing chamber would be required. For the resonators investigated in this thesis, however, its effect is limited. The thermal photons have energies $hf \ll 2\Delta$, so they cannot break Cooper pairs (for TiN, the material with the lowest gap, $2\Delta/h \approx 170$ GHz), and they only add a small background to the photon number in the resonator, which is relevant only at the lowest measurement powers. After transmission through the resonator, the output signal

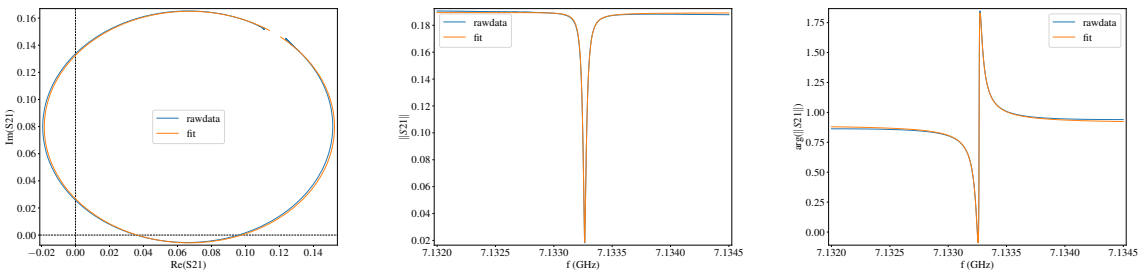

(a) (b) (c)

Figure 4.22: Circle fit performed for the TiN based resonator at an input power of −5 dB: (a) circle fit in the complex plane, (b) amplitude, (c) phase.

is routed through two cryogenic circulators before being amplified by a high-electron-mobility transistor (HEMT) amplifier mounted at the 4 K stage. The circulators direct the signal coming from the sample towards the amplifier, while preventing the noise emitted by the amplifier and the reflections in the output line from travelling back to the device. The amplified signal is further amplified by a room-temperature amplifier before being recorded at the second port of the VNA.

4.7.2 Transmission measurements

The VNA ports are connected to the input and output lines of the cryostat, allowing measurement of the complex transmission coefficient S_{21}. All resonators investigated in this work are capacitively coupled to a common feedline, resulting in notch-type resonances that appear as dips in the magnitude of S_{21}. Moreover, the same design was used for each material to allow an easier comparison, especially when studying the kinetic inductance. The measurements were performed with a Keysight E5071C vector network analyser, controlled through the open-source Python framework qkit [146], inside an Oxford Instruments Triton dilution refrigerator. The total nominal attenuation of the input line is 80 dB (20 dB at room temperature and 60 dB inside the cryostat, including the cables). A wide frequency sweep is initially performed to identify the operational bandwidth of the measurement and locate the resonator frequencies. Once the resonances are identified, narrower frequency windows are scanned with a high number of points to achieve sufficient resolution. This ensures that the resonance linewidths are well resolved, which is essential for the extraction of quality factors. Typical settings were 20001 points for the wide sweeps and 4001 to 5001 points over spans of a few MHz to about 20 MHz around each resonance, with an intermediate-frequency

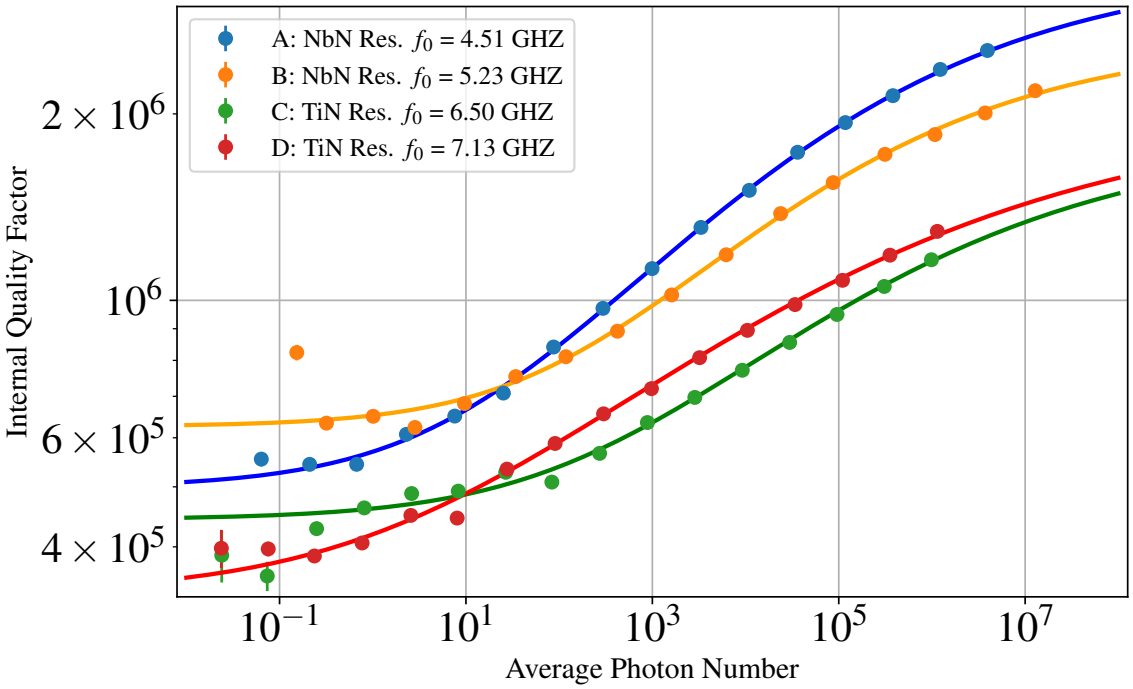

Figure 4.23: Comparison of internal quality factors (Q_i) for TiN and NbN based multilayer resonators. Both devices exhibit similarly high Q_i values, indicating that losses associated with different bottom nitride layers play a minor role; instead, dissipation is predominantly governed by the superconducting film, substrate, and interfaces, consistent with the use of high quality niobium resonators.

bandwidth (IFBW) of 200 Hz. For the power-dependent measurements, the VNA output power was swept from −80 to −5 dBm in steps of 5 dB, and the number of averaged traces was increased at low power to compensate for the lower signal-to-noise ratio, from 10 traces at the highest powers up to about 900 traces at −80 dBm. Before fitting, the linear phase contribution due to the electrical delay of the cables (of the order of 30 to 45 ns) was removed from the data.

4.7.3 Extraction of resonator parameters

The primary quantities of interest are the resonance frequency f_r, the internal quality factor Q_i, and the coupling quality factor Q_c. These parameters are extracted by fitting the complex transmission data using a circle-fitting procedure in the complex plane as explained in Section 4.5.1. An example is reported in Fig. 4.22.

4.7.4 Power-dependent measurements

In addition to single tone measurements, power-dependent studies are carried out to investigate the dominant loss mechanisms in the resonators. At millikelvin temperatures, dielectric losses arising from two-level systems (TLSs) typically dominate the internal dissipation. These defects interact with the resonator electric field and lead to increased loss at low photon numbers. The average photon number inside the resonator, $\langle n_{\mathrm{ph}} \rangle$, can be estimated from the power delivered to the chip as [26, 130]:

$$\langle n_{\mathrm{ph}} \rangle = \frac{P_{\mathrm{chip}}}{h f_r^2} \frac{Q_l^2}{\pi |Q_c|} \tag{4.7.2}$$

where

$$P_{\mathrm{chip}} = \frac{10^{(P_{\mathrm{VNA}} + P_{\mathrm{att}})/10}}{1000} \tag{4.7.3}$$

is the microwave power at the device plane. By varying the VNA output power and repeating the transmission measurements, the evolution of Q_i as a function of photon number can be extracted. At low excitation powers, significant averaging is required to overcome measurement noise due to strong attenuation. As the number of photons increases, the TLSs become saturated, leading to a reduction in the dielectric loss and a corresponding increase in Q_i. Since quasiparticle losses can be neglected ($T \ll T_C$) and no magnetic flux is applied, the dependence of the internal quality factor on photon number can be modelled as [26, 147]

$$\frac{1}{Q_i} = \frac{1}{Q_{\mathrm{TLS}}} \frac{\tanh\left(\frac{h f_r}{2 k_B T}\right)}{\left[1 + \left(\langle n_{\mathrm{ph}} \rangle / n_c\right)^{\beta}\right]^{1/2}} + \frac{1}{Q_0} \tag{4.7.4}$$

where Q_{TLS} quantifies losses due to TLS, Q_0 represents residual TLS-independent losses, n_c is the critical photon number for TLS saturation which depends also on the geometry of the resonator, and β characterizes the extent of interactions. Figure 4.23 shows the measured internal quality factor Q_i as a function of photon number, together with fits obtained using the TLS model. The extracted parameters are summarised in Table 4.2. Both multilayer samples exhibit high internal quality factors, exceeding 10^5 in the low-photon regime and reaching values above 10^6 at high powers. These values are consistent with state of the art performance reported for sputtered coplanar waveguide superconducting resonators [90, 101]. The extracted values of $\tan(1/Q_{\mathrm{TLS}}) \equiv \tan(\delta_{\mathrm{eff}})$ are of order 10^{-6}, indicating weak TLS-induced dissipation. This suggests that losses associated with the use of different bottom nitride layers play a minor role, and that the overall

dissipation is dominated by the superconducting film, substrate and interfaces, consistent with the use of high quality niobium based multilayers. Furthermore, the fitted values of β fall in the range 0.3 to 0.45, in good agreement with previously reported results [90, 101]. The systematic deviation from the ideal value $\beta = 0.5$ indicates the presence of interacting TLS as discussed in Refs. [148, 149].

Device	$\tan(1/Q_{\mathrm{TLS}})$	Q_0	β
A	$(1.73 \pm 0.13) \times 10^{-6}$	$(3.46 \pm 0.16) \times 10^{6}$	0.43 ± 0.02
B	$(1.23 \pm 0.14) \times 10^{-6}$	$(2.67 \pm 0.17) \times 10^{6}$	0.45 ± 0.03
C	$(1.73 \pm 0.27) \times 10^{-6}$	$(1.85 \pm 0.56) \times 10^{6}$	0.40 ± 0.08
D	$(2.51 \pm 0.32) \times 10^{-6}$	$(2.02 \pm 0.35) \times 10^{6}$	0.33 ± 0.04

Table 4.2: TLS model fit parameters extracted for devices A to D. Q_{TLS} quantifies losses due to two-level systems, Q_0 represents residual power-independent losses, β characterises the interaction strength between the TLS ensemble and the resonator field.

4.7.5 Measured Kinetic inductance

The resonant frequencies were systematically shifted, reflecting different kinetic inductances in the samples. By comparing the experimentally measured resonance frequencies with electromagnetic simulations of ideal perfect-electric-conductor (PEC) resonators, we extracted the additional kinetic inductance contribution, L_k, associated with each multilayer stack, as reported in Fig. 4.24. Using the parameters extracted from the resistivity measurements, simulations predict that the kinetic inductance of the multilayers should remain essentially unchanged. This is because the high resistivity of the nitride layer contributes negligibly to the total inductance, and although a reduction in the Nb energy gap could in principle increase L_k, the condition $\gamma \ll 1$ ensures that no significant suppression occurs in the Nb layer. Therefore, these simulations cannot fully account for the experimentally observed variation, indicating that additional effects must be involved. A plausible explanation is the presence of small but systematic differences in film thickness between the samples. Electromagnetic simulations in HFSS yield a geometrical inductance of approximately 423 nH/m, meaning that the observed $\sim 2\%$ difference between the two devices is too small to resolve contributions from variations in the superconducting energy gap. Future exper-

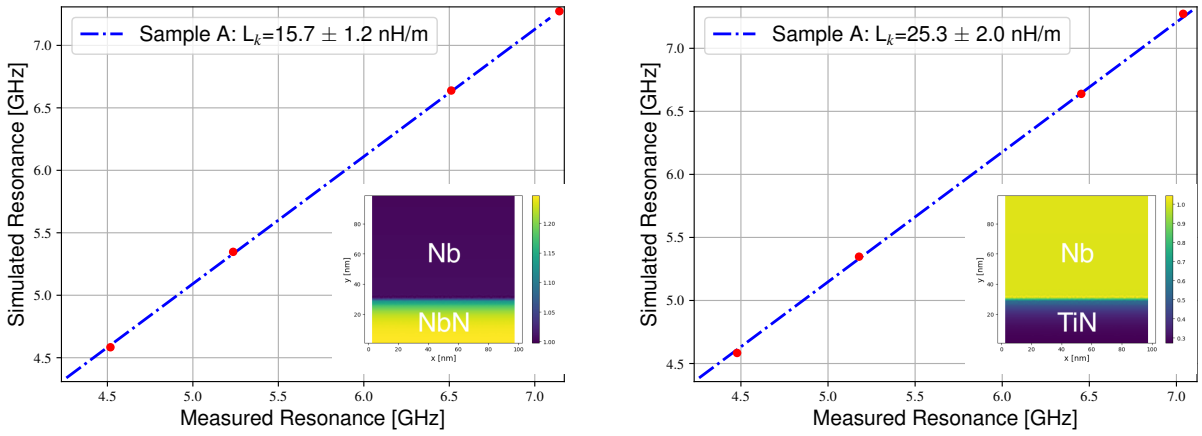

(a) (NbN based)

(b) (TiN based)

Figure 4.24: Kinetic inductance extracted from resonance shifts with respect to a perfect-electric-conductor (PEC) reference resonator for (a) Sample A and (b) Sample B.

iments should focus on materials in which the kinetic inductance is at least comparable to the geometrical inductance, allowing a clearer analysis of proximity-induced effects.

4.8 Flux-tunable resonators

Flux-tunable superconducting resonators provide a versatile platform for control of the resonance frequency through magnetic flux biasing. In these devices, tunability is typically achieved by embedding a superconducting quantum interference device (SQUID) into the resonator, thereby introducing a nonlinear and flux-dependent inductive element. By varying the magnetic flux threading the SQUID loop, the effective inductance of the resonator can be continuously tuned, enabling controlled frequency shifts over a wide range. Such resonators are widely employed in circuit quantum electrodynamics experiments, parametric amplifiers, and qubit readout schemes, where dynamic frequency control is essential [53, 54, 107]. The flux-tunable resonators studied here are quarter-wavelength CPW resonators, capacitively coupled to the feedline at one end and shorted to ground at the other end through a dc SQUID. The SQUID has the same design as the dc SQUIDs discussed in Chapter 3, with two variable thickness nanobridges in a loop of approximately $4 \times 4\ \mu\text{m}^2$, and the magnetic flux is applied through an on-chip flux line placed next to the loop. The resonators were designed for frequencies of 5.62 GHz and 7.77 GHz. At the shorted end of a $\lambda/4$ resonator the current is maximal, so the SQUID acts as a small, flux-dependent inductance

in series with the line. For a symmetric SQUID with negligible loop inductance this inductance is $L_S(\Phi) = L_J/(2|\cos(\pi\Phi/\Phi_0)|)$, with $L_J = \Phi_0/(2\pi I_c)$ the Josephson inductance of a single junction, and for $L_S \ll L_r$ the resonance frequency becomes [54]

$$f(\Phi) \simeq \frac{f_0}{1 + L_S(\Phi)/L_r} \tag{4.8.1}$$

where f_0 is the frequency without the SQUID and $L_r = L_l\ell$ is the total inductance of the resonator line, with L_l the inductance per unit length and ℓ the resonator length. The tuning range is therefore set by the ratio L_S/L_r. As an estimate, for the 5.62 GHz resonator, $\ell = v_p/(4f_0) \approx 5.3$ mm with $v_p = c/\sqrt{\epsilon_{\text{eff}}}$ and $\epsilon_{\text{eff}} = (1+\epsilon_r)/2 \approx 6.35$, and with $L_l \approx 423$ nH/m from the HFSS simulations we obtain $L_r \approx 2.2$ nH. For junction critical currents of the order of 100 μA, $L_J \approx 3.3$ pH and $L_S(0) \approx 1.6$ pH, so that the frequency shift at zero flux is $f_0 L_S/L_r \approx 4$ MHz. We characterized flux-tunable resonators fabricated using the same materials as those discussed in the previous section. For both samples, we extracted a screening parameter $\beta_L > 1.5$, indicating a regime of strong inductive screening, see Fig. 4.25. This behavior is most likely due to the relatively large critical current of the Josephson junctions, which we estimate to be on the order of $I_c \sim 100$ μA. The larger β_L values observed in these devices compared to the SQUIDs discussed earlier are likely attributable to differences in the effective junction dimensions. In particular, the nanobridges in the flux-tunable resonators are oriented along the x-axis, whereas those used previously were aligned along the y-axis. As shown in Fig. 4.26, this change in orientation coincides with a significant distortion introduced by the electron-beam lithography tool, leading to a systematic increase in the junction cross section and, consequently, in the critical current.

4.9 Conclusions

In this chapter, we have presented a comprehensive study of superconducting microwave circuits, addressing both device design and material properties. We demonstrated the design of three-dimensional sample boxes and printed circuit boards, carefully optimizing their geometry to suppress spurious cavity modes and ensure reliable microwave measurements, with particular attention paid to the choice and integration of coaxial connectors. The resonators were designed using conformal mapping techniques and full-wave electromagnetic simulations in HFSS to achieve the target resonance frequencies and 50 Ω impedance matching. Both TiN and NbN multilayer films were employed, yielding resonators with high internal quality factors. Despite these encouraging

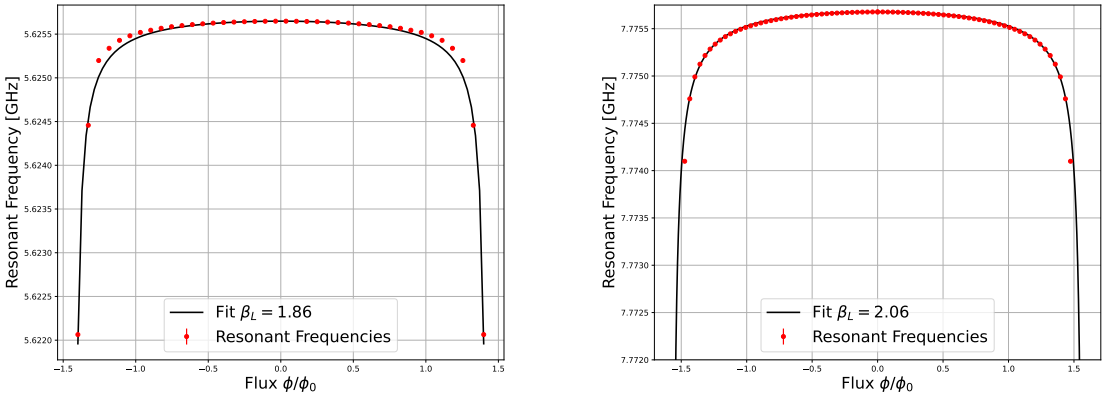

(a) Sample A (NbN based)

(b) Sample B (TiN based)

Figure 4.25: Measured and fitted resonance frequency of flux-tunable superconducting resonators fabricated with TiN and NbN, demonstrating continuous frequency tuning via magnetic flux biasing. The large extracted screening parameter, $\beta_L > 1.5$, indicates strong inductive screening due to the relatively high critical current of the nanobridge SQUIDs ($I_c \sim 100\ \mu$A).

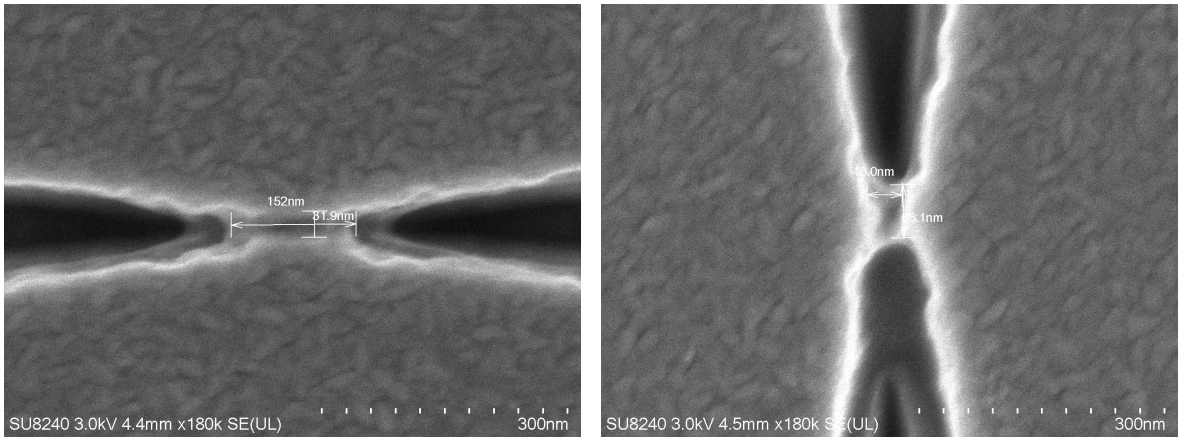

(a) x-oriented nanobridges (flux-tunable resonator)

(b) y-oriented nanobridges (dc SQUID)

Figure 4.26: SEM images of (a) the x-oriented nanobridges forming the SQUID in the flux-tunable resonator (dimensions: 152×32 nm^2) and (b) y-oriented nanobridges (dimensions: 65×43 nm^2). The electron-beam lithography distortion along the x-axis leads to a larger effective junction area and increased critical current. The images were taken on twin devices fabricated together with the measured ones, which were not imaged by SEM before the measurements.

results, the systematic shifts observed in the resonant frequencies could not be accounted for by

Usadel equation based models using parameters extracted from resistivity measurements. This indicates that additional effects, most plausibly small but systematic differences in film thickness, play a dominant role in determining the effective kinetic inductance. Finally, we extended our investigation to flux-tunable superconducting resonators incorporating nanobridge based SQUIDs. These devices exhibited flux tunability on the order of a few megahertz, consistent with operation in a regime of strong inductive screening. The large screening parameter is attributed to fabrication-induced variations in the nanobridge geometry, highlighting the sensitivity of these devices to lithographic alignment and emphasizing the importance of precise junction definition in future designs.

The tuning range of only a few megahertz is consistent with the estimate of Eq. (4.8.1): with critical currents of about 100 μA, the SQUID inductance is less than 10^{-3} of the resonator inductance, and with $\beta_L > 1.5$ the SQUID inductance cannot diverge near half a flux quantum. A much larger tuning range is realistic, but it requires the SQUID inductance to become a significant fraction of L_r. For example, a tuning of about 10% requires $L_S \approx 0.1\, L_r \approx 0.2$ nH, which corresponds to junction critical currents of about 1 μA, two orders of magnitude lower than in the present devices. This would also bring the screening parameter well below one ($\beta_L \approx 0.01$ for the same loop), so that L_S could be tuned over its full range. Such critical currents can be obtained with the design freedom offered by the multilayer approach of this thesis: narrower or thinner weak links, more resistive nitride layers, and a better control of the orientation-dependent distortion of the electron beam lithography discussed above. Using arrays of SQUIDs instead of a single SQUID is a further option to increase L_S without reducing the critical current of each junction.

More generally, this work feeds into several future developments. First, the multilayer nanobridges and the numerical framework of Chapter 2 can be used to design nanobridge based qubits: the simulations predict that multilayer junctions partially restore the anharmonicity lost with non-sinusoidal CPRs, and the low critical currents required by fluxonium qubits can be reached with highly resistive weak links. Second, future resonator experiments on proximity effects should use materials in which the kinetic inductance is at least comparable to the geometric inductance, so that changes in the superconducting gap produce a measurable frequency shift. Finally, the custom sample package and the measurement setup developed here provide a starting point for qubit experiments, for which an additional attenuator at the mixing chamber stage will be needed to reduce the thermal noise on the input line.

Conclusions and Future work

In this thesis, we have investigated a broad range of superconducting devices, spanning nanobridge based Josephson junctions, multilayer superconducting films, and coplanar waveguide resonators. The work combined numerical modelling, device design, nanofabrication, and experimental characterization, with the aim of improving the numerical framework and studying the behavior of commonly used superconducting devices in the presence of multilayer stacks. The main results are summarised below, followed by the future work and the steps needed to carry it out.

Numerical modelling of nanobridge junctions

A substantial part of this work was devoted to the development of a numerical model for three-dimensional nanobridge Josephson junctions. By employing finite element methods, the model overcomes the limitations of widely used one-dimensional analytical approaches and allows realistic device geometries, including rounded edges, and multilayer material stacks to be treated without restrictive assumptions. The model enables the calculation of key junction parameters, including the critical current and the full current phase relation (CPR), which are essential for the integration of nanobridge junctions into larger superconducting circuits such as SQUIDs, qubits, and SFQ-based architectures.

The model was validated in three steps: it reproduces the analytical KO-1 result in the short junction limit, it agrees with previously published numerical results for two- and three-dimensional aluminium nanobridges, and it reproduces the experimental critical currents of aluminium nanobridges reported in the literature, with deviations of about 3% for variable thickness bridges when a realistic coherence length is used. When the simulated CPRs are used to compute qubit spectra, multilayer junctions partially recover the anharmonicity that is lost with the non-sinusoidal CPR of planar nanobridges.

Fabrication and DC characterization of nanobridges and SQUIDs

We developed a fabrication process for multilayer variable thickness nanobridges based only on electron beam lithography and chlorine based dry etching, without focused ion beam milling, and used it to fabricate Nb/NbN and Nb/TiN junctions and dc SQUIDs. The numerical model was tested against the measured critical currents of the nanobridges: for the NbN devices, the three-dimensional model gives a significantly better agreement than the KO-1 model ($\chi^2_{\text{norm}} = 0.96$ compared with 3.5).

For the SQUIDs, the experimental data were fitted using dc SQUID equations modified to incorporate the CPR obtained from our simulations. With this approach, the extracted screening parameter was closer to the value expected from the loop geometry than when the common sinusoidal CPR was used. The limited modulation depth of the SQUIDs was explained mainly by the asymmetry between the two junctions, rather than by the loop inductance. In SQUIDs based on NbN multilayers, deviations from a single valued CPR were observed, with the presence of higher harmonic contributions becoming evident. These results are consistent with the reduced coherence length of NbN, and they highlight the importance of accounting for non sinusoidal CPRs when modelling nanobridge based devices. The hysteresis observed in some junctions with large critical currents was attributed to heating in the resistive state.

Microwave resonators and flux-tunable resonators

Superconducting resonators fabricated from TiN and NbN based multilayer films were designed, fabricated, and characterized. The resonators were designed using conformal mapping techniques combined with high frequency simulations to obtain the desired resonance frequencies and impedance matching. The measured internal quality factors exceeded 10^5 at low photon numbers and reached values above 10^6 at high power, indicating low intrinsic losses and high fabrication quality.

Systematic shifts in the resonant frequencies were observed across devices with different bottom layers, reflecting variations in the kinetic inductance of the multilayer films. By comparing experimental data with full-wave simulations of ideal PEC resonators, the additional kinetic inductance

contribution was extracted. However, simulations based on parameters obtained from resistivity measurements and our model predicted nearly identical kinetic inductance values for the samples. This difference indicates that small variations in film thickness or device dimensions were probably present. Since the geometric inductance of the resonators largely exceeds the kinetic contribution, such variations are sufficient to mask more subtle effects related to changes in the superconducting energy gap.

The thesis also addressed practical aspects of microwave measurements through the design of three-dimensional sample boxes and printed circuit boards. Particular attention was given to cavity dimensions, PCB layout, and coaxial connector choice to suppress unwanted cavity modes and ensure reproducible measurements. Numerical simulations confirmed that cavity resonances were well separated from the operating frequency range of the devices.

Finally, flux-tunable superconducting resonators incorporating nanobridge-based SQUIDs were designed and characterized. The devices exhibited frequency tunability on the order of a few megahertz, consistent with operation in a regime of strong inductive screening and with a simple estimate based on the ratio between the SQUID inductance and the resonator inductance. The tunability is primarily limited by the relatively large critical currents of the nanobridge junctions, which are influenced by fabrication induced variations in junction geometry.

Overall, this work shows that nanobridge Josephson junctions and multilayer superconducting films provide a viable and flexible platform for superconducting circuits. At the same time, the results underline the need for better control over the etching process and the junction geometry.

Future work

The results of this thesis suggest several directions for future work. For each of them, we indicate how it could be achieved.

Better control of the junction dimensions. The spread in normal state resistance and critical current, and the asymmetry of the SQUIDs, are mainly due to variations in the second etching step. This can be improved by choosing material combinations with a higher etch selectivity, so that the etch stops reliably on the weak-link layer and the thickness of the bridge is set by the deposited film rather than by the etching time. Combining superconductors with similar resistivity would further improve the uniformity of the parameters. In addition, the distortion of the electron

beam lithography along one direction, which increased the critical current of the bridges in the flux-tunable resonators, can be avoided by aligning all junctions along the same axis or by calibrating the exposure on dedicated test structures.

SQUIDs with larger modulation depth. Since the modulation depth is limited mainly by the junction asymmetry, $\Delta I_c/I_{c,\max} \approx 1-\alpha$, the better dimensional control described above would directly increase the modulation of the SQUIDs. Asymmetric SQUIDs, in which one nanobridge is paired with a junction of much larger critical current, could also be used on purpose to measure the CPR of a single nanobridge directly [45]. This would allow the model to be tested on the full shape of the CPR, and not only on the critical current.

Flux-tunable resonators with a larger tuning range. A much larger tuning range is realistic, but it requires the SQUID inductance to become a significant fraction of the resonator inductance. For example, a tuning of about 10% requires critical currents of about 1 μA, two orders of magnitude lower than in the present devices, which would also bring the screening parameter well below one. This can be achieved with narrower or thinner weak links and with more resistive nitride layers, which the multilayer approach allows, or by replacing the single SQUID with an array of SQUIDs.

Nanobridge based qubits. Transmon and fluxonium qubits require critical currents of the order of 10 to 100 nA and below 50 nA, respectively, which can be reached with highly resistive weak links designed with the numerical model of Chapter 2. The next step is to fabricate capacitively shunted multilayer nanobridges and to measure their spectrum and coherence times. For these experiments, the measurement setup will need an additional attenuator at the mixing chamber stage, to reduce the thermal photons in the input line, and the custom sample package designed in this work, whose first box modes lie above 10 GHz, can be used.

Kinetic inductance and proximity effect in multilayer resonators. To separate the effect of the superconducting gap from that of small thickness variations, future resonator experiments should use materials in which the kinetic inductance is at least comparable to the geometric inductance, for example thin nitride films, and should measure the film thickness on the same chip as the resonators.

Extensions of the numerical model. The model can be extended in several ways: by including the vector potential in the Usadel equations, to describe the effect of magnetic fields and of the flux in SQUID loops; by coupling it to a heat equation, to describe the heating and hysteresis observed in junctions with large critical currents; and by moving to the non-equilibrium (Keldysh) formulation of the Usadel equations, to describe junctions in the resistive state and under microwave drive.

These developments will be essential for the reliable integration of nanobridge based devices into scalable superconducting quantum technologies.

Acknowledgements

First and foremost, I would like to thank my supervisor, Prof. Martin Weides, for giving me the opportunity to undertake this PhD in his group, for his guidance and scientific insight throughout these years, and for the freedom and trust he gave me to pursue my own ideas, from the numerical modelling of nanobridge junctions to their fabrication and measurement. I am also grateful to my second supervisor, Prof. Vihar Georgiev, for his support and advice during the course of this work.

I thank my examiners for their careful reading of this thesis, for the stimulating discussion during the viva, and for their comments and suggestions, which have improved the final version of this work.

The experimental part of this thesis would not have been possible without the help of many people and friends in the group. I am grateful to Jon and Chris for teaching me the nanofabrication processes, for sharing their experience and recipes, and for their patience in answering my many questions. A special thanks goes to Susan, with whom I shared a large part of the fabrication work: in the early stages of this project we developed and carried out the first fabrication runs together, and her collaboration, help and good company made the many hours spent in the cleanroom both more productive and more enjoyable.

I would like to thank João for his invaluable help with the dilution refrigerator, the microwave measurement setup and the experimental instrumentation, and for always being available to discuss and solve the practical problems that arise in low-temperature experiments.

I also thank the staff of the James Watt Nanofabrication Centre (JWNC) for their technical support, and all the members of Prof. Weides' group, past and present, for the discussions, the help and the friendly working environment.

I would also like to thank my family and my friends for their constant support, patience and encouragement throughout these years, and for always reminding me of what really matters outside the laboratory.

Finally, my deepest gratitude goes to my father, who passed away during my studies. He always supported me and encouraged me to keep going, even in the moments when I wanted to give up. This thesis is dedicated to his memory.

Bibliography

[1] Giuseppe Colletta et al. *Gap Engineered Superconducting Multilayer Nanobridge Josephson Junctions*. 2026. arXiv: 2603.20757 [cond-mat.supr-con]. URL: https://arxiv.org/abs/2603.20757.

[2] Giuseppe Colletta et al. "Modeling realistic multilayer devices for superconducting quantum electronic circuits". In: *Applied Physics Letters* 126.14 (Apr. 2025), p. 142601. ISSN: 0003-6951. DOI: 10.1063/5.0251879. eprint: https://pubs.aip.org/aip/apl/article-pdf/doi/10.1063/5.0251879/20478322/142601_1_5.0251879.pdf. URL: https://doi.org/10.1063/5.0251879.

[3] Fiheon Imroze et al. "Hysteresis-Induced Neuromorphic Behavior in 180nm Bulk PMOS Devices at 3K". In: *2025 IEEE 37th International Conference on Microelectronic Test Structures (ICMTS)*. 2025, pp. 1–4. DOI: 10.1109/ICMTS63811.2025.11068927.

[4] Boris Chesca, Reinhold Kleiner, and Dieter Koelle. "SQUID Theory". In: *The SQUID Handbook, Vol. I: Fundamentals and Technology of SQUIDs and SQUID Systems*. Ed. by John Clarke and Alex I. Braginski. Weinheim: Wiley-VCH, 2004. Chap. 2, pp. 29–92. ISBN: 9783527603640. DOI: 10.1002/3527603646.ch2. URL: https://doi.org/10.1002/3527603646.ch2.

[5] K.K. Likharev and V.K. Semenov. "RSFQ logic/memory family: a new Josephson-junction technology for sub-terahertz-clock-frequency digital systems". In: *IEEE Transactions on Applied Superconductivity* 1.1 (1991), pp. 3–28. DOI: 10.1109/77.80745.

[6] Morten Kjaergaard et al. "Superconducting Qubits: Current State of Play". In: *Annual Review of Condensed Matter Physics* 11.1 (2020), pp. 369–395. DOI: 10.1146/annurev-conmatphys-031119-050605. URL: https://doi.org/10.1146/annurev-conmatphys-031119-050605.

[7] K. K. Likharev. "Superconducting weak links". In: *Rev. Mod. Phys.* 51 (1 Jan. 1979), pp. 101–159. DOI: 10.1103/RevModPhys.51.101. URL: https://link.aps.org/doi/10.1103/RevModPhys.51.101.

[8] A. A. Golubov, M. Yu. Kupriyanov, and E. Il'ichev. "The current-phase relation in Josephson junctions". In: *Rev. Mod. Phys.* 76 (2 Apr. 2004), pp. 411–469. DOI: 10.1103/RevModPhys.76.411. URL: https://link.aps.org/doi/10.1103/RevModPhys.76.411.

[9] Michael Tinkham. *Introduction to Superconductivity*. 2nd ed. Dover Publications, June 2004. ISBN: 0486435032. URL: http://www.worldcat.org/isbn/0486435032.

[10] Thomas E. Roth, Ruichao Ma, and Weng C. Chew. "The Transmon Qubit for Electromagnetics Engineers: An introduction". In: *IEEE Antennas and Propagation Magazine* 65.2 (2023), pp. 8–20. DOI: 10.1109/MAP.2022.3176593.

[11] Frank Arute, Kunal Arya, Ryan Babbush, et al. In: *Nature* 574.7779 (Oct. 2019), pp. 505–510. ISSN: 1476-4687. DOI: 10.1038/s41586-019-1666-5. URL: https://doi.org/10.1038/s41586-019-1666-5.

[12] Shigeyuki Miyajima et al. "High-time-resolved 64-channel single-flux quantum-based address encoder integrated with a multi-pixel superconducting nanowire single-photon detector". In: *Opt. Express* 26.22 (Oct. 2018), pp. 29045–29054. DOI: 10.1364/OE.26.029045. URL: https://opg.optica.org/oe/abstract.cfm?URI=oe-26-22-29045.

[13] Jonathan J. Burnett et al. "Decoherence benchmarking of superconducting qubits". In: *npj Quantum Information* 5.1 (June 2019), p. 54. ISSN: 2056-6387. DOI: 10.1038/s41534-019-0168-5. URL: https://doi.org/10.1038/s41534-019-0168-5.

[14] Steffen Schlör et al. "Correlating Decoherence in Transmon Qubits: Low Frequency Noise by Single Fluctuators". In: *Phys. Rev. Lett.* 123 (19 Nov. 2019), p. 190502. DOI: 10.1103/PhysRevLett.123.190502. URL: https://link.aps.org/doi/10.1103/PhysRevLett.123.190502.

[15] M. Virginia P. Altoé et al. "Localization and Mitigation of Loss in Niobium Superconducting Circuits". In: *PRX Quantum* 3 (2 Apr. 2022), p. 020312. DOI: 10.1103/PRXQuantum.3.020312. URL: https://link.aps.org/doi/10.1103/PRXQuantum.3.020312.

[16] Jürgen Lisenfeld et al. "Electric field spectroscopy of material defects in transmon qubits". In: *npj Quantum Information* 5.1 (Nov. 2019), p. 105. ISSN: 2056-6387. DOI: 10.1038/s41534-019-0224-1. URL: https://doi.org/10.1038/s41534-019-0224-1.

[17] V Bosboom et al. “Selfconsistent 3D model of SN-N-NS Josephson junctions”. In: *Superconductor Science and Technology* 34.11 (Oct. 2021), p. 115022. DOI: 10.1088/1361-6668/ac2d79. URL: https://dx.doi.org/10.1088/1361-6668/ac2d79.

[18] R. Vijay et al. “Optimizing Anharmonicity in Nanoscale Weak Link Josephson Junction Oscillators”. In: *Phys. Rev. Lett.* 103 (8 Aug. 2009), p. 087003. DOI: 10.1103/PhysRevLett.103.087003. URL: https://link.aps.org/doi/10.1103/PhysRevLett.103.087003.

[19] Morten Amundsen and Jacob Linder. “General solution of 2D and 3D superconducting quasiclassical systems: coalescing vortices and nanoisland geometries”. In: *Scientific Reports* 6.1 (Mar. 2016), p. 22765. ISSN: 2045-2322. DOI: 10.1038/srep22765. URL: https://doi.org/10.1038/srep22765.

[20] HaiJie Li et al. “Experimental demonstrations of high-Q superconducting coplanar waveguide resonators”. In: *Chinese Science Bulletin* 58 (2013), pp. 2413–2417.

[21] Andreas Wallraff et al. “Strong coupling of a single photon to a superconducting qubit using circuit quantum electrodynamics”. In: *Nature* 431.7005 (2004), pp. 162–167.

[22] Antonio Barone and Gianfranco Paternò. *Physics and Applications of the Josephson Effect*. New York: John Wiley & Sons, 1982. DOI: 10.1002/352760278X. URL: https://doi.org/10.1002/352760278X.

[23] J. C. Gallop. *SQUIDs, the Josephson Effects and Superconducting Electronics*. Measurement Science and Technology. Bristol: Adam Hilger, 1991. ISBN: 0750300515.

[24] João N. F. Barbosa. “Single Flux Quantum Control Chip for Integrated Quantum Circuits”. Unpublished. PhD dissertation. University of Glasgow, 2021. DOI: 10.5525/gla.thesis.84771. URL: https://theses.gla.ac.uk/84771/.

[25] Jonathan A Collins. “Development of nanobridge based Josephson junction electronics for the readout of superconducting photon sensor arrays”. PhD thesis. University of Glasgow, 2021.

[26] Valentino Seferai. “Fabrication of On-Chip Quantum Circuits for Superconducting Quantum Technologies”. Unpublished. PhD dissertation. University of Glasgow, 2021. DOI: 10.5525/gla.thesis.84326. URL: https://theses.gla.ac.uk/84326/.

[27] J. Kroll. *Magnetic field compatible hybrid circuit quantum electrodynamics*. Delft University of Technology, 2019. DOI: https://doi.org/10.4233/uuid:d72c0db9-8463-4098-a796-457aaa88eaa3.

[28] J. Bardeen, L. N. Cooper, and J. R. Schrieffer. "Theory of Superconductivity". In: *Phys. Rev.* 108 (5 Dec. 1957), pp. 1175–1204. DOI: 10.1103/PhysRev.108.1175. URL: https://link.aps.org/doi/10.1103/PhysRev.108.1175.

[29] R. Meservey and P. M. Tedrow. "Measurements of the Kinetic Inductance of Superconducting Linear Structures". In: *Journal of Applied Physics* 40.5 (Apr. 1969), pp. 2028–2034. ISSN: 0021-8979. DOI: 10.1063/1.1657905. eprint: https://pubs.aip.org/aip/jap/article-pdf/40/5/2028/18350463/2028_1_online.pdf. URL: https://doi.org/10.1063/1.1657905.

[30] Leon N. Cooper. "Bound Electron Pairs in a Degenerate Fermi Gas". In: *Phys. Rev.* 104 (4 Nov. 1956), pp. 1189–1190. DOI: 10.1103/PhysRev.104.1189. URL: https://link.aps.org/doi/10.1103/PhysRev.104.1189.

[31] F. London and H. London. "The electromagnetic equations of the supraconductor". In: *Proceedings of the Royal Society of London. A. Mathematical and Physical Sciences* 149.866 (Mar. 1935), pp. 71–88. ISSN: 0080-4630. DOI: 10.1098/rspa.1935.0048. eprint: https://royalsocietypublishing.org/rspa/article-pdf/149/866/71/33451/rspa.1935.0048.pdf. URL: https://doi.org/10.1098/rspa.1935.0048.

[32] V. L. Ginzburg. "On the theory of superconductivity". In: *Il Nuovo Cimento (1955-1965)* 2.6 (Dec. 1955), pp. 1234–1250. ISSN: 1827-6121. DOI: 10.1007/BF02731579. URL: https://doi.org/10.1007/BF02731579.

[33] G.W. Webb, F. Marsiglio, and J.E. Hirsch. "Superconductivity in the elements, alloys and simple compounds". In: *Physica C: Superconductivity and its Applications* 514 (2015). Superconducting Materials: Conventional, Unconventional and Undetermined, pp. 17–27. ISSN: 0921-4534. DOI: https://doi.org/10.1016/j.physc.2015.02.037. URL: https://www.sciencedirect.com/science/article/pii/S0921453415000647.

[34] Ilya A. Stepanov et al. "Sputtered NbN films for ultrahigh performance superconducting nanowire single-photon detectors". In: *APL Materials* 12.2 (Feb. 2024), p. 021127. ISSN: 2166-532X. DOI: 10.1063/5.0188420. eprint: https://pubs.aip.org/aip/apm/article-

pdf/doi/10.1063/5.0188420/19696769/021127_1_5.0188420.pdf. URL: https://doi.org/10.1063/5.0188420.

[35] M. Trezza et al. "Superconducting properties of Nb thin films deposited on porous silicon templates". In: *Journal of Applied Physics* 104.8 (Oct. 2008), p. 083917. ISSN: 0021-8979. DOI: 10.1063/1.3006014. eprint: https://pubs.aip.org/aip/jap/article-pdf/doi/10.1063/1.3006014/10393963/083917_1_online.pdf. URL: https://doi.org/10.1063/1.3006014.

[36] P. G. de Gennes. "Boundary Effects in Superconductors". In: *Rev. Mod. Phys.* 36 (1 1964), pp. 225–237. DOI: 10.1103/RevModPhys.36.225. URL: https://doi.org/10.1103/RevModPhys.36.225.

[37] Leon N. Cooper. "Superconductivity in the Neighborhood of Metallic Contacts". In: *Phys. Rev. Lett.* 6 (12 1961), pp. 689–690. DOI: 10.1103/PhysRevLett.6.689. URL: https://doi.org/10.1103/PhysRevLett.6.689.

[38] M.Yu. Kurpianov and V. F. Lukichev. "Influence of boundary transparency on the critical current of dirty SS'S structures". In: *Soviet Physics - JETP (English Translation)* 67.6 (1988), pp. 1163–1168. ISSN: 0038-5646. URL: http://inis.iaea.org/search/search.aspx?orig_q=RN:22024754.

[39] B. D. Josephson. "Possible new effects in superconductive tunnelling". In: *Physics Letters* 1.7 (1962), pp. 251–253. DOI: 10.1016/0031-9163(62)91369-0. URL: https://doi.org/10.1016/0031-9163(62)91369-0.

[40] A F Andreev. "THERMAL CONDUCTIVITY OF THE INTERMEDIATE STATE OF SUPERCONDUCTORS". In: *Zh. Eksperim. i Teor. Fiz.* 46 (May 1964). URL: https://www.osti.gov/biblio/4071988.

[41] L. Bretheau et al. "Exciting Andreev pairs in a superconducting atomic contact". In: *Nature* 499.7458 (July 2013), pp. 312–315. ISSN: 1476-4687. DOI: 10.1038/nature12315. URL: http://dx.doi.org/10.1038/nature12315.

[42] Sidney Shapiro. "Josephson Currents in Superconducting Tunneling: The Effect of Microwaves and Other Observations". In: *Phys. Rev. Lett.* 11 (2 1963), pp. 80–82. DOI: 10.1103/PhysRevLett.11.80. URL: https://doi.org/10.1103/PhysRevLett.11.80.

[43] R. C. Jaklevic et al. “Quantum Interference Effects in Josephson Tunneling”. In: *Phys. Rev. Lett.* 12 (7 1964), pp. 159–160. DOI: 10.1103/PhysRevLett.12.159. URL: https://doi.org/10.1103/PhysRevLett.12.159.

[44] R. Kleiner et al. “Superconducting quantum interference devices: State of the art and applications”. In: *Proceedings of the IEEE* 92.10 (2004), pp. 1534–1548. DOI: 10.1109/JPROC.2004.833655. URL: https://doi.org/10.1109/JPROC.2004.833655.

[45] M. L. Della Rocca et al. “Measurement of the Current-Phase Relation of Superconducting Atomic Contacts”. In: *Phys. Rev. Lett.* 99 (12 Sept. 2007), p. 127005. DOI: 10.1103/PhysRevLett.99.127005. URL: https://link.aps.org/doi/10.1103/PhysRevLett.99.127005.

[46] Michael Mück, J. B. Kycia, and John Clarke. “Superconducting quantum interference device as a near-quantum-limited amplifier at 0.5 GHz”. In: *Applied Physics Letters* 78.7 (2001), pp. 967–969. DOI: 10.1063/1.1347384. URL: https://doi.org/10.1063/1.1347384.

[47] S. J. Asztalos et al. “SQUID-Based Microwave Cavity Search for Dark-Matter Axions”. In: *Phys. Rev. Lett.* 104 (4 2010), p. 041301. DOI: 10.1103/PhysRevLett.104.041301. URL: https://doi.org/10.1103/PhysRevLett.104.041301.

[48] Aico G. P. Troeman et al. “NanoSQUIDs Based on Niobium Constrictions”. In: *Nano Letters* 7.7 (2007), pp. 2152–2156. DOI: 10.1021/nl070870f. URL: https://doi.org/10.1021/nl070870f.

[49] L. Hao et al. “Measurement and noise performance of nano-superconducting-quantum-interference devices fabricated by focused ion beam”. In: *Applied Physics Letters* 92.19 (2008), p. 192507. DOI: 10.1063/1.2917580. URL: https://doi.org/10.1063/1.2917580.

[50] L. Hao et al. “Detection of single magnetic nanobead with a nano-superconducting quantum interference device”. In: *Applied Physics Letters* 98.9 (2011), p. 092504. DOI: 10.1063/1.3561743. URL: https://doi.org/10.1063/1.3561743.

[51] Carmine Granata and Antonio Vettoliere. “Nano Superconducting Quantum Interference device: A powerful tool for nanoscale investigations”. In: *Physics Reports* 614 (2016), pp. 1–69. DOI: 10.1016/j.physrep.2015.12.001. URL: https://doi.org/10.1016/j.physrep.2015.12.001.

[52] J. E. Mooij et al. “Josephson Persistent-Current Qubit”. In: *Science* 285.5430 (1999), pp. 1036–1039. DOI: 10.1126/science.285.5430.1036. URL: https://doi.org/10.1126/science.285.5430.1036.

[53] M. A. Castellanos-Beltran and K. W. Lehnert. “Widely tunable parametric amplifier based on a superconducting quantum interference device array resonator”. In: *Applied Physics Letters* 91.8 (2007), p. 083509. DOI: 10.1063/1.2773988. URL: https://doi.org/10.1063/1.2773988.

[54] M. Sandberg et al. “Tuning the field in a microwave resonator faster than the photon lifetime”. In: *Applied Physics Letters* 92.20 (2008), p. 203501. DOI: 10.1063/1.2929367. URL: https://doi.org/10.1063/1.2929367.

[55] Phillip Kaye, Raymond Laflamme, and Michele Mosca. *An Introduction to Quantum Computing*. USA: Oxford University Press, Inc., 2007. ISBN: 0198570007.

[56] Feng Bao et al. “Fluxonium: An Alternative Qubit Platform for High-Fidelity Operations”. In: *Phys. Rev. Lett.* 129 (1 June 2022), p. 010502. DOI: 10.1103/PhysRevLett.129.010502. URL: https://link.aps.org/doi/10.1103/PhysRevLett.129.010502.

[57] Guanyu Zhu et al. “Circuit QED with fluxonium qubits: Theory of the dispersive regime”. In: *Phys. Rev. B* 87 (2 Jan. 2013), p. 024510. DOI: 10.1103/PhysRevB.87.024510. URL: https://link.aps.org/doi/10.1103/PhysRevB.87.024510.

[58] Vladimir E. Manucharyan et al. “Fluxonium: Single Cooper-Pair Circuit Free of Charge Offsets”. In: *Science* 326.5949 (2009), pp. 113–116. DOI: 10.1126/science.1175552. eprint: https://www.science.org/doi/pdf/10.1126/science.1175552. URL: https://www.science.org/doi/abs/10.1126/science.1175552.

[59] Long B. Nguyen et al. “High-Coherence Fluxonium Qubit”. In: *Phys. Rev. X* 9 (4 Nov. 2019), p. 041041. DOI: 10.1103/PhysRevX.9.041041. URL: https://link.aps.org/doi/10.1103/PhysRevX.9.041041.

[60] Jonathan A. Collins, Calum S. Rose, and Alessandro Casaburi. “Superconducting Nb Nanobridges for Reduced Footprint and Efficient Next-Generation Electronics”. In: *IEEE Transactions on Applied Superconductivity* 33.1 (2023), pp. 1–8. DOI: 10.1109/TASC.2022.3218895.

[61] Mingzhao Liu and Charles T. Black. "Performance Analysis of Superconductor-constriction-Superconductor Transmon Qubits". In: *arXiv e-prints*, arXiv:2301.04276 (Jan. 2023), arXiv:2301.04276. DOI: 10.48550/arXiv.2301.04276. arXiv: 2301.04276 [cond-mat.supr-con].

[62] I. O. Kulik and A. N. Omel'yanchuk. "Contribution to the microscopic theory of the Josephson effect in superconducting bridges". In: *JETP Lett.* 21.4 (1975). [Pis'ma Zh. Eksp. Teor. Fiz. **21**, 216 (1975)], pp. 96–97.

[63] I. O. Kulik and A. N. Omel'yanchuk. "Properties of superconducting microbridges in the pure limit". In: *Sov. J. Low Temp. Phys.* 3 (1977). [Fiz. Nizk. Temp. **3**, 945 (1977)], pp. 459–461.

[64] I.I. Soloviev et al. "Miniaturization of Josephson Junctions for Digital Superconducting Circuits". In: *Phys. Rev. Appl.* 16 (4 Oct. 2021), p. 044060. DOI: 10.1103/PhysRevApplied.16.044060. URL: https://link.aps.org/doi/10.1103/PhysRevApplied.16.044060.

[65] Vsevolod Ruzhickiy et al. "Contribution of Processes in SN Electrodes to the Transport Properties of SN-N-NS Josephson Junctions". In: *Nanomaterials* 13.12 (2023). ISSN: 2079-4991. DOI: 10.3390/nano13121873. URL: https://www.mdpi.com/2079-4991/13/12/1873.

[66] Mark James Smith. *Quasi-classical theory of weakly anisotropic superconductors*. University of Birmingham, 2011.

[67] Gert Eilenberger. "Transformation of Gorkov's equation for type II superconductors into transport-like equations". In: *Zeitschrift für Physik A Hadrons and nuclei* 214.2 (Apr. 1968), pp. 195–213. ISSN: 0939-7922. DOI: 10.1007/BF01379803. URL: https://doi.org/10.1007/BF01379803.

[68] L P Gor'kov. "Energy spectrum of superconductors." In: *Sov. Phys. - JETP (Engl. Transl.)(United States)* 7:3 (Jan. 1958). URL: https://www.osti.gov/biblio/7264948.

[69] P. W. Anderson. "Theory of dirty superconductors". In: *Journal of Physics and Chemistry of Solids* 11.1 (1959), pp. 26–30. DOI: 10.1016/0022-3697(59)90036-8. URL: https://doi.org/10.1016/0022-3697(59)90036-8.

[70] A. A. Abrikosov and L. P. Gor'kov. "Contribution to the theory of superconducting alloys with paramagnetic impurities". In: *Sov. Phys. JETP* 12 (1961). [Zh. Eksp. Teor. Fiz. **39**, 1781 (1960)], pp. 1243–1253.

[71] M. Dasgupta. *An Introduction to Quantum Field Theory*. CreateSpace Independent Publishing Platform, 2014. ISBN: 9781502591760. URL: https://books.google.co.uk/books?id=%5C_Iy3jwEACAAJ.

[72] Klaus D. Usadel. "Generalized Diffusion Equation for Superconducting Alloys". In: *Phys. Rev. Lett.* 25 (8 Aug. 1970), pp. 507–509. DOI: 10.1103/PhysRevLett.25.507. URL: https://link.aps.org/doi/10.1103/PhysRevLett.25.507.

[73] J. N. Reddy. *Introduction to the Finite Element Method*. en. 4th Edition. New York: McGraw-Hill Education, 2019. ISBN: 9781259861901. URL: https://www.accessengineeringlibrary.com/content/book/9781259861901.

[74] Robert Cimrman, Vladimír Lukeš, and Eduard Rohan. "Multiscale finite element calculations in Python using SfePy". In: *Advances in Computational Mathematics* (2019). ISSN: 1572-9044. DOI: 10.1007/s10444-019-09666-0.

[75] ISAAK MAYERGOYZ. *Numerical Methods in Electromagnetism*. Academic Press, 2000. ISBN: 978-0-12-615760-4. DOI: https://doi.org/10.1016/B978-012615760-4/50000-6. URL: https://www.sciencedirect.com/science/article/pii/B9780126157604500006.

[76] Nicholas C. Henderson and Ravi Varadhan. "Damped Anderson Acceleration With Restarts and Monotonicity Control for Accelerating EM and EM-like Algorithms". In: *Journal of Computational and Graphical Statistics* 28.4 (2019), pp. 834–846. DOI: 10.1080/10618600.2019.1594835. eprint: https://doi.org/10.1080/10618600.2019.1594835. URL: https://doi.org/10.1080/10618600.2019.1594835.

[77] *Non Linear Diffusion Term*. http://sfepy.org/doc-devel/src/sfepy/terms/terms_diffusion.html#sfepy.terms.terms_diffusion.NonlinearDiffusionTerm. 2023.

[78] *Non Linear Volume Term*. http://sfepy.org/doc-devel/src/sfepy/terms/terms_volume.html#sfepy.terms.terms_volume.NonlinearVolumeForceTerm. 2023.

[79] R. Vijay et al. "Approaching ideal weak link behavior with three dimensional aluminum nanobridges". In: *Applied Physics Letters* 96.22 (2010), p. 223112. DOI: 10.1063/1.3443716. eprint: https://doi.org/10.1063/1.3443716. URL: https://doi.org/10.1063/1.3443716.

[80] M Tarasov et al. “Superconducting thin films and tunnel junctions based on aluminum”. In: *Phys. Solid State* 64 (2022), pp. 1352–1355.

[81] Peter Groszkowski and Jens Koch. “Scqubits: a Python package for superconducting qubits”. In: *Quantum* 5 (Nov. 2021), p. 583. ISSN: 2521-327X. DOI: 10.22331/q-2021-11-17-583. URL: https://doi.org/10.22331/q-2021-11-17-583.

[82] Zlatko K Minev et al. *Qiskit Metal: An Open-Source Framework for Quantum Device Design & Analysis*. 2021. DOI: 10.5281/zenodo.4618153. URL: https://doi.org/10.5281/zenodo.4618153.

[83] Pauli Virtanen, Ralf Gommers, Oliphant, et al. “SciPy 1.0: Fundamental Algorithms for Scientific Computing in Python”. In: *Nature Methods* 17 (2020), pp. 261–272. DOI: 10.1038/s41592-019-0686-2.

[84] Dennis Willsch et al. “Observation of Josephson harmonics in tunnel junctions”. In: *Nature Physics* (2024), pp. 1–7.

[85] M.Yu. Kupriyanov, K.K. Likharev, and V.F. Lukichev. “Influence of effective electron interaction on critical current of Josephson weak links”. In: *Physica B+C* 108.1 (1981), pp. 1001–1002. ISSN: 0378-4363. DOI: https://doi.org/10.1016/0378-4363(81)90804-4. URL: https://www.sciencedirect.com/science/article/pii/0378436381908044.

[86] Toshio Ogino et al. “Fabrication and Integration of Nanostructures on Si Surfaces”. In: *Accounts of Chemical Research* 32.5 (May 1999), pp. 447–454. ISSN: 0001-4842. DOI: 10.1021/ar970235o. URL: https://doi.org/10.1021/ar970235o.

[87] J. Van Damme et al. “Argon-Milling-Induced Decoherence Mechanisms in Superconducting Quantum Circuits”. In: *Phys. Rev. Appl.* 20 (1 July 2023), p. 014034. DOI: 10.1103/PhysRevApplied.20.014034. URL: https://link.aps.org/doi/10.1103/PhysRevApplied.20.014034.

[88] S. W. Pang et al. “Damage induced in Si by ion milling or reactive ion etching”. In: *Journal of Applied Physics* 54.6 (June 1983), pp. 3272–3277. ISSN: 0021-8979. DOI: 10.1063/1.332437. eprint: https://pubs.aip.org/aip/jap/article-pdf/54/6/3272/18401630/3272_1_online.pdf. URL: https://doi.org/10.1063/1.332437.

[89] Paniz Foshat et al. “Robust NbN on Si-SiGe hybrid superconducting-semiconducting microwave quantum circuit”. In: (Sept. 2025). arXiv: 2509.26363 [quant-ph].

[90] Paniz Foshat et al. “Quasiparticle Dynamics in Niobium Nitride Superconducting Microwave Resonators at Single-Photon Regime”. In: *IEEE Trans. Quantum Eng.* 6 (2025), pp. 1–8. DOI: 10.1109/TQE.2025.3616080. arXiv: 2506.17816 [quant-ph].

[91] “AR-P 6200 e-beam resist Data Sheet”. In: (). URL: :https://www.allresist.com/wp-content/uploads/sites/2/2020/03/AR-P6200_CSAR62english_Allresist_product-information.pdf.

[92] Matteo Altissimo. “E-beam lithography for micro-/nanofabrication”. In: *Biomicrofluidics* 4.2 (2010).

[93] Haifang Yang et al. “Comparative study of e-beam resist processes at different development temperature”. In: *Microelectronic Engineering* 84 (May 2007), pp. 1109–1112. DOI: 10.1016/j.mee.2007.01.053.

[94] Alongkorn Pimpin and Werayut Srituravanich. “Review on micro-and nanolithography techniques and their applications”. In: *Engineering journal* 16.1 (2012), pp. 37–56.

[95] Nam-Trung Nguyen. *Micromixers: fundamentals, design and fabrication*. William Andrew, 2011.

[96] J.I. Goldstein et al. *Scanning Electron Microscopy and X-Ray Microanalysis*. Springer New York, 2017. ISBN: 9781493966769. URL: https://books.google.it/books?id=D0I_DwAAQBAJ.

[97] HM Iftekhar Jaim et al. “Superconducting TiN films sputtered over a large range of substrate DC bias”. In: *IEEE Transactions on Applied Superconductivity* 25.3 (2014), pp. 1–5.

[98] Christine M. Zgrabik and Evelyn L. Hu. “Optimization of sputtered titanium nitride as a tunable metal for plasmonic applications”. In: *Opt. Mater. Express* 5.12 (Dec. 2015), pp. 2786–2797. DOI: 10.1364/OME.5.002786. URL: https://opg.optica.org/ome/abstract.cfm?URI=ome-5-12-2786.

[99] D. Andreone et al. “Properties of r.f. sputtered niobium thin films for metrological applications”. In: *Applied Superconductivity* 1.7 (1993). World Congress on Superconductivity, pp. 1333–1340. ISSN: 0964-1807. DOI: https://doi.org/10.1016/0964-1807(93)90440-D. URL: https://www.sciencedirect.com/science/article/pii/096418079390440D.

[100] Charles Kittel. *Introduction to Solid State Physics*. 8th ed. Wiley, 2004. ISBN: 9780471415268. URL: http://www.amazon.com/Introduction-Solid-Physics-Charles-Kittel/dp/047141526X/ref=dp_ob_title_bk.

[101] Shima Poorgholam-Khanjari et al. “Engineering high-Q superconducting tantalum microwave coplanar waveguide resonators for compact coherent quantum circuit”. In: *Scientific Reports* 15.1 (July 2025), p. 27113. ISSN: 2045-2322. DOI: 10.1038/s41598-025-11744-x. URL: https://doi.org/10.1038/s41598-025-11744-x.

[102] Mikhail Yu. Fominsky et al. “Fabrication of Superconducting Nb–AlN–NbN Tunnel Junctions Using Electron-Beam Lithography”. In: *Electronics* 10.23 (2021), p. 2944. DOI: 10.3390/electronics10232944. URL: https://doi.org/10.3390/electronics10232944.

[103] J. Tonotani et al. “Dry etching characteristics of TiN film using Ar/CHF3,Ar/Cl2, and Ar/BCl3 gas chemistries in an inductively coupled plasma”. In: *Journal of Vacuum Science Technology B: Microelectronics and Nanometer Structures Processing, Measurement, and Phenomena* 21.5 (Sept. 2003), pp. 2163–2168. ISSN: 1071-1023. DOI: 10.1116/1.1612517. eprint: https://pubs.aip.org/avs/jvb/article-pdf/21/5/2163/8206079/2163_1_online.pdf. URL: https://doi.org/10.1116/1.1612517.

[104] L. Hao, D. C. Cox, and J. C. Gallop. “Characteristics of focused ion beam nanoscale Josephson devices”. In: *Superconductor Science and Technology* 22.6 (2009), p. 064011. DOI: 10.1088/0953-2048/22/6/064011. URL: https://doi.org/10.1088/0953-2048/22/6/064011.

[105] David C. Cox, John C. Gallop, and Ling Hao. “Focused Ion Beam Processing of Superconducting Junctions and SQUID Based Devices”. In: *Nanofabrication* 1.1 (2014), pp. 53–64. DOI: 10.2478/nanofab-2014-0005. URL: https://doi.org/10.2478/nanofab-2014-0005.

[106] T. Godfrey et al. “Investigation of Dayem Bridge NanoSQUIDs Made by Xe Focused Ion Beam”. In: *IEEE Transactions on Applied Superconductivity* 28.7 (2018). DOI: 10.1109/TASC.2018.2854624. URL: https://doi.org/10.1109/TASC.2018.2854624.

[107] Jamie A. Potter et al. “Millikelvin Nb nanoSQUID-embedded tunable resonator fabricated with a neon focused-ion-beam”. In: *Applied Physics Letters* 126.1 (Jan. 2025), p. 012601. ISSN: 0003-6951. DOI: 10.1063/5.0230505. eprint: https://pubs.aip.org/aip/apl/article-pdf/doi/10.1063/5.0230505/20328797/012601_1_5.0230505.pdf. URL: https://doi.org/10.1063/5.0230505.

[108] W. Siemons et al. “Focused-ion-beam induced damage in thin films of complex oxide BiFeO3”. In: *APL Materials* 2.2 (Feb. 2014), p. 022109. ISSN: 2166-532X. DOI: 10.1063/1.4866051. eprint: https://pubs.aip.org/aip/apm/article-pdf/doi/10.1063/1.4866051/13763029/022109_1_online.pdf. URL: https://doi.org/10.1063/1.4866051.

[109] C.-H. Chen et al. “Combined method of focused ion beam milling and ion implantation techniques for the fabrication of high temperature superconductor Josephson junctions”. In: *Journal of Vacuum Science Technology B: Microelectronics and Nanometer Structures Processing, Measurement, and Phenomena* 16.5 (Sept. 1998), pp. 2898–2901. ISSN: 1071-1023. DOI: 10.1116/1.590291. eprint: https://pubs.aip.org/avs/jvb/article-pdf/16/5/2898/8202147/2898_1_online.pdf. URL: https://doi.org/10.1116/1.590291.

[110] Yariv Drezner et al. “Characterization of damage induced by FIB etch and tungsten deposition in high aspect ratio vias”. In: *Journal of Vacuum Science Technology B* 29.1 (Jan. 2011), p. 011026. ISSN: 2166-2746. DOI: 10.1116/1.3539204. eprint: https://pubs.aip.org/avs/jvb/article-pdf/doi/10.1116/1.3539204/15883316/011026_1_online.pdf. URL: https://doi.org/10.1116/1.3539204.

[111] O.W. Kennedy et al. “Tunable Nb Superconducting Resonator Based on a Constriction Nano-SQUID Fabricated with a Ne Focused Ion Beam”. In: *Phys. Rev. Appl.* 11 (1 Jan. 2019), p. 014006. DOI: 10.1103/PhysRevApplied.11.014006. URL: https://link.aps.org/doi/10.1103/PhysRevApplied.11.014006.

[112] L. F. Mattheiss. "Electronic Structure of Niobium and Tantalum". In: *Phys. Rev. B* 1 (2 Jan. 1970), pp. 373–380. DOI: 10.1103/PhysRevB.1.373. URL: https://link.aps.org/doi/10.1103/PhysRevB.1.373.

[113] S. P. Chockalingam et al. "Superconducting properties and Hall effect of epitaxial NbN thin films". In: *Phys. Rev. B* 77 (21 June 2008), p. 214503. DOI: 10.1103/PhysRevB.77.214503. URL: https://link.aps.org/doi/10.1103/PhysRevB.77.214503.

[114] J. S. Chawla, X. Y. Zhang, and D. Gall. "Effective electron mean free path in TiN(001)". In: *Journal of Applied Physics* 113.6 (Feb. 2013), p. 063704. ISSN: 0021-8979. DOI: 10.1063/1.4790136. eprint: https://pubs.aip.org/aip/jap/article-pdf/doi/10.1063/1.4790136/14703008/063704_1_online.pdf. URL: https://doi.org/10.1063/1.4790136.

[115] Jeremy Freixas et al. "Sputtered Titanium Nitride: A Bifunctional Material for Li-Ion Microbatteries". In: *Journal of The Electrochemical Society* 162.4 (Jan. 2015), A493. DOI: 10.1149/2.0051504jes. URL: https://dx.doi.org/10.1149/2.0051504jes.

[116] M. I. Faley and R. E. Dunin-Borkowski. "A Self-Flux-Biased NanoSQUID with Four NbN-TiN-NbN Nanobridge Josephson Junctions". In: *Electronics* 11.11 (2022). ISSN: 2079-9292. DOI: 10.3390/electronics11111704. URL: https://www.mdpi.com/2079-9292/11/11/1704.

[117] A. Greco, Q. Pichard, and F. Giazotto. "Josephson diode effect in monolithic dc-SQUIDs based on 3D Dayem nanobridges". In: *Applied Physics Letters* 123.9 (Aug. 2023), p. 092601. ISSN: 0003-6951. DOI: 10.1063/5.0165259. eprint: https://pubs.aip.org/aip/apl/article-pdf/doi/10.1063/5.0165259/18279784/092601_1_5.0165259.pdf. URL: https://doi.org/10.1063/5.0165259.

[118] Connor D Shelly et al. "Weak link nanobridges as single flux quantum elements". In: *Superconductor Science and Technology* 30.9 (Aug. 2017), p. 095013. DOI: 10.1088/1361-6668/aa80cd. URL: https://doi.org/10.1088/1361-6668/aa80cd.

[119] Kevin Uhl et al. “Niobium quantum interference microwave circuits with monolithic three-dimensional nanobridge junctions”. In: *Phys. Rev. Appl.* 21 (2 Feb. 2024), p. 024051. DOI: 10.1103/PhysRevApplied.21.024051. URL: https://link.aps.org/doi/10.1103/PhysRevApplied.21.024051.

[120] W. J. Skocpol, M. R. Beasley, and M. Tinkham. “Self-heating hotspots in superconducting thin-film microbridges”. In: *Journal of Applied Physics* 45.9 (1974), pp. 4054–4066. DOI: 10.1063/1.1663912. URL: https://doi.org/10.1063/1.1663912.

[121] Dibyendu Hazra et al. “Hysteresis in superconducting short weak links and μ-SQUIDs”. In: *Phys. Rev. B* 82 (18 2010), p. 184530. DOI: 10.1103/PhysRevB.82.184530. URL: https://doi.org/10.1103/PhysRevB.82.184530.

[122] A. Blois et al. “Heat propagation models for superconducting nanobridges at millikelvin temperatures”. In: *Superconductor Science and Technology* 30.1 (2017), p. 014003. DOI: 10.1088/0953-2048/30/1/014003. URL: https://doi.org/10.1088/0953-2048/30/1/014003.

[123] Michael I. Faley, Yuchen Liu, and Rafal E. Dunin-Borkowski. “Titanium Nitride as a New Prospective Material for NanoSQUIDs and Superconducting Nanobridge Electronics”. In: *Nanomaterials* 11.2 (2021), p. 466. DOI: 10.3390/nano11020466. URL: https://doi.org/10.3390/nano11020466.

[124] M I Faley et al. “Bulk nanomachining of cantilevers with Nb nanoSQUIDs based on nanobridge Josephson junctions”. In: *Superconductor Science and Technology* 34.3 (Feb. 2021), p. 035014. DOI: 10.1088/1361-6668/abda5c. URL: https://doi.org/10.1088/1361-6668/abda5c.

[125] Michael I. Faley, Yuchen Liu, and Rafal E. Dunin-Borkowski. “Titanium Nitride as a New Prospective Material for NanoSQUIDs and Superconducting Nanobridge Electronics”. In: *Nanomaterials* 11.2 (2021). ISSN: 2079-4991. DOI: 10.3390/nano11020466. URL: https://www.mdpi.com/2079-4991/11/2/466.

[126] Claudia D. Tesche and John Clarke. “dc SQUID: Noise and optimization”. In: *Journal of Low Temperature Physics* 29.3 (1977), pp. 301–331. DOI: 10.1007/BF00655097. URL: https://doi.org/10.1007/BF00655097.

[127] Ya. V. Fominov and D. S. Mikhailov. "Asymmetric higher-harmonic SQUID as a Josephson diode". In: *Phys. Rev. B* 106 (13 Oct. 2022), p. 134514. DOI: 10.1103/PhysRevB.106.134514. URL: https://link.aps.org/doi/10.1103/PhysRevB.106.134514.

[128] E M Levenson-Falk, N Antler, and I Siddiqi. "Dispersive nanoSQUID magnetometry". In: *Superconductor Science and Technology* 29.11 (Sept. 2016), p. 113003. DOI: 10.1088/0953-2048/29/11/113003. URL: https://doi.org/10.1088/0953-2048/29/11/113003.

[129] David M. Pozar. *Microwave engineering*. Includes bibliographical references and index. Fourth edition. Hoboken, NJ : Wiley, [2012] ©2012, 2012. URL: https://search.library.wisc.edu/catalog/9910153599402121.

[130] Paul G. Baity et al. "Circle fit optimization for resonator quality factor measurements: Point redistribution for maximal accuracy". In: *Phys. Rev. Res.* 6 (1 Mar. 2024), p. 013329. DOI: 10.1103/PhysRevResearch.6.013329. URL: https://link.aps.org/doi/10.1103/PhysRevResearch.6.013329.

[131] Jiansong Gao. *The Physics of Superconducting Microwave Resonators*. California Institute of Technology, 2008. DOI: 10.7907/RAT0-VM75. URL: https://resolver.caltech.edu/CaltechETD:etd-06092008-235549.

[132] Alexander Denis Stehli. "Analog quantum simulator of the multistate Landau-Zener model". PhD thesis. Karlsruher Institut für Technologie (KIT), 2021. 126 pp. DOI: 10.5445/IR/1000132804.

[133] S. Probst et al. "Efficient and robust analysis of complex scattering data under noise in microwave resonators". In: *Review of Scientific Instruments* 86.2 (Feb. 2015), p. 024706. ISSN: 0034-6748. DOI: 10.1063/1.4907935. eprint: https://pubs.aip.org/aip/rsi/article-pdf/doi/10.1063/1.4907935/15732678/024706_1_online.pdf. URL: https://doi.org/10.1063/1.4907935.

[134] Anthony J Annunziata et al. "Tunable superconducting nanoinductors". In: *Nanotechnology* 21.44 (Oct. 2010), p. 445202. DOI: 10.1088/0957-4484/21/44/445202. URL: https://dx.doi.org/10.1088/0957-4484/21/44/445202.

[135] C Girardin et al. "Study of the electron mean free path by ballistic electron emission microscopy". In: *Journal de Physique III* 6.5 (1996), pp. 661–669.

[136] Daniel Gall. "Electron mean free path in elemental metals". In: *Journal of applied physics* 119.8 (2016).

[137] Cheng-Hsuan Kuo et al. "Low-Resistivity Titanium Nitride Thin Films Fabricated by Atomic Layer Deposition with TiCl4 and Metal–Organic Precursors in Horizontal Vias". In: *ACS Applied Electronic Materials* 5.8 (2023), pp. 4094–4102.

[138] F Schrey, RD Mathis, and RT Payne. "Structure and properties of rf sputtered, superconducting tantalum films". In: *Thin Solid Films* 5.1 (1970), pp. 29–40.

[139] LYL Shen. "Superconductivity of tantalum, niobium and lanthanum studied by electron tunneling: Problems of surface contamination". In: *AIP Conference Proceedings*. Vol. 4. 1. American Institute of Physics. 1972, pp. 31–44.

[140] Mustafa Bal et al. "Systematic improvements in transmon qubit coherence enabled by niobium surface encapsulation". In: *npj Quantum Information* 10.1 (2024), p. 43.

[141] Slawomir Simbierowicz et al. "Inherent Thermal-Noise Problem in Addressing Qubits". In: *PRX Quantum* 5 (3 July 2024), p. 030302. DOI: 10.1103/PRXQuantum.5.030302. URL: https://link.aps.org/doi/10.1103/PRXQuantum.5.030302.

[142] G. Catelani et al. "Decoherence of superconducting qubits caused by quasiparticle tunneling". In: *Phys. Rev. B* 86 (18 Nov. 2012), p. 184514. DOI: 10.1103/PhysRevB.86.184514. URL: https://link.aps.org/doi/10.1103/PhysRevB.86.184514.

[143] URL: https://athena.ecs.csus.edu/~milica/EEE212/HAND/HFSSintro.pdf.

[144] Ilya Besedin and Alexey P. Menushenkov. "Quality factor of a transmission line coupled coplanar waveguide resonator". In: *EPJ Quantum Technology* 5.1 (Jan. 2018), p. 2. ISSN: 2196-0763. DOI: 10.1140/epjqt/s40507-018-0066-3. URL: https://doi.org/10.1140/epjqt/s40507-018-0066-3.

[145] S. Krinner et al. "Engineering cryogenic setups for 100-qubit scale superconducting circuit systems". In: *EPJ Quantum Technology* 6 (2019), p. 2. DOI: 10.1140/epjqt/s40507-019-0072-0. URL: https://doi.org/10.1140/epjqt/s40507-019-0072-0.

[146] qkit developers. *qkit – a quantum measurement suite in Python*. https://github.com/qkitgroup/qkit. Accessed 2026.

[147] Jeremy M. Sage et al. "Study of loss in superconducting coplanar waveguide resonators". In: *Journal of Applied Physics* 109.6 (Mar. 2011), p. 063915. ISSN: 0021-8979. DOI: 10.1063/1.3552890. eprint: https://pubs.aip.org/aip/jap/article-pdf/doi/10.1063/1.3552890/15071073/063915_1_online.pdf. URL: https://doi.org/10.1063/1.3552890.

[148] Janka Biznárová et al. "Intermodulation spectroscopy and the nonlinear response of two-level systems in superconducting coplanar-waveguide resonators". In: *Phys. Rev. Appl.* 22 (1 July 2024), p. 014063. DOI: 10.1103/PhysRevApplied.22.014063. URL: https://link.aps.org/doi/10.1103/PhysRevApplied.22.014063.

[149] J. Burnett et al. "Evidence for interacting two-level systems from the 1/f noise of a superconducting resonator". In: *Nature Communications* 5.1 (June 2014), p. 4119. ISSN: 2041-1723. DOI: 10.1038/ncomms5119. URL: https://doi.org/10.1038/ncomms5119.

Appendices

A. Numerical Code for nanobridge Junctions

A list of the new terms created in sfepy can be found in :New linear terms in Sfepy.

```
from __future__ import print_function
from __future__ import absolute_import
from sfepy import data_dir
from sfepy.discrete.fem.utils import refine_mesh
from sfepy.base.base import output
import numpy as np
from sfepy.base.base import Struct
from scipy.optimize import fsolve
from sfepy.terms.terms import Term, terms
from sfepy.terms import register_term
import sys

from sfepy.linalg import dot_sequences



class MultiNonlinearDiffusionTerm(Term):
    """
     Product of gradient of virtual, gradient of state and function of state.
    :Definition:
    .. math::
        \int_{\Omega} \nabla q1 \cdot \nabla p1 f(p1,p2)
    :Arguments 1:
        - function : :math:‘f‘
        - virtual : :math:‘q1‘
        - state   : :math:‘p1‘
        - state   : :math:‘p2‘
    """
    name = 'dw_mnl_diffusion'
    arg_types = ('fun', 'fun_d_1','fun_d_2', 'virtual', 'state_1','state_2')
```

```
    arg_shapes = {'material_fun'     : '1: 1',
                  'material_fun_d_1'    : '1: 1',
                  'material_fun_d_2'    : '1: 1',
                  'virtual' : (1, 'state_1'),
                  'state_1'   : 1,
                  'state_2'   : 1,
}


    @staticmethod
    def function(out, out_qp, geo):
        status = geo.integrate(out, out_qp)
        return status


    def get_fargs(self, fun, dfun1, dfun2, var1, var2, var3,
                  mode=None, term_mode=None, diff_var=None, **kwargs):
        """
        print('=======')
        print(var1,'\n')
        print('=======')
        print('=======')
        print(var2,'\n')
        print('=======')
        print('=======')
        print(var3,'\n')
        print('=======')
        """
        vg1, _ = self.get_mapping(var1)
        vg2, _ = self.get_mapping(var2)
        vg3, _ = self.get_mapping(var3)
```

```
        if diff_var is None:
            geo = vg1
            val_grad_qp = self.get(var2, 'grad')
            val_qp = fun(self.get(var2, 'val'),self.get(var3, 'val'),var2)
            out_qp = dot_sequences(vg1.bfg, val_grad_qp*val_qp,'ATB')

            #fmode = 0

        elif diff_var == var2.name:
            #print('entered in diffvar2')
            geo = vg1
            val_grad_qp = self.get(var2, 'grad')
            val_d_qp = dfun1(self.get(var2, 'val'),self.get(var3, 'val'),var2)
            val_qp = fun(self.get(var2, 'val'),self.get(var3, 'val'),var2)
            out_qp = dot_sequences(vg1.bfg, vg2.bfg*val_qp,'ATB') +
                dot_sequences(vg1.bfg, val_grad_qp*val_d_qp,'ATB')*vg2.bf

            #fmode = 1

        elif diff_var == var3.name:
            #print('entered in diffvar3')
            geo = vg1
            val_grad_qp = self.get(var2, 'grad')
            val_d_qp = dfun2(self.get(var2, 'val'),self.get(var3, 'val'),var2)
            val_qp = fun(self.get(var2, 'val'),self.get(var3, 'val'),var2)
            out_qp = dot_sequences(vg1.bfg, val_grad_qp*val_d_qp,'ATB')*vg3.bf

            #fmode = 2

        return out_qp, geo


class MultiNonLinearVolumeForceTerm(Term):
```

```
    """
     Product of virtual and function of state.
    :Definition:
    .. math::
        \int_{\Omega} q1 f(p1,p2)
    :Arguments 1:
        - function : :math:‘f‘
        - virtual : :math:‘q1‘
        - state   : :math:‘p1‘
        - state   : :math:‘p2‘
    """
    name = 'dw_volume_mnvf'
    arg_types = ('fun', 'fun_d_1','fun_d_2', 'virtual', 'state_1','state_2')
    arg_shapes = {'material_fun'     : '1: 1',
                  'material_fun_d_1'    : '1: 1',
                  'material_fun_d_2'    : '1: 1',
                  'virtual' : (1, 'state_1'),
                  'state_1'   : 1,
                  'state_2'   : 1,
}


    @staticmethod
    def function(out, out_qp, geo, fmode):
        status = geo.integrate(out, out_qp)
        return status


    def get_fargs(self, fun, dfun1, dfun2, var1, var2, var3,
                  mode=None, term_mode=None, diff_var=None, **kwargs):
        vg1, _ = self.get_mapping(var1)
        vg2, _ = self.get_mapping(var2)
        vg3, _ = self.get_mapping(var3)
```

```
        if diff_var is None:
            geo = vg1
            val_qp = fun(self.get(var2, 'val'),self.get(var3, 'val'),var2)

            out_qp = dot_sequences(vg1.bf, val_qp,'ATB')

            fmode = 0

        elif diff_var == var2.name:
            geo = vg1
            val_d_qp = dfun1(self.get(var2, 'val'),self.get(var3, 'val'),var2)

            out_qp = dot_sequences(vg1.bf, val_d_qp*vg2.bf,'ATB')

            fmode = 1

        elif diff_var == var3.name:
            geo = vg1
            val_d_qp = dfun2(self.get(var2, 'val'),self.get(var3, 'val'),var2)

            out_qp = dot_sequences(vg1.bf, val_d_qp*vg3.bf,'ATB')

            fmode = 2
        return out_qp, geo, fmode

class MultiDeltaNonLinearVolumeForceTerm(Term):
    """
     Product of virtual and function of state.
    :Definition:
    .. math::
        \int_{\Omega} q1 f(p1,p2)
    :Arguments 1:
```

```
        - function : :math:‘f‘
        - virtual : :math:‘q1‘
        - state   : :math:‘p1‘
        - state   : :math:‘p2‘
    """
    name = 'dw_volume_Deltamnvf'
    arg_types = ('material', 'fun', 'fun_d_1','fun_d_2', 'virtual',
        'state_1','state_2')
    arg_shapes = { 'material'     : '1, 1',
                   'material_fun'      : '1: 1',
                   'material_fun_d_1'    : '1: 1',
                   'material_fun_d_2'    : '1: 1',
                   'virtual' : (1, 'state_1'),
                   'state_1'   : 1,
                   'state_2'   : 1,
}


    @staticmethod
    def function(out, out_qp, geo, fmode):
        status = geo.integrate(out, out_qp)
        return status


    def get_fargs(self, mat , fun, dfun1, dfun2, var1, var2, var3,
                  mode=None, term_mode=None, diff_var=None, **kwargs):
        vg1, _ = self.get_mapping(var1)
        vg2, _ = self.get_mapping(var2)
        vg3, _ = self.get_mapping(var3)

        if diff_var is None:
            geo = vg1
            val_qp = fun(self.get(var2, 'val'),self.get(var3, 'val'),var2)*mat
```

```
            #print(val_qp.shape)
            #print(mat.shape)
            out_qp = dot_sequences(vg1.bf, val_qp,'ATB')

            fmode = 0

        elif diff_var == var2.name:
            geo = vg1
            val_d_qp = dfun1(self.get(var2, 'val'),self.get(var3, 'val'),var2)*mat

            out_qp = dot_sequences(vg1.bf, val_d_qp*vg2.bf,'ATB')

            fmode = 1

        elif diff_var == var3.name:
            geo = vg1
            val_d_qp = dfun2(self.get(var2, 'val'),self.get(var3, 'val'),var2)*mat

            out_qp = dot_sequences(vg1.bf, val_d_qp*vg3.bf,'ATB')

            fmode = 2
        return out_qp, geo, fmode

class MultiNonLinearSurfaceJumpTerm(Term):

    name = 'dw_mnl_jump'
    arg_types = ('fun', 'fun_d_1','fun_d_2', 'fun_d_3','fun_d_4','virtual',
        'state_1','state_2', 'state_3','state_4')
    arg_shapes = {'fun'   : lambda x: x,
                  'fun_d_1'  : lambda x: x,
                  'fun_d_2'  : lambda x: x,
                  'fun_d_3'  : lambda x: x,
                  'fun_d_4'  : lambda x: x,
```

```
            'virtual' : (1, 'state_1'),
            'state_1'  : 1,
            'state_2'  : 1,
            'state_3'  : 1,
            'state_4'  : 1,}

integration='surface'

@staticmethod
def function(out, out_qp, geo):
    status = geo.integrate(out, out_qp)
    return status


def get_fargs(self, fun, dfun1, dfun2, dfun3, dfun4, var1, var2, var3, var4, var5,
              mode=None, term_mode=None, diff_var=None, **kwargs):
    vg1, _ = self.get_mapping(var1)
    vg2, _ = self.get_mapping(var2)
    vg3, _ = self.get_mapping(var3)
    vg4, _ = self.get_mapping(var4)
    vg5, _ = self.get_mapping(var5)
    #print(var3)

    if diff_var is None:
        geo = vg1
        val_qp = fun(self.get(var2, 'val'),self.get(var3, 'val'), self.get(var4,
            'val'),self.get(var5, 'val'), var2)

        out_qp = dot_sequences(vg1.bf, val_qp,'ATB')



    elif diff_var == var2.name:
```

```
            geo = vg1
            val_d_qp = dfun1(self.get(var2, 'val'),self.get(var3, 'val'),
                self.get(var4, 'val'),self.get(var5, 'val'),var2)

            out_qp = dot_sequences(vg1.bf, val_d_qp*vg2.bf,'ATB')


        elif diff_var == var3.name:
            geo = vg1
            val_d_qp = dfun2(self.get(var2, 'val'),self.get(var3, 'val'),
                self.get(var4, 'val'),self.get(var5, 'val'),var2)

            out_qp = dot_sequences(vg1.bf, val_d_qp*vg3.bf,'ATB')

        elif diff_var == var4.name:
            geo = vg1
            val_d_qp = dfun3(self.get(var2, 'val'),self.get(var3, 'val'),
                self.get(var4, 'val'),self.get(var5, 'val'),var2)

            out_qp = dot_sequences(vg1.bf, val_d_qp*vg4.bf,'ATB')

        elif diff_var == var5.name:
            geo = vg1
            val_d_qp = dfun4(self.get(var2, 'val'),self.get(var3, 'val'),
                self.get(var4, 'val'),self.get(var5, 'val'),var2)

            out_qp = dot_sequences(vg1.bf, val_d_qp*vg5.bf,'ATB')

        return out_qp, geo

register_term(MultiNonLinearSurfaceJumpTerm)
register_term(MultiNonlinearDiffusionTerm)
register_term(MultiNonLinearVolumeForceTerm)
```

```
register_term(MultiDeltaNonLinearVolumeForceTerm)
```